Title
The Influence of High-Temperature Plasticity on the Thermomechanical Behavior of Structural Materials in Power Conversion Systems

Author
Ghazari, Arian

Publication Date
2022

Peer reviewed|Thesis/dissertation

UNIVERSITY OF CALIFORNIA
Los Angeles

The Influence of High-Temperature Plasticity on the Thermomechanical Behavior of Structural Materials in Power Conversion Systems

A dissertation submitted in partial satisfaction
of the requirements for the degree
Doctor of Philosophy in Mechanical Engineering

by

Arian Ghazari

2022

ABSTRACT OF THE DISSERTATION

The Influence of High-Temperature Plasticity on the Thermomechanical Behavior of Structural Materials in Power Conversion Systems

by

Arian Ghazari
University of California, Los Angeles, 2022
Professor Nasr M. Ghoniem, Chair

High heat flux facing components (HHFFCs) under extreme thermal loading often fail due to surface damage and crack propagation as a result of combinations of mechanical and thermal loading. Body centered cubic (BCC) refractory metals, such as tungsten (W) and 9Cr steels, are good candidates for HHFFCs due to their high melting temperature and excellent mechanical properties. However, applications of these materials in extreme thermal and radiation environments are limited by their brittle response at low temperatures, and by thermal creep and degradation of their mechanical properties as a result of re-crystallization at high-temperature. The main objective of this thesis is to investigate the influence of high-temperature rate-dependent plasticity (creep), under both cyclic and steady loading, on the evolution of residual stresses, plastic strain accumulation, and thermal shock resistance of tungsten, tungsten foam, and 9Cr steels (F82H and Eurofer). The approach is mainly experimental, where constitutive modeling of material behavior and Finite Element (FE) analysis are used to analyze and understand experimental results. This work is focused on designing controlled thermomechanical experiments to investigate solid W and W foam fracture under a variety of constrains and loading conditions. We also construct multiphysics FE models of stress evolution in large-scale fusion energy structures (First Wall and Blanket (FW/B)), where thermal, mechanical, and radiation effects are taken into consideration. Special sample fixtures are designed and fabricated to apply certain constrains and boundary conditions under high heat flux thermal loading. Additionally, a heat flux sensor is designed to properly measure the incident heat flux on samples tested in the *High Energy Flux Test facilitY*

(HEFTY). Extensive experimental testing revealed that W foam can be used as a sacrificial (armor) material for high heat flux applications because of its resilience. The majority of foam samples survived severe cyclic plasma thermal loading, showing no significant damage. Micro-cracks were observed generally at ligament triple junctions. Large-scale cracks were not observed in any of the tested foam samples. The presence of micro-cracks in foam samples as compared to massive cracks in solid W samples is indicative of thermomechanical resilience. The accommodation of many micro-cracks in ligaments is possible without adverse effects on component integrity, as compared to massive through-the-thickness cracks in solid W that can lead to rupture and coolant ingress into the core plasma. Temperature measurements have shown that W foam can provide a degree of heat shielding for the substrate material due to a lower effective thermal conductivity. Thus, a plasma-facing component may include a top non-structural layer (armor) of W foam, bonded to a structural solid W substrate.

Multi-physics FE simulations of large-scale fusion energy structures (FW/B modules) reveal that gradients in the irradiation field variables (dpa and helium generation) result in a fanning deformation mode of the entire structure. Extreme deformation is observed for free side walls at 6 years of operation. The stress and plastic strain in the FW/B structure are found to increase due to radiation gradient effects. Constraining the side walls increases the bending type deformation and displacements, with the maximum displacement at the mid-plane of the FW. The build-up of residual stresses in the FW/B structure can cause crack propagation upon cool-down and during cyclic reactor operations. Potential failure concerns can be alleviated by design optimization. This may include controlling the cooling patterns of the structure to maintain a high yield strength in desired areas and to allow reduction in the yield strength in other areas that are under extreme tensile stresses. Three distinct dimensional stability modes have been revealed in the current study: (1) "self-similar growth" for unconstrained modules; (2) "bending" for constrained modules; and (3) "fanning" resulting from radiation damage gradients. We also show that the maximum temperature limit of 9Cr steels in a fusion energy environment is around 530 °C, and is dictated by the accumulation of large plastic creep strains, driven by swelling-induced stresses.

The dissertation of Arian Ghazari is approved.

Jaime Marian

Jiann-Wen Woody Ju

Timothy S. Fisher

Nasr M. Ghoniem, Committee Chair

University of California, Los Angeles

2022

Dedicated to my wife, Angineh Rostamiyan, for all her love and support through this journey.

TABLE OF CONTENTS

LIST OF FIGURES

LIST OF TABLES

ACKNOWLEDGMENTS

I would like to thank all the individuals who helped and supported me during the course of my thesis research. Obviously, the completion of this work would be impossible without their help.

Firstly, I would like to thank my incredible advisor Professor Nasr Ghoniem for all his support and remarkable advices during these years which gave direction to my research and career. Also, I appreciate his time, patient, experience, and wisdom that helped me to grow as a researcher and person.

I am also appreciative to my thesis committee members Professor Jaime Marian, Professor Jiann-Wen Woody Ju and Professor Timothy Fisher for their time, energy and guidance.

Much thanks goes to my lab mates for all their support during these years. In particular, Warren Nadvornick and Dylan Dickstein for their help in carrying out the experiments. Also, I would like to thank Yue Huang and Ruggero Forte for their help in the fusion energy structure project.

Special thanks goes to Professor Jaime Marian and Cameron McElfresh from his research group for their collaboration and input in tungsten and open-cell tungsten foam material characterization for the cyclic plasma heating and thermo-fracture projects. Also, I appreciate Professor Timothy Fisher and his group for their help in heat flux calibration.

I would like to thank Dr. Russ Doerner and the UCSD PISCES facility for conducting the helium plasma exposure experiments. Also, I want to thank Professor Robert Odette and Dr. Takuya Yamamoto for their collaboration and input in the work on irradiation effects on fusion energy structures.

Also, I would like to thank MTM CNC Machining Inc. for their help in machining experimental devices and sensors that I designed through my research.

Finally, I would like to thank my incredibly supportive and loving parents, Zaven Ghazari and Novart Abedi, who encouraged and helped me to pursue higher education and taught me to be patient and work hard to achieve my goals. Also, I would like to thank my brothers,

Artoor and Aren, for being with me through good and bad times.

VITA

2015 B.S. (Mechanical Engineering), University of California, Los Angeles.

2015-2020 Teaching Assistant, Mechanical and Aerospace Engineering Department, University of California, Los Angeles.

2015-Present Research Assistant, MATRIX Laboratory, Mechanical and Aerospace Engineering Department, University of California, Los Angeles.

2017 M.S. (Mechanical Engineering), University of California, Los Angeles.

PUBLICATIONS

1. Huang, Y., Nadvornick, W. I., **Ghazari, A.** & Ghoniem N. M. (2020) "Multiphysics-multiscale modeling of plasma-facing structures in extreme heat and radiation environments." *International Journal for Multiscale Computational Engineering*, **18**, 285–304.

2. **Ghazari, A.**, Forte, R., Yamamoto, T., Odette, R., Ghoniem, N. (2021). "Radiation effects on stress evolution and dimensional stability of large fusion energy structures." *Fusion Engineering and Design*, **172**, 112756.

3. **Ghazari, A.**, McElfresh, C., Dickstein, D., Marian, J., Ghoniem, N. (2021). "Effects of cyclic plasma heating on surface damage of micro-porous tungsten." *Physica Scripta*, **96(12)**, 124033.

4. **Ghazari, A.**, McElfresh, C., Dickstein, D., Nadvornick, W. I., Pintsuk, G., Wessel, E., Wirtz, M., Hughes, D., Williams, B., Marian, J., Ghoniem, N. (2022). "Intense Cyclic Heating Effects on Thermo-Fracture and Thermal Shock of Open-Cell Tungsten Foam." *Journal of Nuclear Materials*, submitted.

5. Nadvornick, W. I., **Ghazari, A.**, Dickstein, D., Patel, S., Williams, B., Hughes, D., Ghoniem, N. (2022). "Design, Fabrication, and Testing of a Water-Cooled High-Heat Flux Plasma-Facing Module." *Journal of Nuclear Materials*, in preparation for submission.

6. Murali, N., **Ghazari, A.**, Zheng, S., Jin, K., Fisher, T., Ghoniem, N., Li, X. (2022). "High-Temperature Oxidation of Haynes 282 Microtubes in CO_2." *Materials at High Temperatures*, submitted.

CHAPTER 1

Introduction and Objectives

Increasing need for power in different industries brings the attention to more efficient power conversion systems which require higher operating temperatures. Power conversion systems such as fusion reactors and high-temperature compact heat exchangers are operating at temperatures that push the material to their limit. This requires a good understanding of thermomechanical behavior of material under these extreme conditions to prevent catastrophic failures. Having experiments where one can apply constrains and boundary conditions similar to the ones material experiences in service assembly is necessary to understand the material response under high heat flux loading. Designing high heat flux facing components (HHFFC) is always challenging due to combination of thermal and mechanical loading in addition to major changes in material properties at elevated temperatures. Additionally, most of these components undergo cycling loading which complicates the loading nature even more. Investigating the failure of HHFFC can get complicated due to similar observed damages on materials that were under different constrains and loading conditions during their service. Cracks shown in Figures 1a and 1b are examples of thermomechanical damages observed on tungsten and ceramic components exposed to high heat flux. Looking at the crack propagation in divertor tungsten tile shown in Figure 1a it is hard to determine if this crack is due to temperature gradient across the tile, residual stresses upon cool-down or cyclic fatigue. Also, it is not clear that the crack shown on ceramic insulator in Figure 1b is due to thermal shock, thermal stresses or thermal expansion mismatch. In order to have better understanding of failure mechanisms in such materials it is important to perform controlled experiments to take into account all the possible conditions which can cause failure in materials. Developing controlled experiments can help to test the material under variety

of loading conditions having certain constrains and boundary conditions. This work will present design of controlled experiments and sample fixtures that can be used to examine failure mechanisms in HHFFC such as tungsten, ceramics and foams. However, the main experimental focus will be on solid tungsten and tungsten foam failure mechanisms. The High Energy Flux Test facilitY (HEFTY) and designed and fabricated sample fixtures will be discussed in Chapter 4 of this thesis. Also, measuring and calibrating the incident heat flux on samples is crucial both for validating the experimental condition and FE analysis. Chapter 5 presents the design of a heat flux sensor and experimental setups to measure the magnitude and distribution of heat flux in HEFTY. Then, a heat flux profile is developed for HEFTY to be used in FE analysis describing HEFTY's tests.

(a) (b)

Figure 1: Crack propagation under high heat flux in (a) divertor tungsten tile [1] and (b) ceramic insulation [2].

Exceeding need of reliable high temperature material in aerospace and fusion energy structures brought researchers interest to characterize and develop high temperature materials capable of keeping reasonable mechanical properties at elevated temperatures. Tungsten is in huge interest to be used in high temperature components due to its high melting temperature. However, tungsten applications are limited by its brittle behavior below its Ductile to Brittle Transition Temperature (DBTT), 200-400 °C, and after recrystallization at temperatures above ≈ 1300 °C. Therefore, in this report open-cell tungsten foams (W foams) are proposed as armor for HHFFC and are studied in great details by high-heat flux tests performed in HEFTY. W foam has great advantage of having porous structure capable of

allowing free thermal expansion under high heat flux loading. Also, flexible ligaments in W foam can rotate and bend to accommodate thermal strains without major damage. Thermal and mechanical properties of W foam are controlled by its volume fraction (relative density) and pores-per-inch (PPI) as will be discussed later in this thesis. Variety of W foams with different volume fraction and PPI were tested and reported in Chapter 6 to find the most resilient one to thermal shock and cyclic loading outside W allowable operating window (below DBTT and above recrystallization temperature). After defining the best performing foam (best combination of volume fraction and PPI), this foam was tested under extreme thermal loading condition and was compared with tungsten disks tested under the same condition. Experimental results and detailed structural analysis for these tests are presented in Chapter 7.

Material degradation due to high temperature and irradiation fields in fusion reactors HHFFC is another concern in design of these components which dictates their dimensional stability and lifetime. Chapter 8 presents structural analysis for a large fusion energy structure including radiation effects on material degradation and stress evolution showing the deformation and potential failure modes. This is followed by the lifetime assessment for this structure discussed in Chapter 9 including creep studies.

The objectives of this thesis are summarized as follows:

- To Develop controlled thermomechanical experiments at high heat flux.
- Measure plasma high heat flux magnitude and distribution.
- Explore the influence of high-temperature plasticity, residual stresses and thermal shock on open cell tungsten foam and bulk tungsten.
- Demonstrate the influence of thermal and radiation fields on stress evolution and dimensional stability of fusion energy structures using FE analysis.
- Investigate lifetime of fusion energy structures considering radiation and creep at elevated temperatures.

CHAPTER 2

Mechanical Properties of High-Temperature Structural Materials

The need for reliable high temperature materials in energy production and aerospace fields takes all the attention to tungsten, which has the highest melting temperature among elements and maintains reasonable mechanical properties at elevated temperatures. In addition, mechanical properties of tungsten such as high elastic modulus and thermal conductivity make this material a good candidate for high temperature applications.
Some of the main challenges of using tungsten is its brittleness which can cause sever fracture and failure in design. Having a high ductile to brittle transition temperature (DBTT) limits tungsten usage at temperatures below DBTT due to significant reduction in ductility. Also, tungsten's recrystallization temperature puts an upper band on its service temperature. Even though tungsten's melting point is around 3400 °C, passing recrystallization temperature (≈1300 °C) makes the material supper brittle. Researchers put lots of effort on reducing tungsten DBTT using alloying technique and thermomechanical processes and succeed to some extend. Mechanical and thermal properties of tungsten are summarized in this chapter. Also, a detailed discussion is provided on tungsten fracture toughness and DBTT.

Another important material in energy production and conversion systems is F82H steel which is one of the the main candidates for structural material in fusion systems. F82H is a fully martensitic steel with very small amount of Mn, Ti, C, Si, Ta and V. The content of high activation elements are low in this type of steel as described in [3] making it ideal for fusion applications. Since F82H is being used in computational analysis of fusion structures presented in this thesis, its mechanical and thermal properties are summarized in this

chapter.

2.1 Mechanical and Thermal Properties of Tungsten

Tungsten is one of the main high-temperature structural materials studied in this thesis. Therefore, its thermal properties such as conductivity, thermal expansion coefficient and specific heat are presented here as function of temperature. These properties are used in heat transfer and thermal analysis through this report.

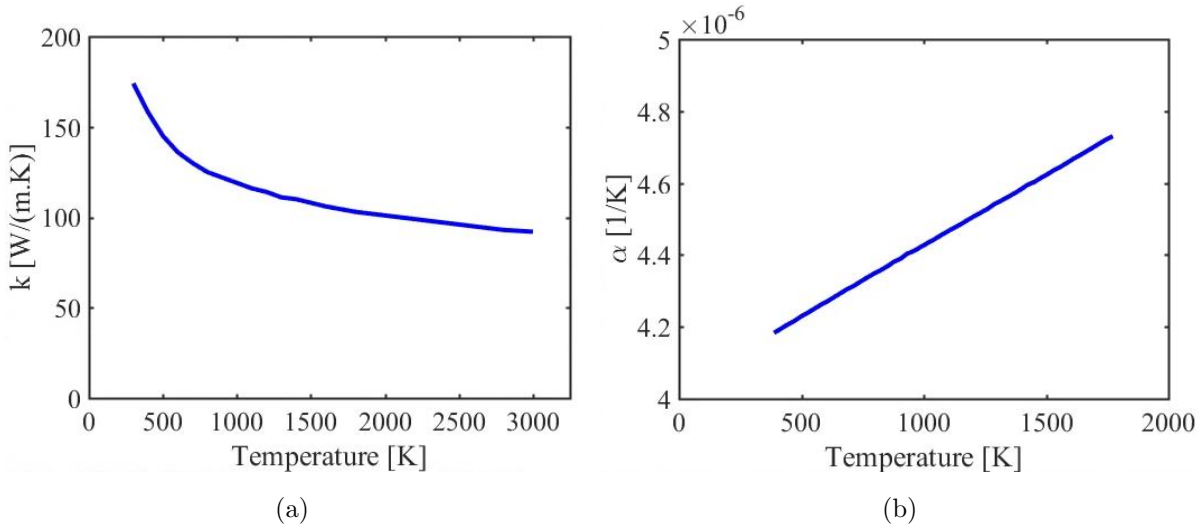

Figure 2: (a) Tungsten thermal conductivity [4]. (b) Tungsten thermal expansion coefficient [4].

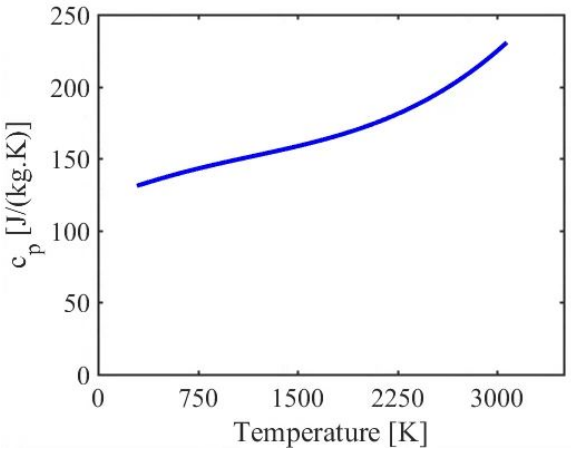

(a)

Figure 3: Specific heat of tungsten [5].

In order to consider high-temperature effects in structural analysis, temperature dependent mechanical properties are used in FE simulations studied in this thesis. Yield strength and Young's modulus of tungsten are obtained from experimental data provided at [4] as plotted in Figure 4.

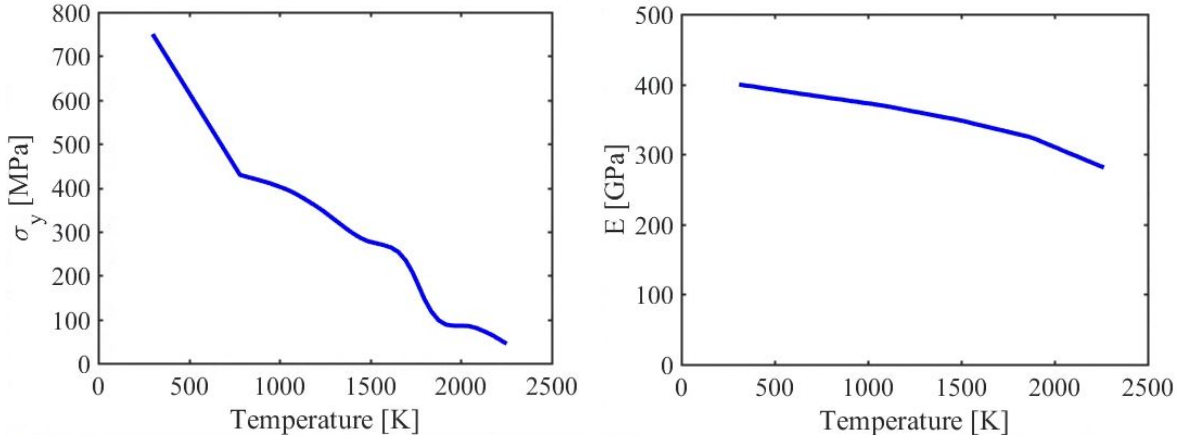

(a) (b)

Figure 4: (a) Tungsten yield strength obtained form experimental data provided at [4] for 780-2250 [K] temperature range (yield strength at room temperature is obtained from COMSOL nominal value and a linear distribution is assumed from room temperature to 780 [K].) (b) Tungsten Young's modulus [4].

2.1.1 Tungsten Fracture Toughness & DBTT

The main cause of brittleness in tungsten is reported to be lack of close pack planes in its crystal, reduction of grain boundaries cohesion due to impurities and strain incompatibilities between grains [6]. Thermomechanical processes such as rolling, forging and equal-channel angular pressing (ECAP) are one of the most important ways of improving ductility and reducing DBTT in tungsten. Researchers proposed several mechanisms causing the ductility during thermomechanical processes. Thermomechanical processes not only reduce tungsten grain size but they introduce lamellar textured microstructure and directional elongated grains with small angle grain boundaries. Also, low-temperature thermomechanical processes increases edge and high mobility dislocations density in tungsten. In addition, thermomechanical processes improve grain boundary cohesion by reducing impurity concentration at grain boundary as a result of increasing grain boundary density. Also, it is mentioned that the textured microstructure inhibits the crack front propagation to some extend [6]. Lastly, thermomechanical processes increase tungsten density and decrease its porosity which can act as source of strain concentration causing ductility reduction. DBTT of annealed tungsten reduces from 675 °C to 375 °C and 125 °C utilizing hot rolling and cold rolling respectively [7]. Rolling temperature has a great influence on grain size and ductility of tungsten and finer grains can be obtained by lower rolling temperatures [6]. It is important to notice that ductility obtained from low temperature rolling can be diminished by subsequent higher temperature rolling as shown in Figure 5.

ECAP is more effective in reducing the grain size compare to rolling and can generate ultrafine-grained tungsten with grain size of about 0.3-2 μm which is smaller than the ones generated by rolling (1-4 μm for rolling below 1200°C [7] and 100 μm for rolling at 1500°C [8]) and is capable of reducing DBTT to 386 °C and 322 °C for ECAP performed at 800 °C and 950 °C respectively [9].

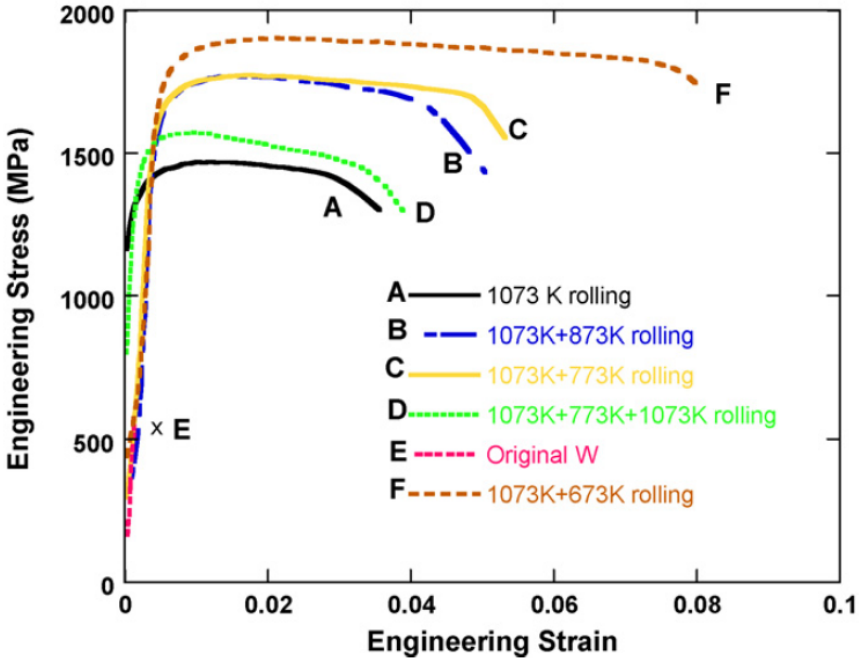

Figure 5: Engineering Stress Strain curves of room temperature tensile test for tungsten rolled at different temperatures [10].

Alloying with rhenium has a great effect on tungsten ductility and DBTT. Adding rhenium to tungsten reduces Peierls stress in tungsten which helps easier activation of dislocations and improves low temperature mobility of screw dislocations. Also, it promotes additional slip systems such as {112} by solid solution formation [6]. In Addition, rhenium alloying reduces grain boundary segregation and brittleness by trapping impurities such as oxygen in lattice [11]. Arc-melted and rolled tungsten with 1.9 wt% rhenium is reported to have a DBTT of 25 °C which is much lower than the rolled pure tungsten with DBTT of 113 °C [6]. Some drawbacks of using rhenium in tungsten is its cost and its transmutation to osmium under neutron radiation in radioactive environments.

Producing ultrafine-grained and noncrystalline tungsten using sintering technic is another approach to produce small grain size tungsten to improve its mechanical properties. This approach succeed to improve fracture toughness and hardness of tungsten. However, it shows no significant change in ductility and DBTT of tungsten unless it is subject to thermomechanical process. This shows the importance of textured and directional elongated lamellar microstructure in ductility and DBTT of tungsten.

Main Factors Affecting Tungsten Fracture Toughness & DBTT:

Choosing material for structural applications can get complicated due to change in materiel response at different temperature regimes. Refractory metals such as tungsten are known to have a transition temperature called DBTT below which the ductile response of material changes to brittle fracture leading to a catastrophic failure. Since tungsten is proposed as plasma-facing material in fusion reactors such as ITER [12], it is important to have a clear understanding of material response at different loading condition and temperature regimes. In addition to radiation damage and extreme mechanical and thermal loading, plasma-facing material needs to be resilient enough for critical operation conditions such as thermal shock which introduces high strain rates in material [13].

DBTT can be obtained by performing 3 point bending or 4 point bending experiments at different temperatures and measuring the fracture toughness. As increasing the temperature fracture toughness increases and at a certain temperature a huge increase in fracture toughness is observed. This temperature is defined as DBTT for material below which there is significant decrease in material ductility. DBTT strongly dependent on the loading rate ($\dot{K}$) which allows obtaining an activation energy for ductile to brittle transition (DBT). Activation energy for DBT can be obtained by Arrhenius plot of log $\dot{K}$ versus 1/BDTT [14]. In addition to loading rate, sample size, fracture system and initial dislocation density can change DBTT in material. Therefore, understanding the controlling mechanism for DBT has been challenging for researchers.

DBT is a measure of material fracture toughness which is directly related to crack propagation under certain load. Crack propagation depend on plastic deformation induced by dislocation near the crack tip at a given temperature and loading rate. Having dislocation nucleation and motion near the crack tip can prevent crack propagation by blunting he crack tip and reducing stress intensity factor. Higher temperature and lower loading rates increase dislocation activity and plasticity leading to higher fracture toughness and lower DBTT.

Some researchers have developed models in which dislocation mobility is introduced as controlling factor for DBT [15, 16]. However, there are others [17, 18] that believe dislocation nucleation is the main factor controlling DBT. It has been shown for other materials that

DBT activation energy is comparable with the one required for dislocation motion [15] which propose dislocation mobility as the main factor controlling DBT.

In BCC materials such as tungsten plasticity is mainly due to screw dislocations which have smaller mobility compare to edge dislocations. Also, screw dislocation motion is mainly due to kink pair formation. Therefore, it can be concluded that dislocations activation energy in tungsten is mainly due to kink pair formation. Gumbsch et al. [14] used tungsten DBTT experimental data and obtained a DBT activation energy of 0.2 eV for tungsten and compared it with reported activation energy for screw dislocation in tungsten (2 eV). According to Gumbsch et al. [14] tungsten DBT activation energy is one order smaller than its screw dislocation activation energy which doesn't support the mobility base controlling force for DBT. However, in another work done by Giannattasio et al. [13] it is shown that the activation energy for DBT is around 1.05 eV which is much larger than the one reported by Gumbsch. The much smaller DBT activation energy (0.2 eV) reported by Gumbsch is due to crack system $\{110\}\langle 110\rangle$ used in his experiments [13]. In this crack system crack is mainly shielded by edge dislocations which have lower activation energy [19]. According to Giannattasio's work screw dislocations control the shielding of crack tip on $\{100\}$ crack system with a kink pair activation energy of about 1 eV which is in close agreement with DBT activation energy (1.05 eV) obtained in his report which supports mobility base controlling force for DBT. It is important to notice that four-point bending test on tungsten single-crystal at Giannattasio report shows much larger plastic deformation compare to the three-point bending test performed by Gumbsch on single crystal [13].

Sample geometry and shape, crack depth and plastic deformation can greatly influence DBTT measured in experiments. Basically, change in geometry varies the pre-factor in BDT Arrhenius law leading to a shift in DBTT. However, the geometric factors do not effect DBT activation energy. Therefore, DBTT measured at a given loading rate for a material might not be considered as an invariant physical parameter for that material [13].

Researchers have performed lots of experiments on single-crystal and poly-crystalline tungsten to investigate mechanisms controlling ductile to brittle transition. It can be seen from Figure 6a and 6b that DBTT does not change much from $\{100\}$ fracture surface to

{110} staying around 380 K for ⟨011⟩ crack front direction and 470 K for ⟨001⟩ direction on both surfaces. However, there is a significant increase in fracture toughness going from {100} fracture surface to {110} for both crack tip directions at almost all temperatures above 77 K. The higher fracture toughness on {110} plane can be explained by higher dislocation activity on this plane in BCC that can prevent cleavage of the crack tip by plasticity.

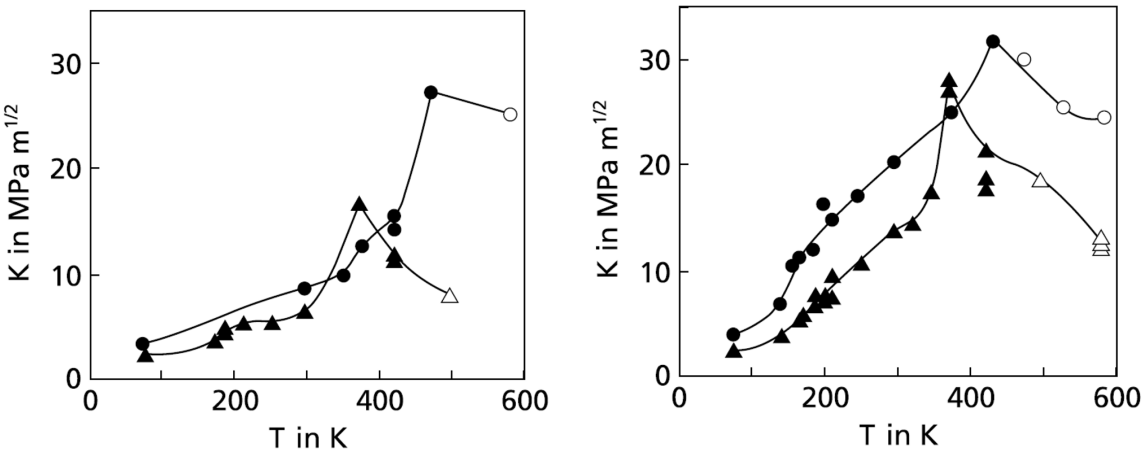

Figure 6: Fracture toughness of tungsten single crystal measured at different temperatures for four low index crack systems. The ⟨001⟩ crack front is indicated by circles and the ⟨011⟩ crack front is indicated by triangles. Filled symbols represent stress intensity factors and open symbols represent maximum stresses at ductile failure normalized by crack length. (a) Shows results for {100} fracture surface, and (b) shows Results for {110} fracture surface. [14].

Experiments performed on tungsten sharp pre-cracked specimens and tungsten notched specimens reveal the effect of high stress concentration at sharp crack which reduces fracture toughness and shifts the DBTT to higher temperatures. It can be seen from Figure 7 that fracture toughness of sharp pre-cracked specimen is smaller than the notched one for all temperatures.

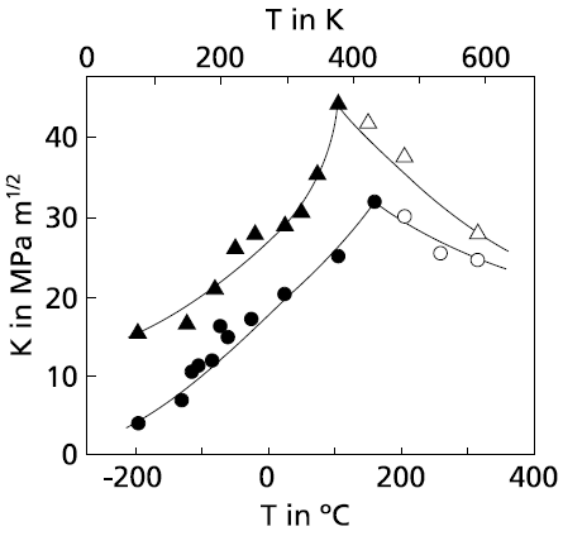

Figure 7: Fracture toughness at different temperatures for tungsten sharp pre-cracked (circle) and notched (triangles) specimens with (011) [100] crack system (Filled symbols represent stress intensity factors and open symbols represent maximum stresses at ductile failure normalized by crack length) [14].

Experiments have shown dependence of fracture toughness at a given temperature to amount of dislocation sources available in material. It can be seen from Figure 8 that fracture toughness of pre-deformed tungsten at lower temperature regimes is higher than undeformed samples. This is due to pre-existing dislocations from pre-deformation which at high stress regions such as rack tip can act as dislocation sources to enhance the crack tip shielding. At intermediate temperatures the benefits of pre-deformations dies out due to work hardening effects which increases yield strength and reduces dislocation mobility. This can cause reduction in fracture toughness and shifts DBTT to higher temperatures [14].

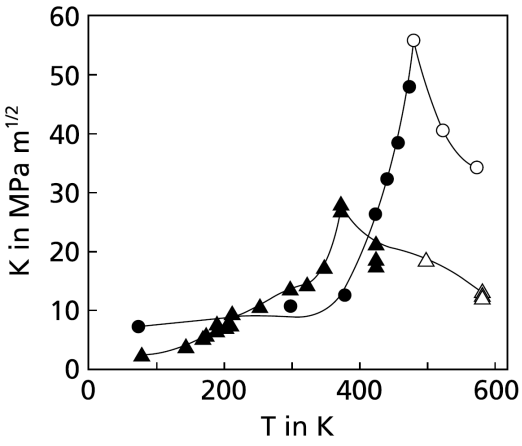

Figure 8: Fracture toughness of pre-deformed (circles) and undeformed reference samples (triangles) at different temperatures. (Filled symbols represent stress intensity factors and open symbols represent maximum stresses at ductile failure normalized by crack length) [14].

Loading rate has a great effect on fracture toughness as shown in Figure 9. Increasing loading rate lowers fracture toughness and shifts DBTT to higher temperatures. Tungsten fracture toughness at room temperature reduces (16 to 6 MPa $m^{1/2}$) linearly with logarithm of loading rate increasing from 0.04 to 6 MPa $m^{1/2}s^{-1}$ [14]. It is important to notice that at 77 K changing loading rate does not effect the fracture toughness due to lack of dislocation activities at such low temperatures.

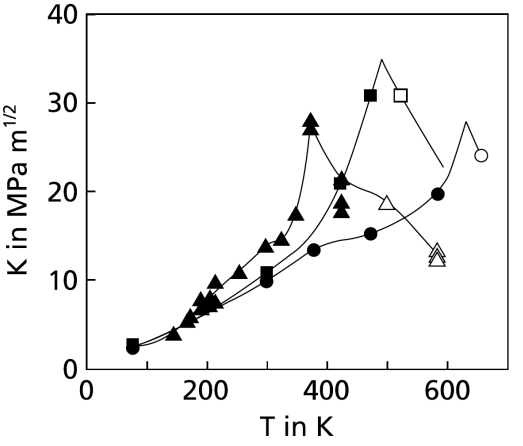

Figure 9: Loading rate $\dot{K}$ effect on fracture toughness of pre-cracked single crystal tungsten with $\{110\}\langle 1\bar{1}0\rangle$ crack system. For triangles $\dot{K}$=0.1 MPa $m^{1/2}s^{-1}$, squares $\dot{K}$=0.4 MPa $m^{1/2}s^{-1}$ and circles $\dot{K}$=1.0 MPa $m^{1/2}s^{-1}$. (Filled symbols represent stress intensity factors and open symbols represent maximum stresses at ductile failure normalized by crack length) [14].

In an experimental work done by Giannattassio et al. [13] effects of grain boundaries

on DBTT is studied by performing fracture toughness test at different temperatures for variety of strain rates on tungsten single crystal and polycrystal samples. It can be seen from Figures 10 and 11 that DBTT at each strain rate stays almost the same for single and poly-crystal tungsten. This might be a sign that DBTT is driven by dislocation mobility which is the same for single crystal and poly-crystal since grain boundaries have no effect on dislocation mobility. However, grain boundaries can act as barrier for crack cleavage to increase fracture toughness. This can be seen by comparing Figures 10 and 11. Even though DBTT values for each strain rate reported for poly-crystal tungsten is closely agree with the ones reported for single crystal samples, the fracture toughness values of poly-crystalline samples are almost twice bigger than single crystal tungsten samples. Also, effects of grain boundaries on hindering crack propagation and increasing fracture toughness can be seen at 77 K where polycrystalline samples show a fracture toughness which is almost twice bigger than single crystal tungsten samples.

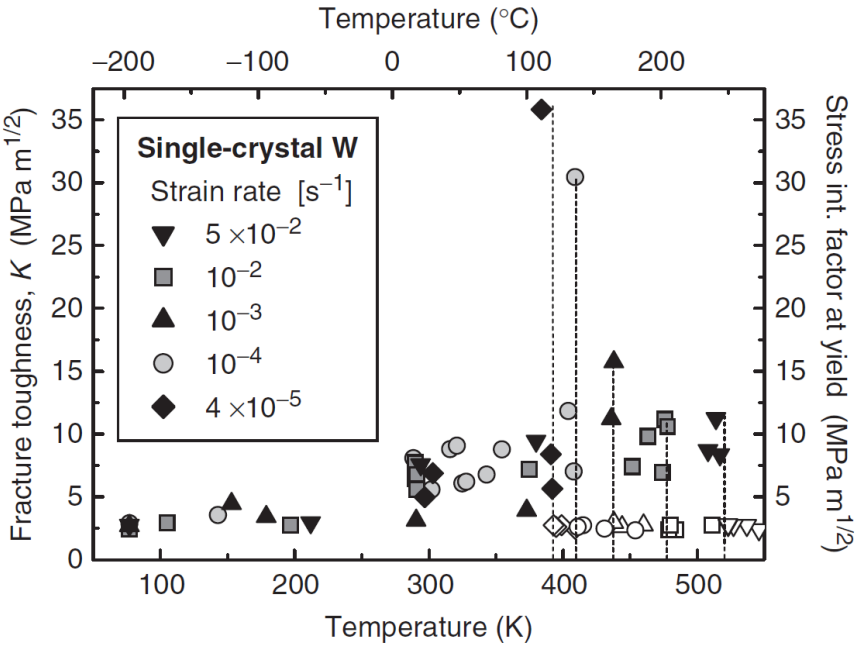

Figure 10: Measured fracture toughness in single crystal tungsten as a function of temperature and strain rate. Solid symbols represent fracture toughness (left axis) and open symbols are stress intensity factor at yield (K_{Iy} (right axis) for ductile failure occurring after DBTT) [13].

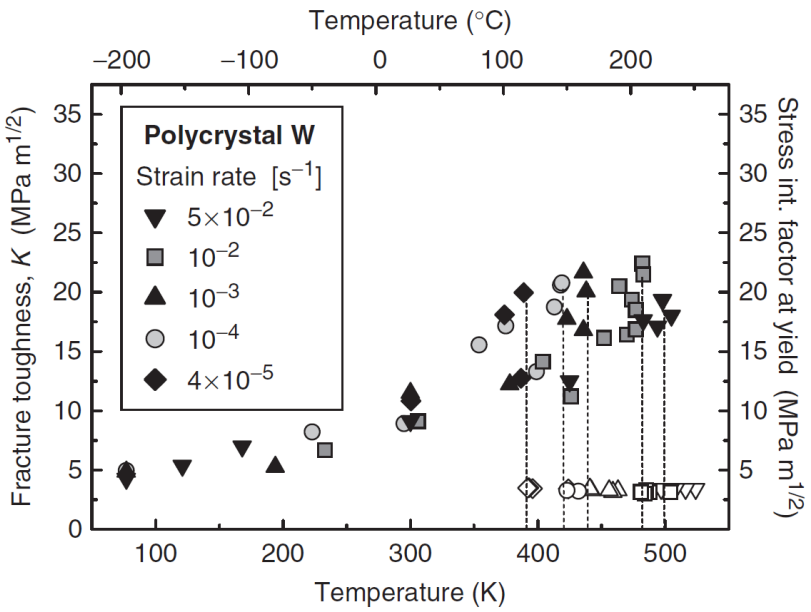

Figure 11: Measured fracture toughness in poly-crystal tungsten as a function of temperature and strain rate. Solid symbols represent fracture toughness (left axis) and open symbols are stress intensity factor at yield (K_{Iy} (right axis) for ductile failure occurring after DBTT) [13].

Figure 12 shows DBT activation energy versus DBTT for materials that are known for having dislocation mobility as the controlling force for DBT. The linear fit to the data is shown by the dash line which provides the relationship $E_{\mathrm{DBT}}/(k\ \mathrm{DBTT})=25$ between DBT activation energy (E_{DBT}) and DBTT for mentioned materials where k is Boltzmann constant.

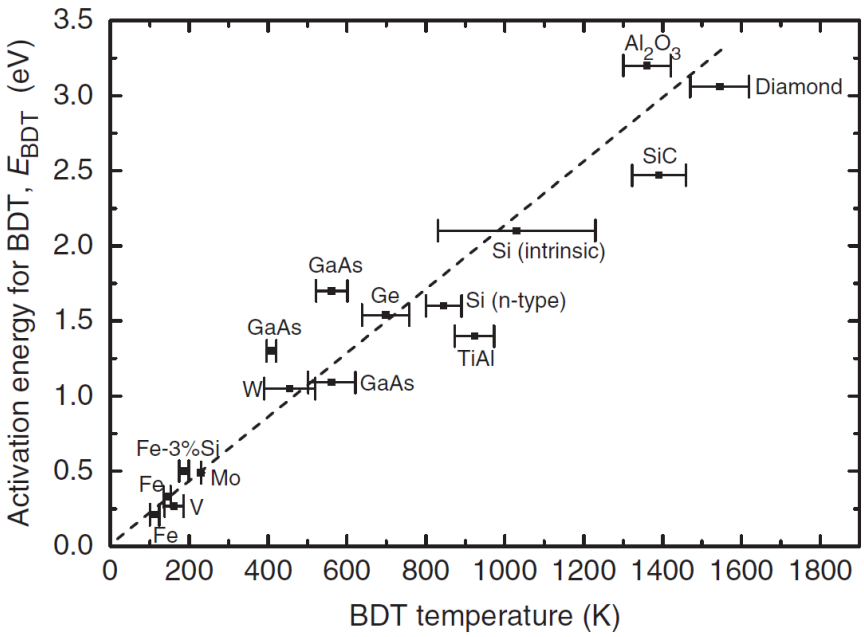

Figure 12: DBT (or BDT) activation energy (E_{BDT}) of different materials as function of their DBTT (BDT temperature). Range of DBTT for each material is shown as a horizontal error bar. This range is mainly due to effect of strain rate on DBTT [13].

In summary, owing to its high melting temperature, high plasma sputtering erosion resistance [12], and low sputtering yield [20], tungsten is one of the candidate materials for plasma-facing components in nuclear fusion application. However, the reduced ductility of tungsten at low temperatures remains a concern and hinders its applications as a structural material. The two major factors contributing to the low-temperature brittleness of tungsten are the limited mobility of dislocations within the bcc lattice, and the poor cohesion of grain boundaries [6]. Although empirical and phenomenological research has led to significant improvements in the ductility of tungsten and lowering its DBTT by alloying and thermo-mechanical treatments, tungsten components still fracture in high temperature applications under various loading conditions which need to be investigated by controlled experiments to reveal the main reasons causing these failure.

2.2 Mechanical and Thermal Properties of F82H Steel

F82H is one of the main candidates to be used as structural material in fusion applications. This section presents thermal properties such as thermal conductivity, thermal expansion coefficient and specific heat as function of temperature for this material. These properties are used in FE simulations of fusion structure (FW/B) studied in this thesis to perform heat transfer and thermal analysis.

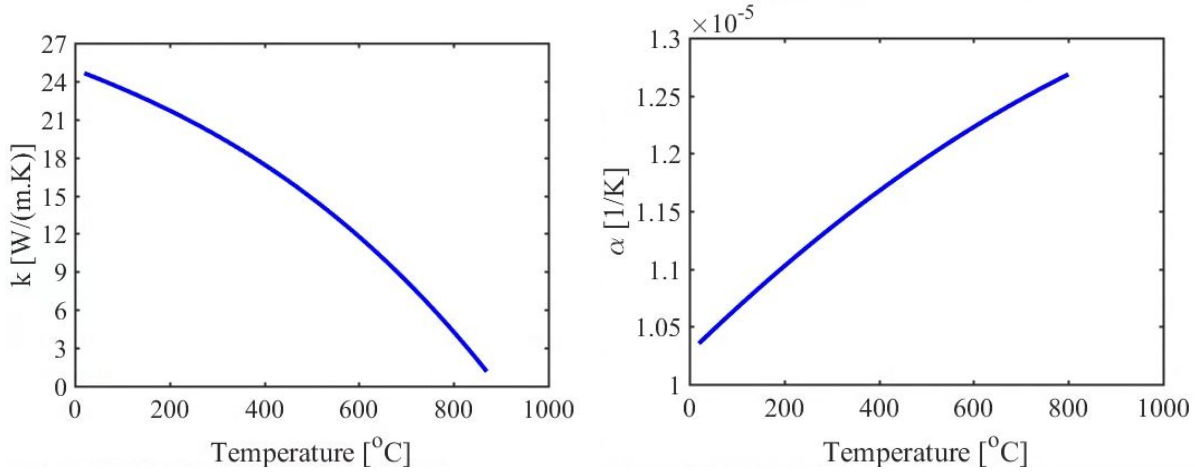

(a) (b)

Figure 13: (a) F82H steel thermal conductivity [3]. (b) F82H steel thermal expansion coefficient [3].

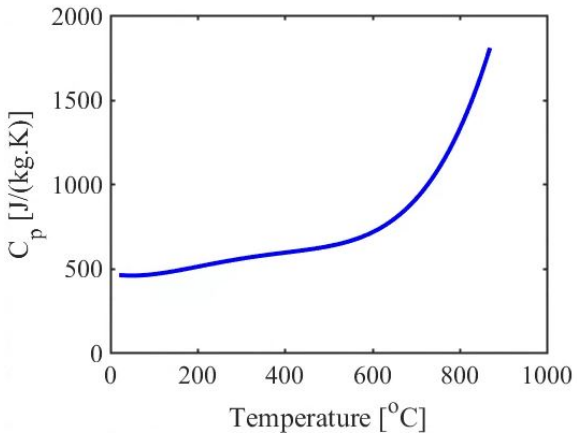

(a)

Figure 14: Specific heat of F82H steel [3].

Also, in order to consider high-temperature effects in structural analysis, temperature dependent material properties are used in the fusion structure FE simulations. Yield strength, Young's modulus and ultimate tensile strength as function of temperature presented in following figures are used in these studies.

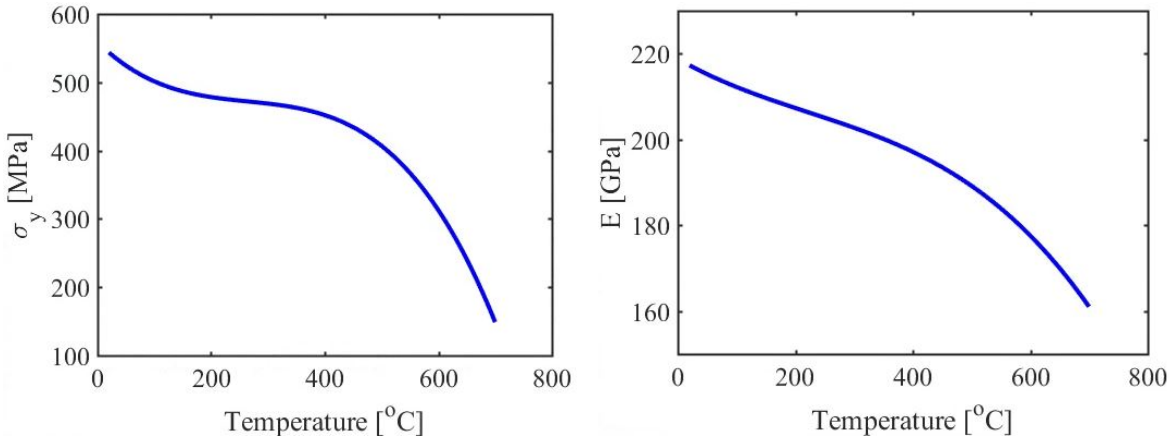

(a) (b)

Figure 15: (a) F82H steel yield strength [3]. (b) F82H steel Young's modulus [3].

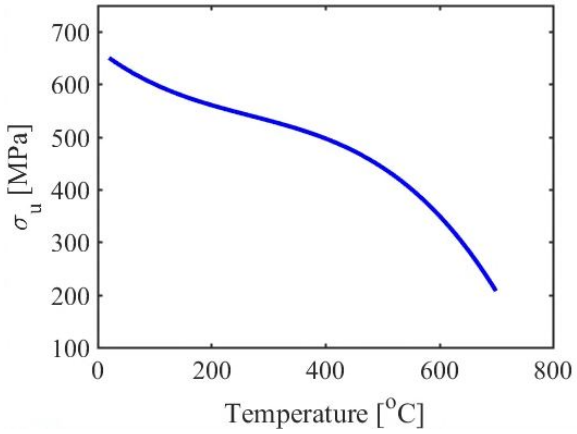

(a)

Figure 16: F82H steel ultimate tensile strength [3].

CHAPTER 3

Plastic Deformation Under Cycling Loading

3.1 Material Response to Cyclic Mechanical Loading at High-Temperature

Components such as cooling tubes which are under combined mechanical (pressure) and cyclic thermal loading (heating from one side and cooling form the other side) can face stress regimes such as R_1 and R_2 (Ratcheting), S_1 and S_2 (Shakedown after first half-cycle), P (Plastic cycling) and E (Elastic) which are shown in Figure 18. Since axial stress due to internal pressure is half of the hoop stress, the axial stress can be neglected and stress state for such components can be simplified to uniaxial stress on a slab shown on Figure 17. The uniaxial stress σ is composed of a mechanical component σ_p and a thermal component σ_t as shown in equation 1.

$$\sigma = \sigma_p + 2x\sigma_t/d \tag{1}$$

$$\sigma_t = \frac{E\alpha\Delta T}{2\,(1-\nu)} \tag{2}$$

Taking a look at equation 1 it can be seen that at $x = d/2$ (outer wall of the tube) thermal stress σ_t will be added to the tensile hope stress from internal pressure. However, at $x = -d/2$ (inner wall of the tube) thermal stress will be compressive.

Temperature drop across the tube's wall is denoted with ΔT and in order to use the uniaxial model and add up the thermal stress to the hope stress caused by internal pressure the $1/(1-\nu)$ fraction is used.

Bending is not desired for such components under service and assumption of having no bending leads to a uniform strain in the loading direction through the thickness d. The strain ε is composed of elastic strain σ/E, thermal strain αT and plastic strain η.

$$\varepsilon = \frac{\sigma}{E} + \alpha T + \eta \tag{3}$$

where temperature changes linearly through the wall thickness as;

$$T = \frac{-\Delta T x}{d} \tag{4}$$

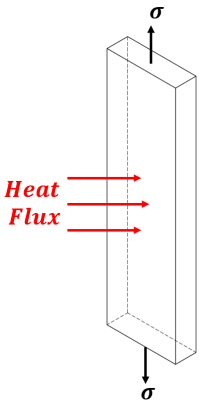

Figure 17: Cross section view of component under combined loading

It can be seen form equation 3 that keeping total strain constant through the thickness requires certain combinations of elastic and plastic strains to cancel out the linear x dependence of the thermal strain. This idea is used to create the stress-strain curves for stress regimes and develop the conditions separating boarders between different stress regimes shown on Figure 18.

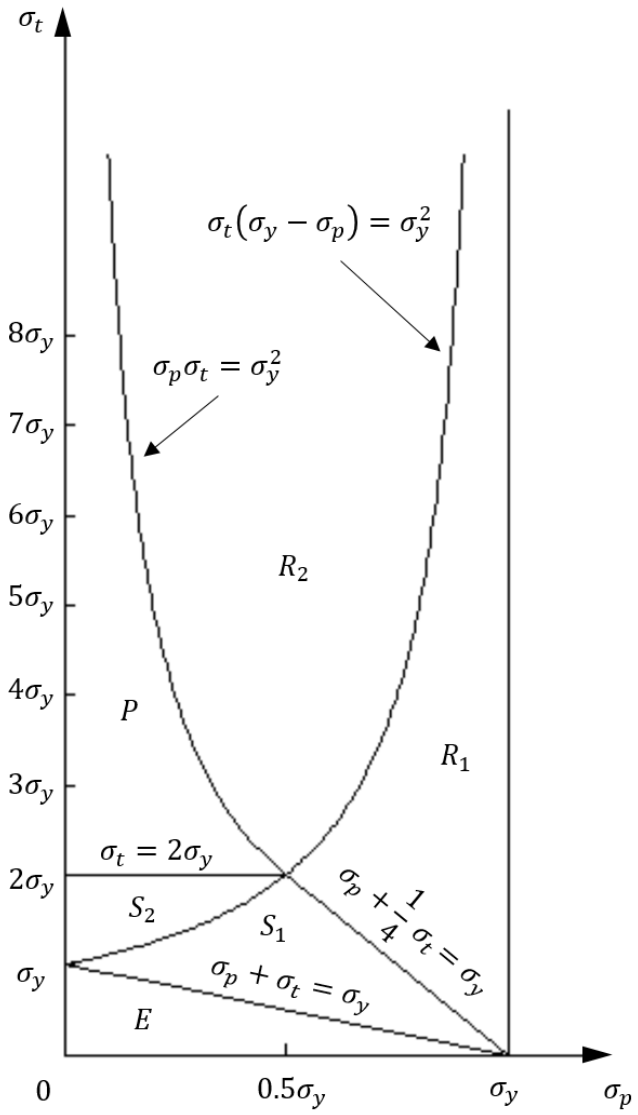

Figure 18: Stress Regimes under combined pressure and cyclic thermal loading for non-work-hardening material with constant yield strength with respect to mean temperature [21]

Knowing applied mechanical stress σ_p and calculating σ_t using equation 2 one can determine the component's stress regime utilizing Figure 18. If the combined mechanical and thermal stress σ (constant mechanical load σ_p and cyclic thermal load with half cycle *On* and half cycle *Off*) at first half cycle, causes material yielding to exceed half the way through the thickness, material will experience ratcheting in which plastic strain will accumulate in every cycle. This stress regime is defined as R_1 and its stress and strain distributions are shown on Figure 19.

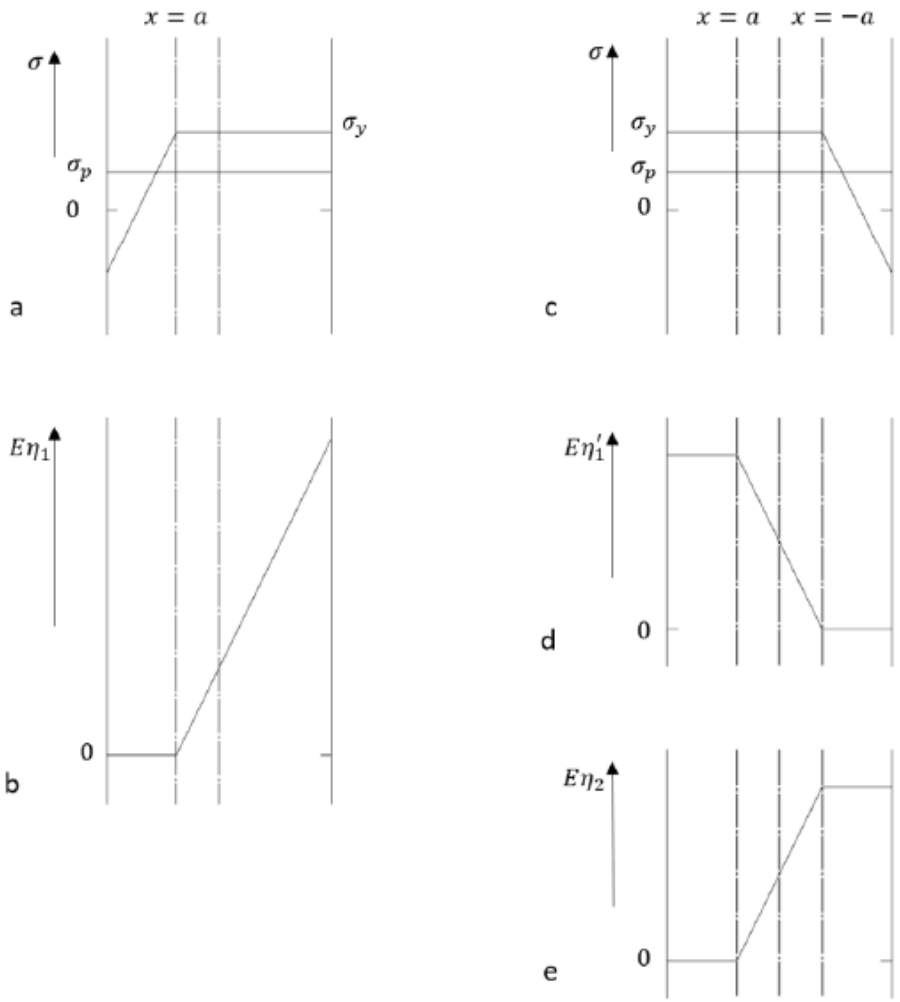

Figure 19: Stress and strain distributions for stress regime R_1. a) Stress at first half of each cycle (On time). b) Plastic strain at first half-cycle. c) Stress at second half of each cycle (Off time). d) Plastic strain at second half of each cycle. e) Plastic strain at first half of each cycle after the first. [21]

In the case where the yielding zone does not exceed the half of the component's thickness at the first half cycle, there will be only an initial plastic strain and the plastic strain will not accumulate in each cycle. This stress regime is denoted as plastic regime P in Figure 18 and its stress and strain distributions are shown in Figure 20. Having such cyclic plastic strain can cause fatigue failure at certain number of cycles as shown in Figure 21. It can be seen that a large strain amplitude can reduce the fatigue life of the component significantly.

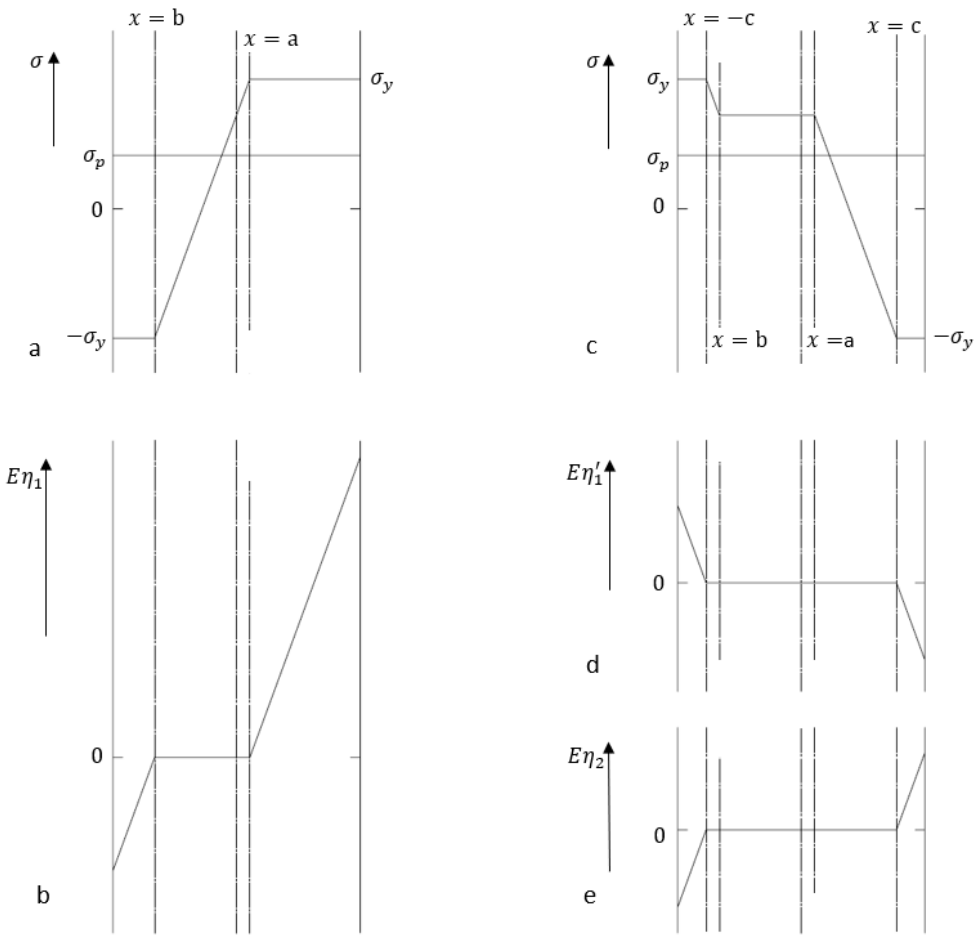

Figure 20: Stress and strain distributions for stress regime P. a) Stress at first half of each cycle (On time). b) Plastic strain at first half-cycle. c) Stress at second half of each cycle (Off time). d) Plastic strain at second half of each cycle. e) Plastic strain at first half of each cycle after the first [21].

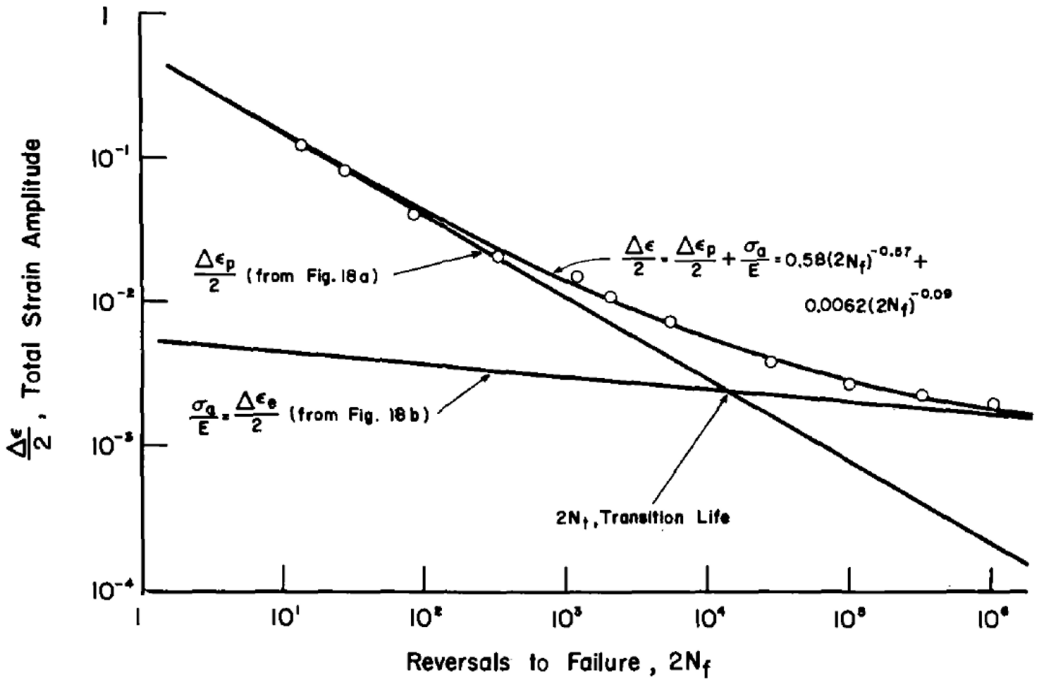

Figure 21: A log-log plot showing relationship between strain amplitude and fatigue life [22].

Stress regime R_2 is similar to R_1. However, in R_2 materiel yields from inner wall as well as the outer one. Stress and strain distributions for this regime are shown in Figure 22.

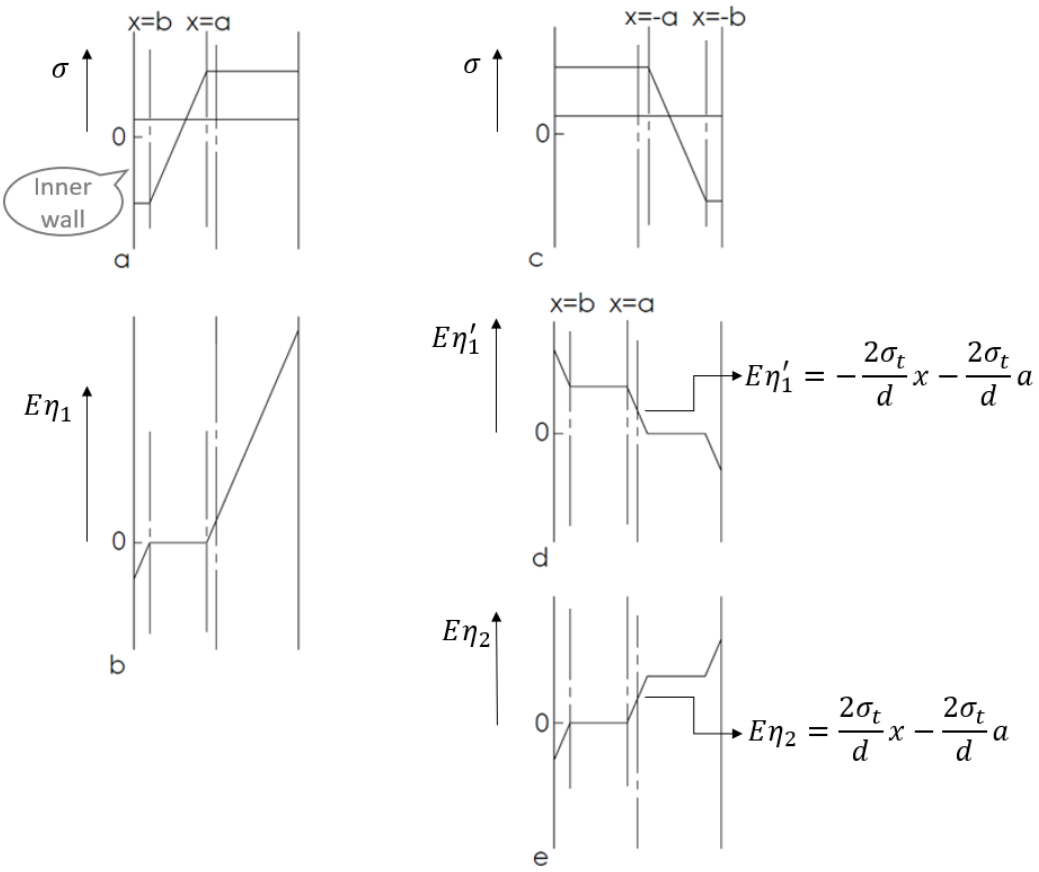

Figure 22: Stress and strain distributions for stress regime R_2. a) Stress at first half of each cycle (On time). b) Plastic strain at first half-cycle. c) Stress at second half of each cycle (Off time). d) Plastic strain at second half of each cycle. e) Plastic strain at first half of each cycle after the first.

Plasma-facing components (PFCs) such as divertor and first wall in fusion reactors like ITER are subjected to stationary heat fluxes reaching to 10 MW/m^2 [23] during normal operating conditions and short thermal transient loading with power densities in range of GW/m^2 during plasma instabilities. Thermal transient loading can cause crack propagation induced by residual stresses during cool down. Figure 23 shows a crack initiated from heating face of a tungsten tile which was under high heat flux loading. Under thermal transient a huge power density in range of GW/m^2 is being applied to PFCs in very short amount of time in order of few ms. This causes a steep temperature gradient in depth of few mm leading to a huge temperature difference between the direct loading zone and the rest of surrounding material [24]. The loading zone experiences significant thermal expansion due to supper high temperature and is constrained with the rest of surrounding material experiencing

much smaller thermal expansion. Under kinematic constrains from surrounding material, the loading zone accumulate plastic compressive strain due to large thermal expansion and lowered yield strength at such extreme temperatures built up at loading zone. During cooling time the surrounding material goes back to its initial configuration elastically. However, the heated area goes under tension from surrounding material due to residual compressive strain and permanent shrinkage that was accumulated in this area during heating time. During cooling time as temperature drops, tensile residual stress builds up. In addition, material experiences a significant drop in ductility and fracture toughness as temperature drops below its DBTT. As a result, material undergoes brittle fracture due to high residual tensile stress at brittle regime below DBTT.

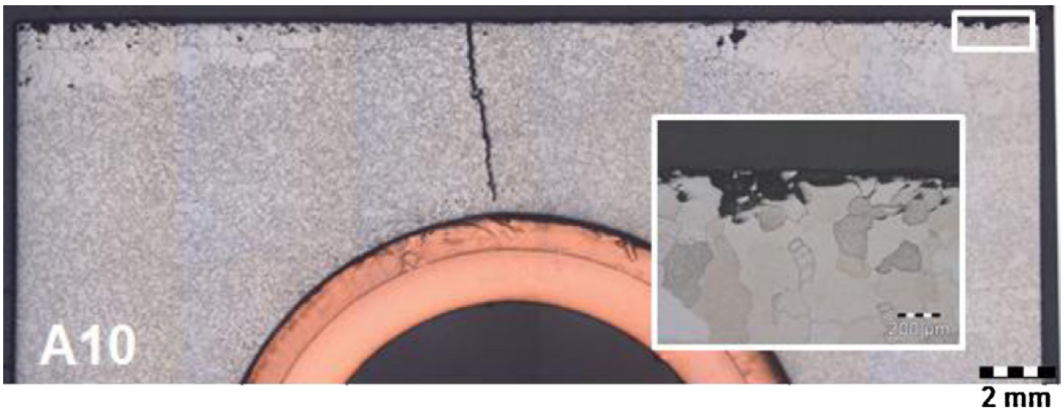

Figure 23: Crack initiation on a tungsten tile from heating face due to residual stresses under high heat flux loading [25].

Li et al. [24] calculated J-integral as a function of thermal transient load power density for two cases, crack existing prior to thermal loading and crack initiation after cool down shown on Figure 24a. Having the assumption of an existing crack or flow in material prior to thermal loading, overestimates the load magnitude at crack tip as it can be seen form the J-integral values. Figure 24b shows the strong dependence of the J-integral and crack tip load to base temperature (temperature of material at the end of cool down). It can be seen that having a low base temperature increases J-integral by a large amount. This is due to magnitude of tensile residual stress which increases as material temperature reduces to reference temperature converting entire stored compressive residual strain in material to tensile stress. At base temperatures 600 °C and above, J-integral saturates around 0.1

mJ/mm^2 and does not increase with power density ranges provided. It can be seen that having a low base temperature can help crack initiation both by increasing stress intensity factor at crack tip and reducing material fracture toughness at base temperatures below DBTT. Failure and crack initiation at each base temperature can be predicted by comparing the J-integral values from Figure 24b with calculated values for critical J-integral at each base temperature shown on table 1, which are obtained with linear elastic material assumption as follows:

$$G = \frac{{K_I}^2}{E} \tag{5}$$

$$J = G \text{ (linear elastic assumption)} \Rightarrow J = \frac{K_I^2}{E} \tag{6}$$

$$J_c = \frac{K_{Ic}^2}{E} \text{ (critical value of J-integral)} \tag{7}$$

where G is the strain energy release rate, K_I is the mode I Stress intensity factor, K_{Ic} is the mode I plain strain fracture toughness, J is the J-integral, and J_c is the critical value of the J-integral.

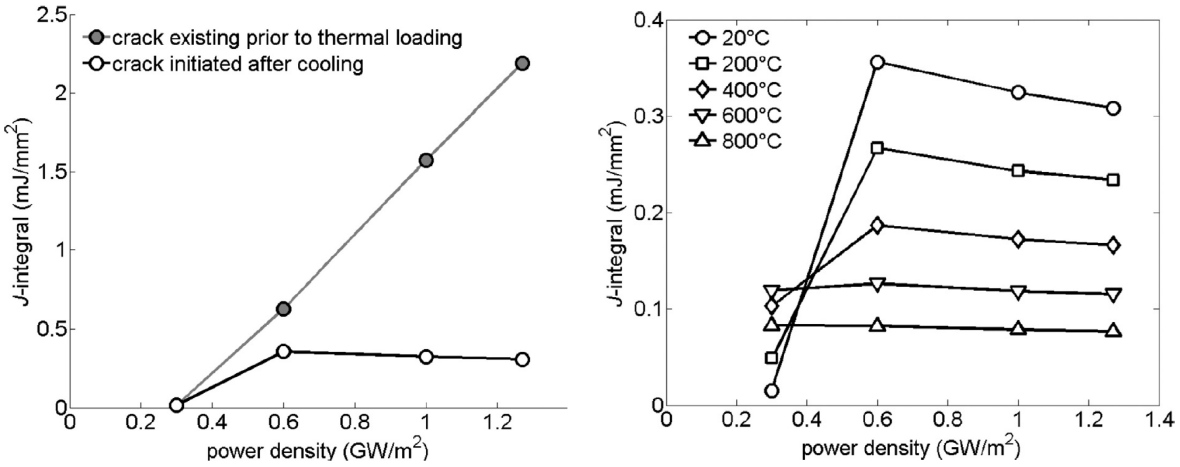

(a) (b)

Figure 24: J-integral as a function of thermal transient power density (a) Calculated for 20μm pre-existing crack (filled circles) and 20μm crack initiated after cool down (hollow circles) with 20°C base temperature for both cases. (b) Calculated for a 20μm crack initiated after cool down with base temperatures of 20-800°C [24].

Temperature (°C)	20	200	400	600	800
Critical value of J-integral (mJ/mm^2)	0.1549	0.2329	0.4325	0.9582	2.4579

Table 1: Critical values of J-integral obtained from fracture toughness data in [26] for 20-800°C base temperatures assuming linear elastic fracture mechanics [24].

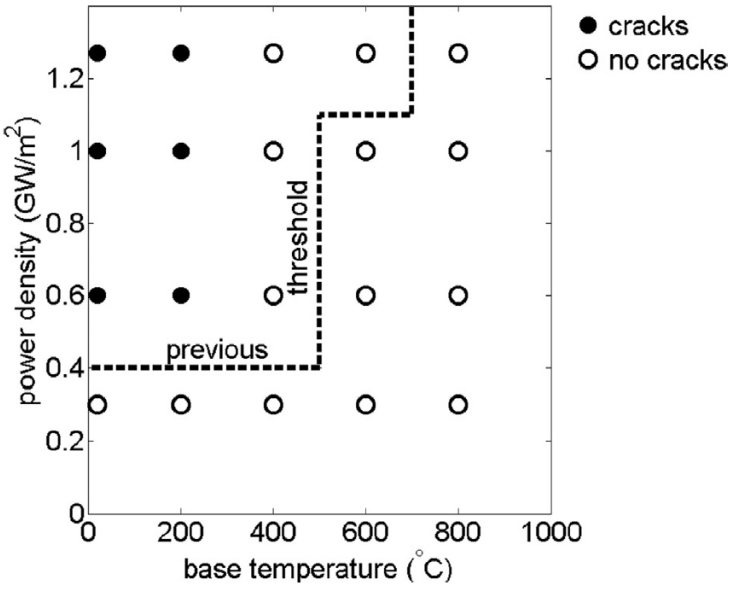

Figure 25: Prediction of tungsten crack map for a relevant range of power densities and base temperatures. The dashed line is the threshold obtained with assumption of a pre-existing crack before thermal loading and the separation region between solid circles and open circles at the top left corner is calculated threshold considering a 20μm crack initiated during cool down [24].

Figure 25 presents a crack map for tungsten at a given power density and base temperature. This figure predicts the threshold for critical loading regimes where crack might occur in tungsten. The threshold is identified by comparing the J-integral values for a 20μm crack calculated at a certain base temperature for an applied power density with critical J-integral values obtained from fracture toughness of tungsten at that base temperature. It is important to notice that Figure 25 presents two different threshold. First one is the dash lines and the second one is located at the regions between solid circles and open ones at the top left corner. The dash line threshold is calculated with the assumption of a pre-existing crack in material and the later one is calculated assuming the crack initiates during cool down. It can be seen that pre-existing crack assumption overestimates the load at crack tip lead-

ing to a lower allowable power densities and higher temperature at end of cool down (base temperature) limiting the material operation at lower temperatures. The second assumption (crack initiation during cool down) leads to a threshold power density somewhere between 0.3 to 0.6 GW/m^2 and a threshold base temperature between 200 to 400 °C for tungsten [24]. Comparing the experimental work performed by Linke et al. [27] shown on Figure 26a with the predicted map of Li et al. [24] presented on Figure 25 it can be seen that Li's prediction overestimates crack tip load by showing a higher allowable base temperature. This can be due to the fact that surface of experimental specimens were well polished leaving no crack or very small cracks in material compare to the 20 μm crack used in J-integral calculations in Li's work. Comparing double forged pure tungsten crack map (Figure 26a) with WTa5 shown in Figure 26b it can be seen that WTa5 can undergo a higher range of power density and lower base temperature without any cracking. This is due to anisotropic texture in material ,grain shape and grain orientation with respect to applied thermal transient load [27].

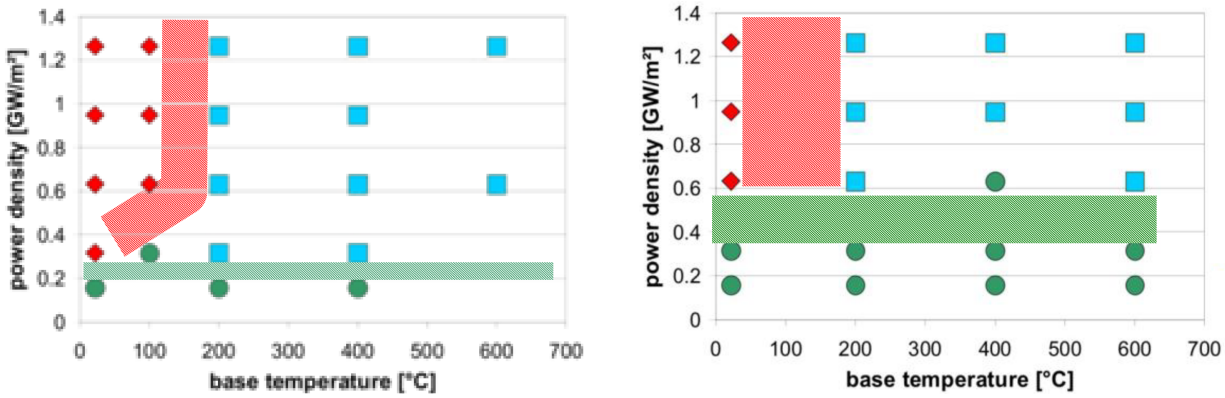

(a) (b)

Figure 26: Crack map and thermally induced surface damage under electron beam pulses of 1 ms duration for; (a) Double forged pure tungsten, (b) Tungsten alloy with 5 weight % tantalum (WTa5). For each data point 100 electron beam pulses are applied. Green symbols represent no damage, blue symbols represent surface modification and red symbols represent crack network [27].

3.2 Linear Hardening Plasticity Model of Irradiated Materials

Empirical constitutive models for structural materials are required for prediction of their thermomechanical response. Such models must provide clear dependence on the main environmental conditions and salient parameters. Therefore, all thermophysical properties of the low-activation structural material, F82H, must be assessed and presented with dependencies on temperature (T), neutron irradiation dose in units of displacements per atom (dpa), neutron-induced gas content (mainly helium) inside the structure, and the length of operational time. As the database keeps on expanding, the voracity of thermomechanical response predictions will improve. For F82H, a significant database already exists in several key publications [28, 3, 29, 30, 31, 32]. More recent work by [33, 34, 35] focused on radiation effects on the swelling, hardening, and softening.

The basic properties required for modeling the elasto-plastic behavior of F82H in the present FW/B study are the coefficient of thermal expansion (α), Young's modulus (E), the yield strength (σ_y), the ultimate strength (σ_u), strain-to-necking (ε_N), and the magnitude of volumetric swelling strain ($f_v = \frac{\Delta V}{V}$). Since we need to understand the effects of temperature distribution, pressure loading, and neutron irradiation on the stress state of the FW/B, we would need these properties to be available as functions of temperature (T) and displacement damage dose (Φ) measured in units of dpa. In the particular case of volumetric swelling, an additional dependence on the amount of generated helium gas inside the structure by neutron irradiation would also be required. Thus, an additional parameter, the helium-to-dpa ratio r is introduced.

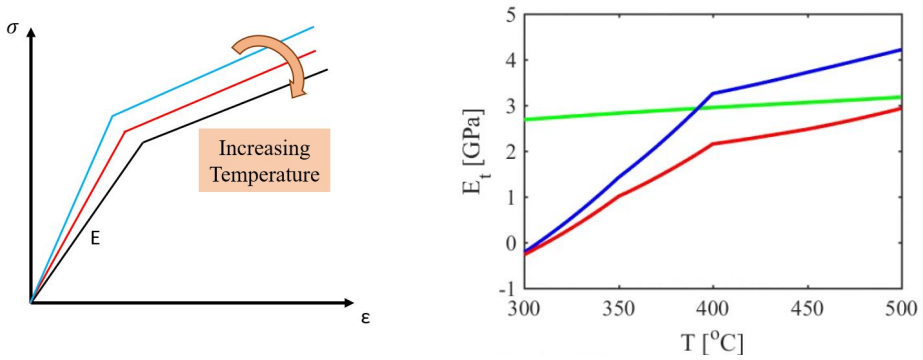

(a) (b)

Figure 27: (a) Illustration of the linear hardening model with temperature-dependent elastic modulus (E), and temperature and irradiation dose dependent tangent modulus (E_t), (b) tangent modulus at BOL (0 dpa, green curve), 45 dpa (blue curve) and 90 dpa (red curve) as function of temperature.

We model the constitutive elasto-plastic behavior of F82H by employing a temperature and irradiation-dependent linear hardening model, as shown in Figure 27a. In this model E, σ_y, σ_u and ε_N are functions of T, Φ (σ_y and σ_u are function of T and Φ but E and ε_N are only function of temperature due to limited experimental data). Temperature-dependent properties are taken from the work of [28], [3], [30] and [32]. However, a more recent data assessment by [33] and [35] indicates that radiation hardening as a change in the yield strength ($\Delta\sigma_y$) of F82H is dependent on (T, Φ, r), and that it can be positive (hardening) or negative (softening).

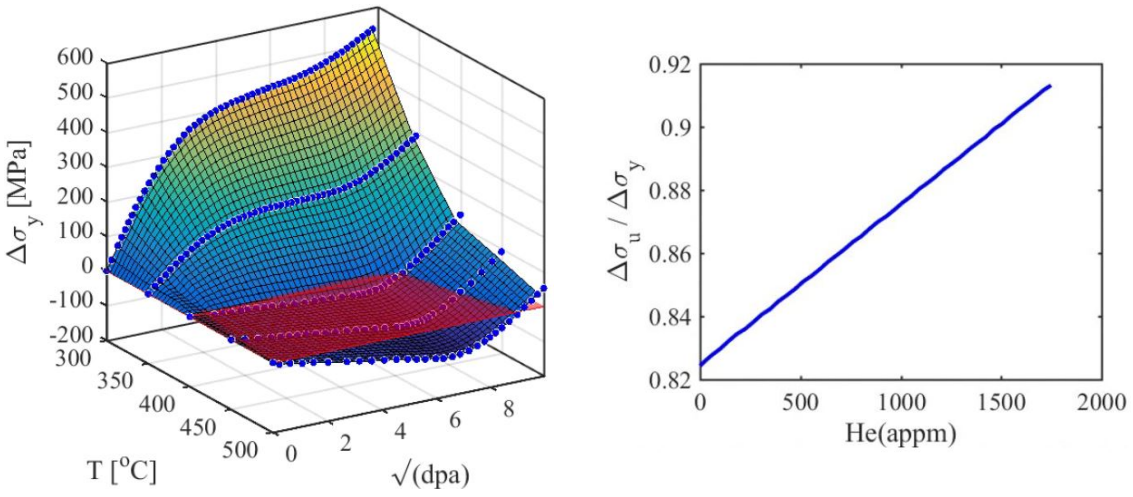

(a) (b)

Figure 28: (a) Hardening model ($\Delta\sigma_y$) prediction for F82H for fusion reactor conditions (He/dpa=10) adopted from [35]. (b) Ratio of change in ultimate strength to change in yield strength due to neutron irradiation as a function of He concentration [35].

Changes in the yield strength ($\Delta\sigma_y$) as function of dpa at different temperatures are shown in Figure 28a. This has been adapted from reference [35], and used in subsequent computer simulations. It can be seen that at high temperatures (above 400°C), F82H undergoes softening (-$\Delta\sigma_y$) up to about 64 dpa (the area under the red plane shown in Figure 28a), and then experiences hardening (+$\Delta\sigma_y$) at higher dpa. However, at lower temperatures (below 400°C), neutron irradiation leads to hardening behavior (+$\Delta\sigma_y$), even at low dose, as shown in Figure 28a. The influence of neutron irradiation and helium concentration on σ_u has been studied by [35], as reproduced in Figure 28b. Figures 29a and 29b show σ_y and σ_u at the BOL (0 dpa), 45 dpa and 90 dpa as function of temperature. Comparing σ_y non-irradiated case (0 dpa) with the one at 45 dpa in Figure 29a indicates F82H hardening [$\sigma_y(45\ dpa) > \sigma_y(0\ dpa)$] at temperatures below 392°C and softening [$\sigma_y(45\ dpa) < \sigma_y(0\ dpa)$] at temperatures above it. However, at 90 dpa, F82H experiences hardening from about 300°C to 500°C with higher hardening rates at lower temperatures.

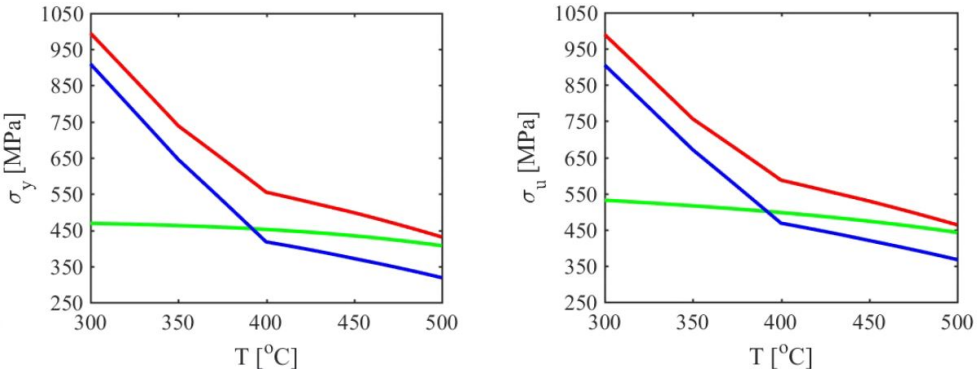

Figure 29: (a) σ_y and (b) σ_u at BOL (0 dpa, green curve), 45 dpa (blue curve) and 90 dpa (red curve) as function of temperature. (σ_y and σ_u are computed from irradiation data (Figures 28a, 28b) and temperature dependent data provided by [3].

A simplified linear hardening model is developed here to describe the elasto-plastic behavior of F82H under fusion neutron irradiation. In this model, the tangent modulus, $E_t(T, \Phi)$, is obtained from fitted data of the ultimate and yield strengths, Young's modulus and strain-to-necking as following:

$$E_t(T, \Phi) = \frac{\sigma_u - \sigma_y}{\varepsilon_N - \sigma_y/E} \tag{8}$$

Strain-to-necking (ε_N) data are adopted from experimental work of [30] and [32] showing effects of temperature on ε_N as plotted in Figure 30. Experimental data showing effects of neutron irradiation damage on ε_N is available up to 20 dpa ([30]) which is not sufficient for our study cases reaching to 45 dpa and 90 dpa. Therefore, we kept ε_N only function of temperature in our study till we get more experimental data in this regard for future works.

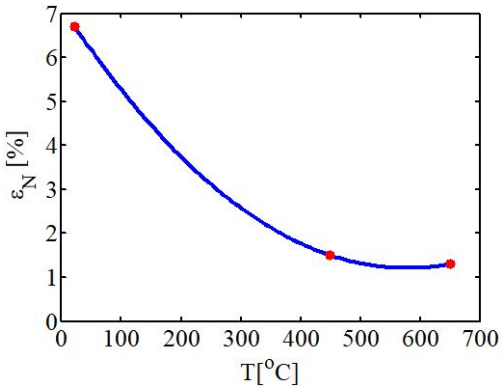

Figure 30: Strain-to-necking (ε_N) experimental data points (red dots) adopted from [30] and [32] and fitted curve (blue curve) used in our simulations.

Figure 27a shows a schematic of the linear hardening model, while Figure 27b shows the calculated tangent modulus as a function of temperature at the Beginning of Life (BOL), at 45 dpa, and at 90 dpa. It is noted from the figure that the tangent modulus drops to nearly zero at low temperature as a result of neutron irradiation, indicating possible onset of plastic instabilities. On the other hand, it is an increasing function of temperature above 300 °C, as shown in Figure 27b. Note also that as the structure is irradiated further (for example from 45 to 90 dpa), the tangent modulus, and hence the work hardening capacity of the structure, decreases. Stress-Strain curves for F82H at 375 °C and 500 °C are plotted in Figures 31a and 31b as discussed. It can be seen that at 375 °C irradiation causes more hardening at higher dpa. However, at 500 °C material goes under softening at 45 dpa and hardening at 90 dpa.

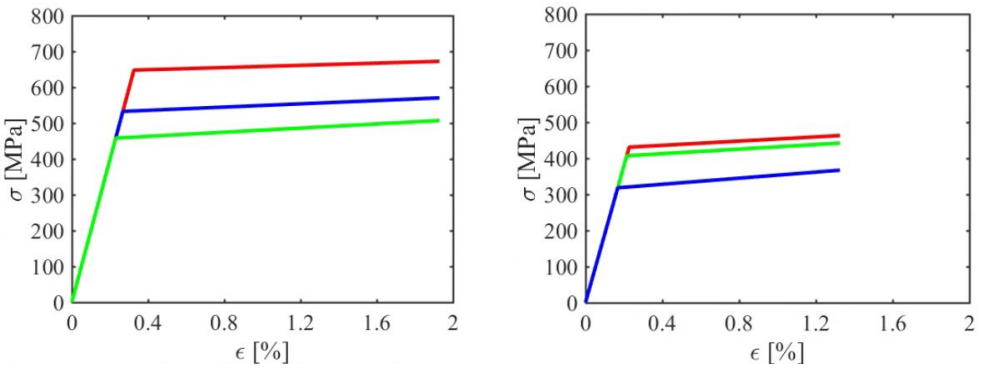

Figure 31: Stress-strain relationships according to the linear hardening model at BOL (0 dpa, green curve), 45 dpa (blue curve) and 90 dpa (red curve) for (a) 375°C and (b) 500°C .

3.3 Model of Inelastic Deformation by Swelling

Neutron-induced void and bubble swelling (f_v) is modeled as an inelastic isotropic strain. We will describe a simplified bi-linear swelling model based on the analysis of [33]. The diagonal components of the inelastic strain tensor ($\boldsymbol{\varepsilon}^{\text{in}}$), which correspond to volumetric swelling ($\boldsymbol{\varepsilon}^{\text{s}}$),

are all set to be equal, where:

$$f_v = \Delta V/V = \varepsilon^{\rm s}_{11} + \varepsilon^{\rm s}_{22} + \varepsilon^{\rm s}_{33} = 3e \tag{9}$$

$$\varepsilon^{\rm s}_{11} = \varepsilon^{\rm s}_{22} = \varepsilon^{\rm s}_{33} = e = \frac{1}{3} f_v \tag{10}$$

Thus, the total strain tensor is composed of an elastic component, ($\boldsymbol{\varepsilon}^{\rm e}$), an inelastic component ($\boldsymbol{\varepsilon}^{\rm in}$), and a thermal strain component, ($\alpha(T-T_0)\boldsymbol{I} = \alpha\Delta T\boldsymbol{I}$), where α is the coefficient of thermal expansion, and $\boldsymbol{I}$ is the identity tensor. The inelastic component is further decomposed into a volumetric swelling strain ($\boldsymbol{\varepsilon}^{\rm s}$), and a plastic strain ($\boldsymbol{\varepsilon}^{\rm p}$). One can then write:

$$\boldsymbol{\varepsilon} = \boldsymbol{\varepsilon}^{\rm e} + \boldsymbol{\varepsilon}^{\rm p} + \alpha\Delta T\boldsymbol{I} + \frac{f_v}{3}\boldsymbol{I} \tag{11}$$

And the constitutive relationship between stress and strain as:

$$\boldsymbol{\sigma} = \boldsymbol{C} : \boldsymbol{\varepsilon}^{\rm e} = \boldsymbol{C} : \left(\boldsymbol{\varepsilon} - (\boldsymbol{\varepsilon}^{\rm p} + \alpha\Delta T\boldsymbol{I} + \frac{f_v}{3}\boldsymbol{I})\right) \tag{12}$$

where $\boldsymbol{C}$ is the elastic constants tensor. The material properties in Equation 12 are generally functions of the triplet (Φ, T, r). However, not all the dependencies are available at the present time, and one has to make best estimates, consistent with current data and discuss the trends. Neutron swelling data at 500 °C has been thoroughly analyzed by [33], and several suggested data fits were discussed. Because of these uncertainties, and for simplicity of including the swelling strain into the structural model, we use here a bi-linear fit of the neutron displacement damage dose as following where U is the Heaviside function;

$$f_v = e_0(1 - U(\Phi - \Phi_0))(\frac{\Phi}{\Phi_0}) + U(\Phi - \Phi_0)(e_0 + s(\Phi - \Phi_0)) \tag{13}$$

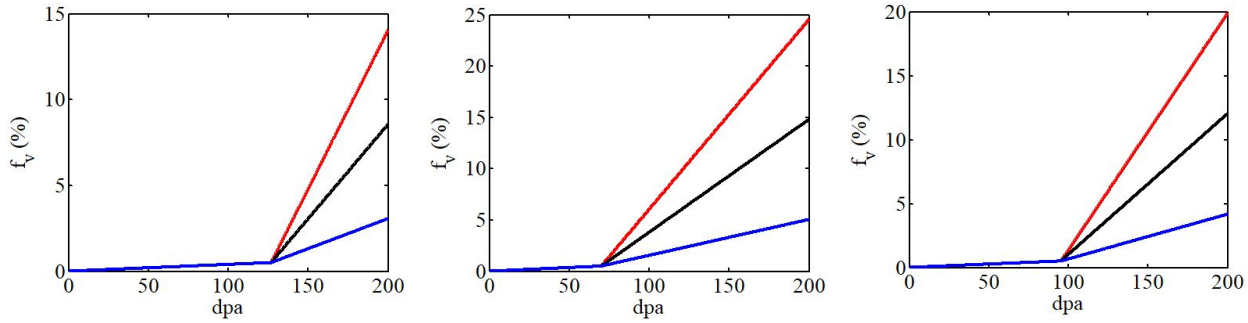

Figure 32: Void swelling (f_v) as a function of neutron displacement damage dose (ϕ) in dpa at (a) 350°C, (b) 500°C, and (c) 600°C considering worst case (red curve), reference case (black curve which is used in our simulations) and best case (blue curve).

The rate of volumetric swelling past the incubation dose Φ_0 is given by:

$$s = s_0 - 0.004r \tag{14}$$

Where s_0 is the swelling rate in the absence of helium, and the incubation dose is given by:

$$\Phi_0 = (a + br)\{1 - U(r - 40)\}\{1 + (c\frac{T - T_0}{T_0})^2\} \tag{15}$$

In these equations, the fitting parameters are: a=90, b=-2, c=3, T_0 = 500°C, s_0 = 0.15 (s_0, the swelling rate, has a min of 0.075 for best case and maximum of 0.225 for worst case), e_0 = 0.5 (minimum swelling at Φ_0), and r=10 (helium-to-dpa ratio). The results of this model are shown in Figure 32 at various temperatures, where the volumetric swelling of F82H is shown as a function of neutron displacement damage dose Φ. The swelling rate for F82H is very low below an incubation dose, and then accelerates at higher dose. There is considerable uncertainty in these predictions because of the lack of dedicated prototypical fusion irradiation facilities. This uncertainty is reflected in bounds for the swelling rate (minimum and maximum) that are consistent with current understanding [33]. Future updates of the current property predictions may be necessary, as more radiation effects data become available.

CHAPTER 4

Experimental Thermomechanics Background

The causes of thermal damage and fracture of materials exposed to a surface heat flux can be numerous. For example, when the heating (or cooling rate) of the surface is extreme, fracture can occur either during the heat up transient on the cold side of the material, or during the cool-down phase on the hot side of the material. The description of "thermal shock" is commonly used to describe these two possibilities, although they are physically driven by thermal expansion gradients in the first case, and by residual stresses in the second. Very brittle or even ductile materials can therefore undergo "thermal shock", depending on the nature of surface heating and any applied external boundary conditions. There are other possibilities as well, where fracture can be induced in materials, even at low-to-moderate heating rates. Such thermal damage and fracture, while is commonly not described as "thermal shock", must be understood and analyzed so as to ensure better component design. In this chapter, first I will introduce the HEFTY and all different sample fixtures that I designed and fabricated for verity of high-heat flux high-temperature testings. Also, I will discuss the experimental setups and measurement techniques. Then, I will provide the background for setting up thermomechanics experiments at high heat flux, considering the various possibilities that can influence thermal damage and fracture. The influence of residual stresses, thermal expansion mismatch, temperature gradients in brittle materials and effects of combined mechanical and cyclic thermal loading will be explored here.

4.1 The HEFTY Experimental Facility

The HEFTY is a low vacuum plasma chamber equipped with Praxair SG-100 Argon plasma arc-jet rated at 85 kW at atmospheric pressure. If one assumes that half of the rated power is delivered to a 5 cm^2 target, a theoretical upper limit of the surface heat flux could be on the order of 80 MW/m^2. However, as the sample moves away from the exit plane of the plasma gun, the maximum heat flux is expected to decrease due to an increase in the plume size and the concomitant decrease in the specific power in a spreading plasma. The objective of measuring the heat flux in the HEFTY chamber is to provide a more accurate distribution of the heat flux within the chamber.

This work is focused on designing controlled high-temperature cyclic loading experiments to investigate material failure under a variety of constrains (boundary condition) and loading schedules. A 3-axis precision linear stage (Figure 34) is designed to center the sample and remotely control the sample distance form the arc-jet during experiments. This, in turn, will define the magnitude and distribution of the heat flux on the sample. Three heat exchangers are installed inside the low-vacuum chamber to prevent components from overheating during tests. The first one is located at the top of the chamber before the exhaust valves, the second is around the precision linear stage stepper motor and the third one is near the arc-jet exit, as shown in Figure 33. Several Vacuum feedthroughs are added to the chamber for high-temperature strain gauges and thermocouples (K-type). A LabVIEW Virtual Instrument (VI) software is developed to process signals obtained from the thermocouples and strain gauges installed on the samples. The software outputs the signals to a live monitor, and can be programmed for a variety of thermal loading schedules during experiments. Experimental data are finally recorded for post-processing and analysis.

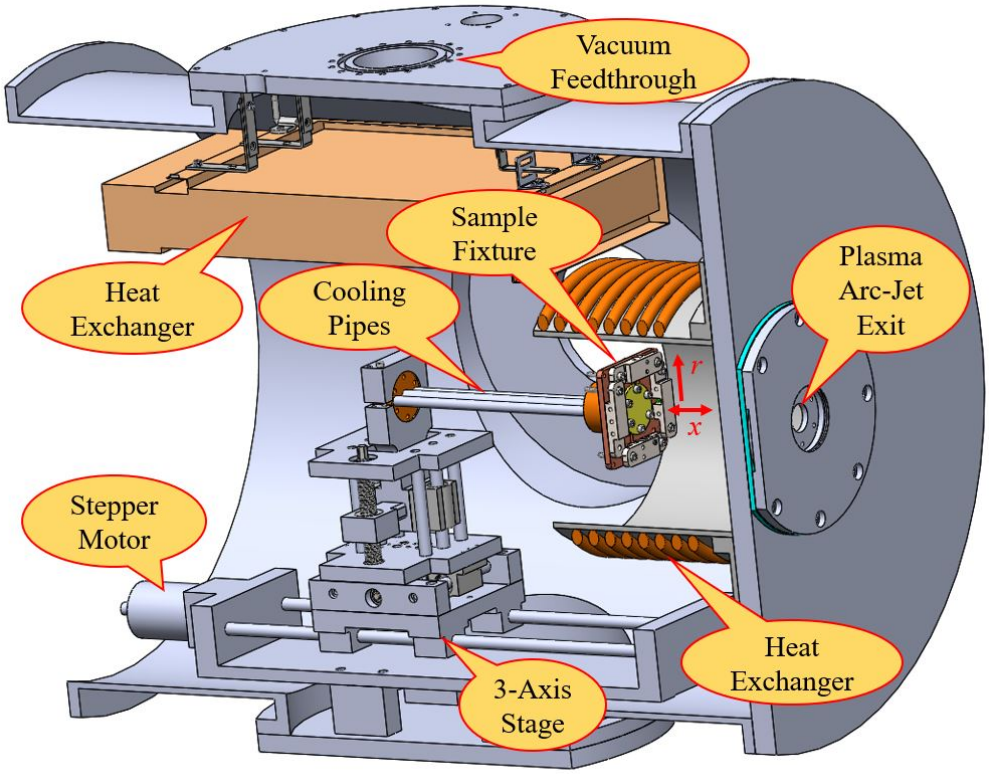

Figure 33: HEFTY chamber cross-section view showing the assembly of the sample fixture on the cooling pipes.

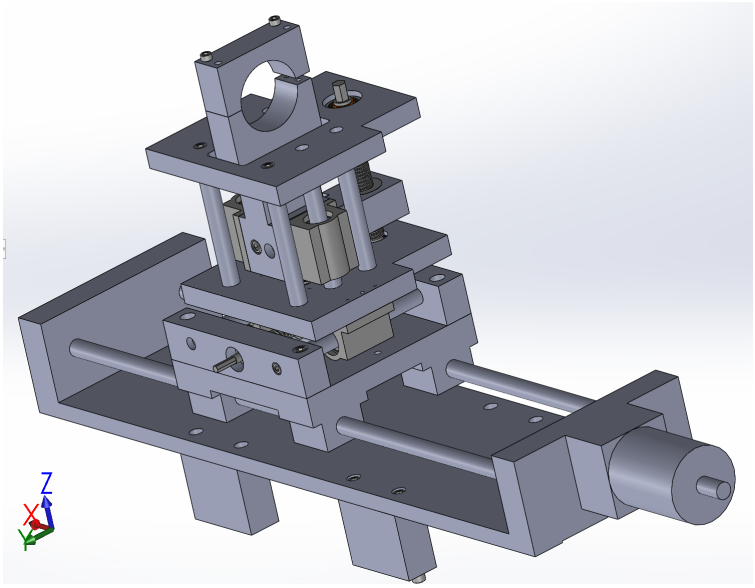

Figure 34: Design of 3-axis precision linear stage for centering the sample, changing the loading zone on sample and remote control of sample's distance from the arc-jet during experiments.

In this work several sample fixtures (Figure 35) were designed and fabricated for use

in the HEFTY chamber for a variety of high temperature test conditions. These include free thermal expansion, thermal shock, fully constrained boundary conditions, local high-heat flux loading, thermal expansion mismatch, water-cooled high heat flux plasma facing modules, and combined mechanical and thermal loading fixtures. In order to introduce deep temperature gradients across samples, all the sample fixtures include a CuCrZr cooling plate, which is assembled on HEFTY's cooling pipes (Figure 33) that are connected to a room temperature water-jet with $\approx$ 4 GPM flow rate. The sample is mounted on the CuCrZr cooling plate and is exposed to cyclic high heat flux from the arc-jet on its top face, while being continuously cooled on the back face where it is connected to the cooling plate. In order to reduce undesired oxidation in these tests, a vacuum pump is used to take HEFTY chamber to 0.01 torr and then the chamber is partially filled up with argon gas up to 100 torr before starting each test. The sample fixtures shown in Figure 35 will be discussed in greater detail in the following sections, including some typical experimental results. Extensive experimental results for free thermal expansion, fully constrained, and local loading fixtures are presented in Chapters 6 and 7 and for water-cooled high-heat flux plasma-facing module in [36].

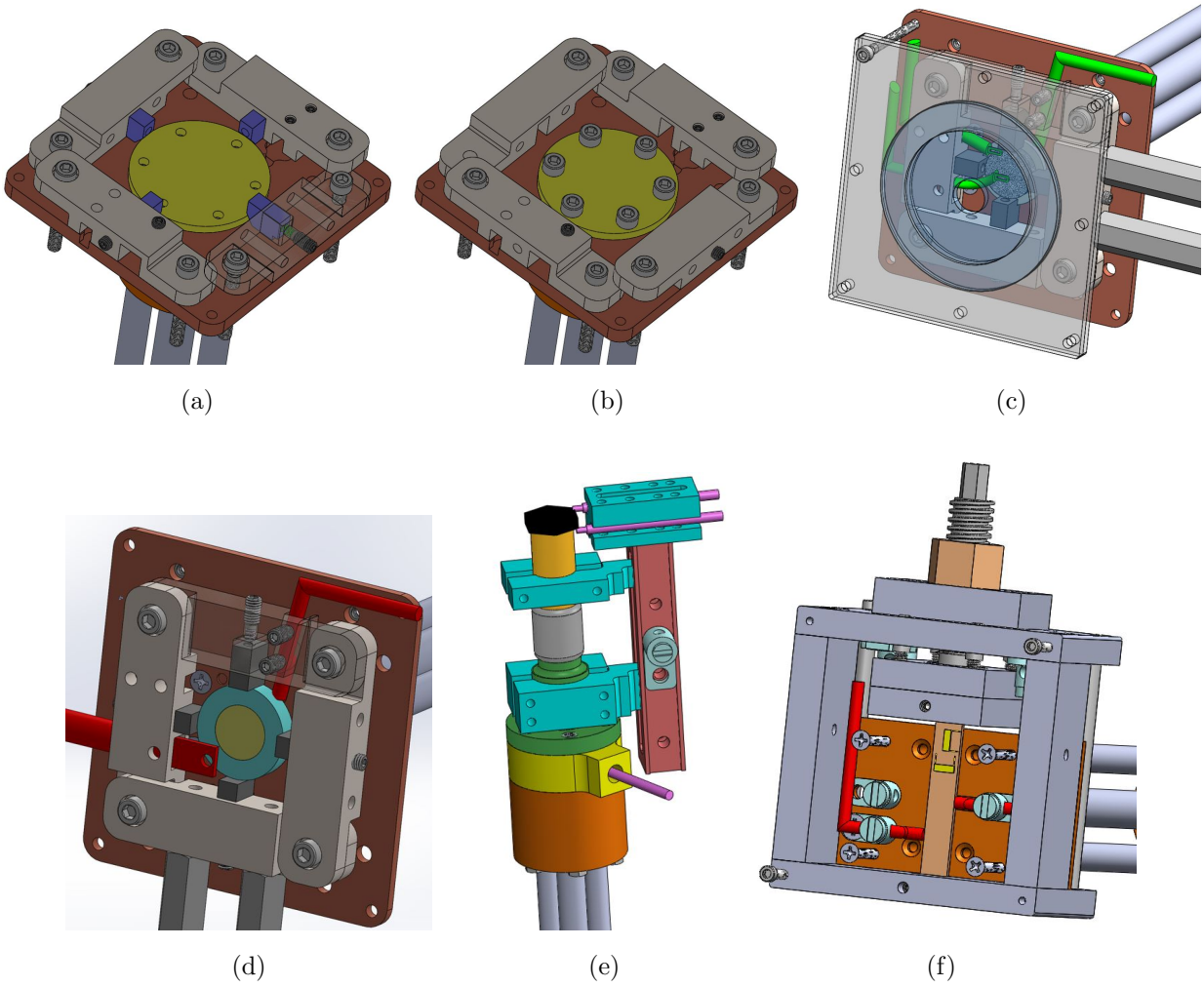

Figure 35: (a) Free thermal expansion and thermal shock, (b) fully constrained, (c) local loading, (d) thermal expansion mismatch, (e) water-cooled high-heat flux plasma-facing module and (f) combined mechanical and thermal loading sample fixtures designed for HEFTY high temperature cyclic experiments.

4.2 Residual Stresses

Accumulated residual strain can cause severe damage and cracking of materials subjected to high heat flux. Components that are fully constrained in their service assembly can experience compressive plastic strain during heat-up. Also, local loading and material self-constraint can cause compressive plastic strain during thermal loading. Compressive plastic strain, which stays as permanent deformation in the material, can cause tensile stress during material cool-down. Depending on the loading conditions and magnitude of the accumulated

plastic strain, the residual tensile stress can cause micro-cracks or even catastrophic failure and fracture in the material during cool-down.

4.2.1 Residual Stresses in Heated Bars and Disks

An experimental set-up has been developed to explore the role of residual stresses on fracture. Experiments can be performed on two different configurations to determine the effects of residual stresses on a constrained bar, as shown in Figure 36 and on a constrained disk, as shown in Figures 37. The stress-strain curve of a bar clamped at both ends under thermal loading is shown in Figure 38. It can be seen that after thermal loading-unloading, the total strain goes back to zero due to fixed boundary conditions. This causes the development of a tensile stress during cool-down. This is a result of fully elastic unloading of the material, after it accumulated a degree of plastic deformation. Depending on the magnitude of the accumulated plastic strain, unloading may result in a tensile stress below the yield point for a small amount of residual strain, or above the yield point if the residual strain is large. In all cases, the residual stress can be calculated using an elastic-perfectly-plastic or a linear hardening model for the post-yield behavior.

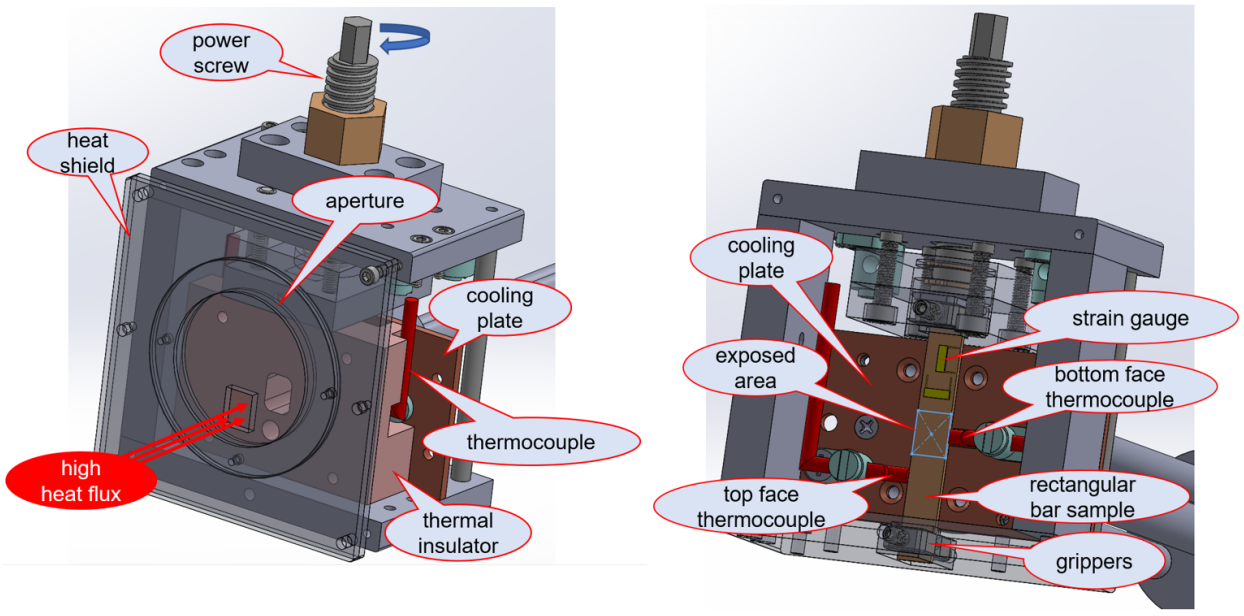

Figure 36: Sample fixture designed to study combined thermal and mechanical loading and residual stresses in a constrained bar.

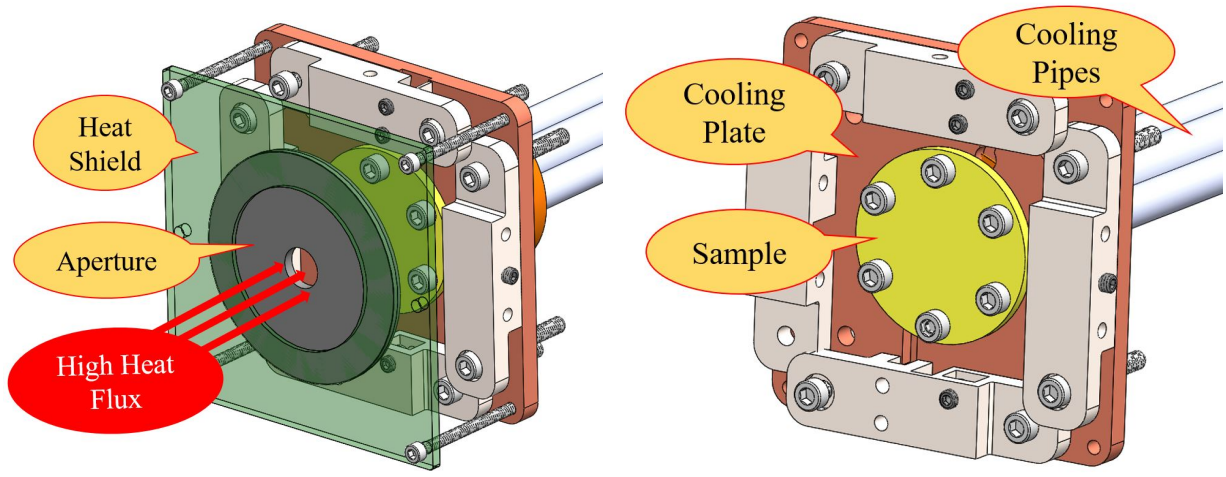

Figure 37: Sample fixture designed to fully constrain a disk on its perimeter subjected to local high heat flux loading showing (a) the heat shield and aperture defining the thermal loading zone and (b) sample assembly on the cooling plate.

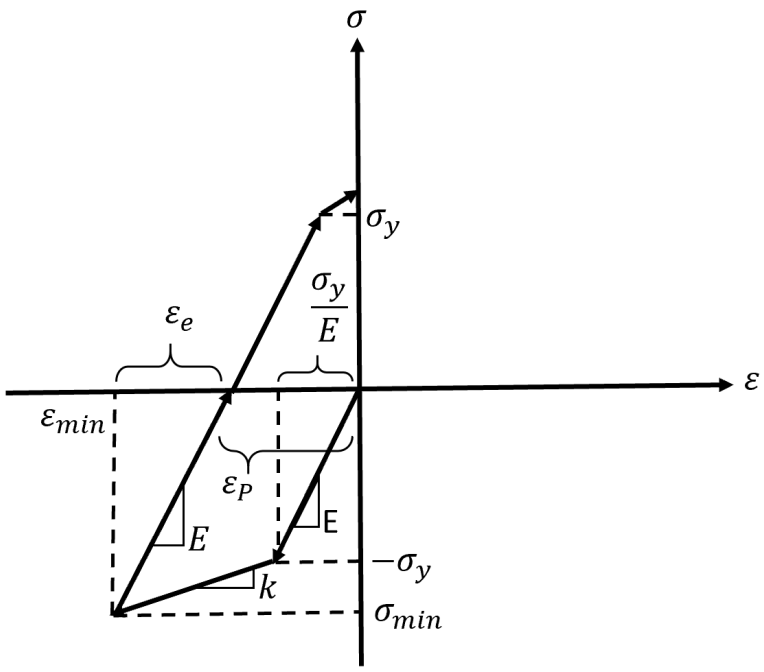

Figure 38: Stress-strain curve for constrained bar under thermal loading

The total strain (ε_{tot}), which is sum of thermal (ε_t), elastic (ε_e), and plastic (ε_p) strains (equation 16) must be zero at the end of a full thermal cycle due to the fixed boundary conditions of the bar. The plastic strain (ε_p) at the end of the heat-up phase can be found

as:

$$\varepsilon_{tot} = \varepsilon_t + \varepsilon_e + \varepsilon_p = 0 \tag{16}$$

$$\alpha\Delta T + \frac{\sigma_{min}}{E} + \varepsilon_p = 0 \tag{17}$$

$$\varepsilon_p = -\left[\alpha\Delta T + \frac{\sigma_{min}}{E}\right] \tag{18}$$

where ΔT is the temperature difference from the reference conditions. During cool-down, the compressive plastic strain ε_p stored in the material and the elastic strain must add up to zero, since the bar is fixed at its boundaries. This introduces a tensile stress in the material upon cool-down, as follows:

$$\varepsilon_e + \varepsilon_p = 0; \quad , \varepsilon_e = \alpha\Delta T + \frac{\sigma_{min}}{E} \tag{19}$$

$$\sigma_{cool\ down} = E\alpha\Delta T + \sigma_{min} \tag{20}$$

It can be seen form Figure 38 that for an elastic-perfectly plastic material model, σ_{min} is equal to the yield strength (-σ_y) of the material as shown in (i). On the other hand, for the linear hardening material model, σ_{min} can be obtained from the tangent modulus k as described in (ii).

(i) Elastic-perfectly-plastic (EPP) material model:

$$\sigma_{\text{cool down, EPP}} = E\alpha\Delta T - \sigma_y \tag{21}$$

(ii) Linear hardening (LH) material model:

It can be seen from Figure 38 that ε_{min} is composed of elastic and plastic components.

$$\varepsilon_{min} = \varepsilon_e + \varepsilon_p \tag{22}$$

ε_{min} can be rewritten as:

$$\varepsilon_{min} = -\varepsilon_t = -\alpha\Delta T \tag{23}$$

Also, from figure 38, σ_{min} can be calculated as:

$$\sigma_{min} = -\sigma_y - k\left[|\varepsilon_{min}| - \left|\frac{\sigma_y}{E}\right|\right] \tag{24}$$

Replacing σ_{min} in equation 20, the tensile stress at cool-down can be found as:

$$\sigma_{cool\ down,\ LH} = E\alpha\Delta T - \sigma_y - k\left[\alpha\Delta T - \frac{\sigma_y}{E}\right] \tag{25}$$

$$\sigma_{cool\ down,\ LH} = (E-k)\,\alpha\Delta T - \left(1 - \frac{k}{E}\right)\sigma_y \tag{26}$$

The calculated $\sigma_{cool\ down}$, along with an estimated pre-existing flaw size, can be used to obtain stress intensity factors and to compare with the fracture toughness so as to determine whether crack propagation is likely to take place during cool-down.

4.2.2 Residual Stress Test

A 1.6 mm thick tungsten bar is tested under high heat flux in HEFTY utilizing sample fixture shown in Figure 36 to study the effects of residual stress on tungsten. The experimental setup is shown in Figure 39a and 39b. It can be seen that the tungsten bar is fully constrained at both ends by grippers and is exposed to high heat flux through an aperture opening. The cooling plate under the tungsten bar is continuously being cooled by a water jet. Three k-type thermocouples ch1, ch2 and ch3, shown in Figure 39a, are installed on the tungsten bar and their signals are processed by the developed LabVIEW VI to monitor thermal loading during the experiment and output temperature measurements for further analysis. Temperature readings of this experiment are shown in Figure 40.

This experiment can be repeated for different applied heat flux and thermal loading by changing the HEFTY plasma arc-jet ON and OFF times, changing the sample distance from the plasma arc-jet by the remote controller shown in Figure 34, or by changing the tungsten aperture shown in Figure 39b to increase the exposed area on the sample. Performing this experiment allows a better understanding of the extent of plasticity and residual stresses in tungsten due to high heat flux impinging on constrained components. Residual stress tests on tungsten disks are discussed in great detail in section 7.5.2.

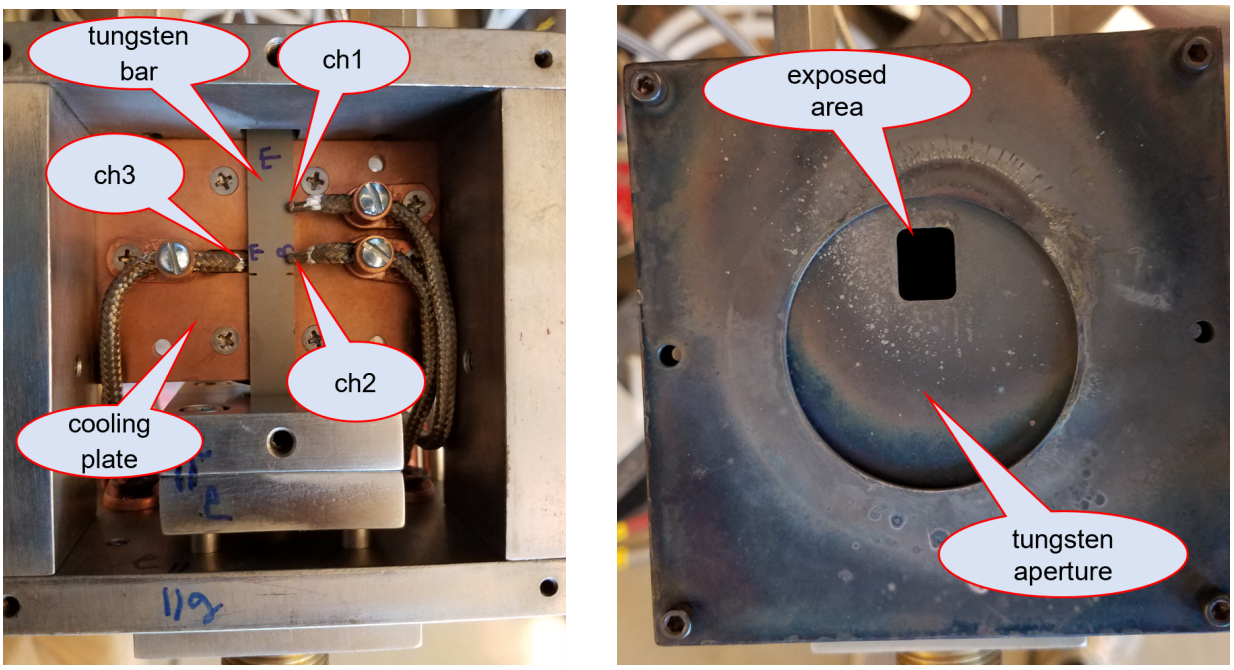

(a) (b)

Figure 39: Residual stress test setup for a tungsten bar. (a) Thermocouples setup showing ch1 located at the exposed face 15 mm from the center, ch2 located at the exposed face center of the sample and ch3 located at cooled face center of the sample. (b) Heat shield and tungsten aperture.

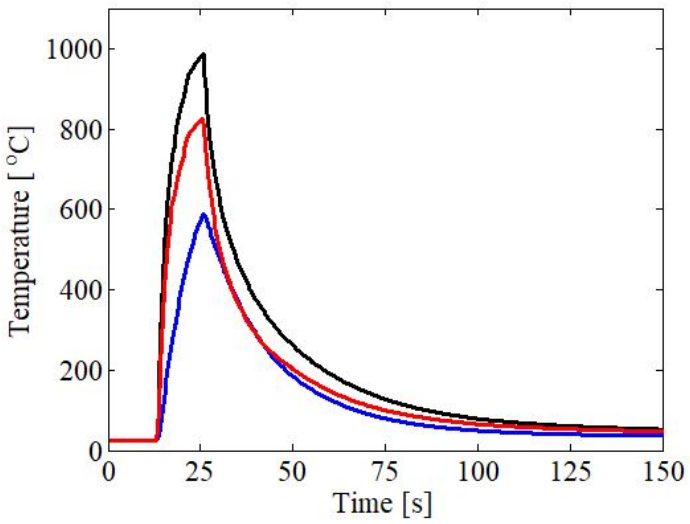

Figure 40: Temperature measurements on the tungsten bar during residual stress test. Temperature measurements from ch2 located at the center of W bar exposed face is plotted in black, measurements from ch1 located at the exposed face of W bar 15 mm from center of loading is plotted in red and, measurements from ch3 located at the center of W bar cooled face is plotted in blue.

4.3 Thermal Expansion Mismatch

Thermal fracture is sometimes observed to occur when two adjacent materials expand at different rates when heated or cooled down. The extent by which thermal expansion mismatch can damage high temperature components upon their assembly can be tested in HEFTY. This is accomplished using the designed sample fixture and experimental setup shown in Figure 41.

4.3.1 Mismatch Stresses in a Disk-Ring Assembly

In this experiment, a ring and disk assembly are fabricated from different materials and are exposed to a high heat flux to study thermal damage at the interface. Thermal expansion mismatch between the disk and ring can introduce significant interfacial pressure that can lead to fracture. The following equations can be used to approximate the stress at the inner radius of the ring due to the thermal expansion mismatch .

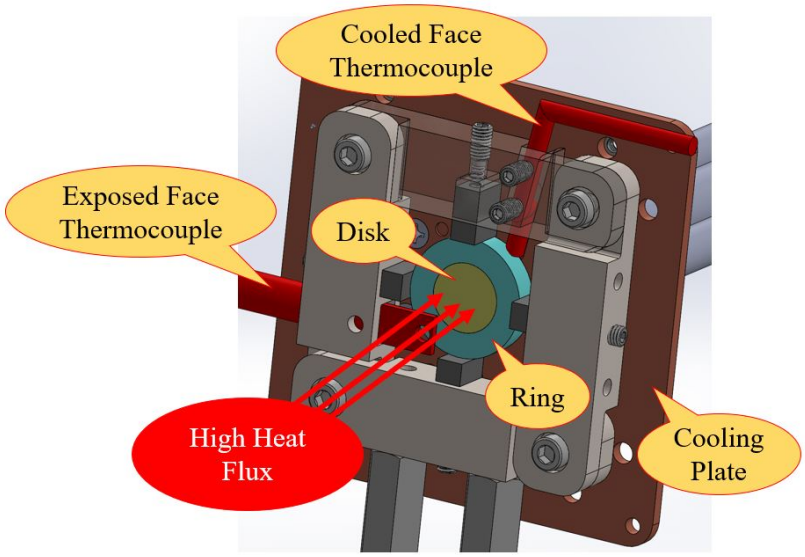

Figure 41: Thermal expansion mismatch test for assemblies at high temperature.

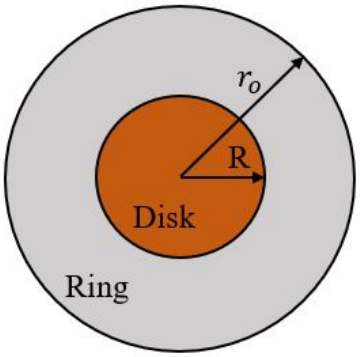

Figure 42: Disk and ring assembly

The radial interference(δ) between the disk and ring induced by thermal loading can be found as the difference between the expanded radii of the disk (R'_D) and ring (R'_R):

$$\delta = R'_D - R'_R \tag{27}$$

$$\delta = R_D\left(1 + \alpha_D \Delta T\right) - R_R\left(1 + \alpha_R \Delta T\right) \tag{28}$$

At the reference (room) temperature, the inner radius of ring is the same as disk radius (R);

$$\delta = R\left[\alpha_D - \alpha_R\right]\Delta T \tag{29}$$

where;

R'_D: Radius of disk after being exposed to heat

R'_R: The inner radius of Ring after being exposed to heat

R: Interface radius before being exposed to heat

r_o: Outer radius of the ring

α_D: Thermal expansion coefficient for the disk

α_R: Thermal expansion coefficient for the ring

ΔT: Temperature rise form a reference temperature

The interfacial pressure (p) and hoop stress on the inner radius of the ring (σ_t) due to the radial interference δ can be obtained as:

$$p = \frac{\delta}{R\left[\frac{1}{E_R}\left(\frac{r_o^2+R^2}{r_o^2-R^2} + \nu_R\right) + \frac{1}{E_D}\left(1 - \nu_D\right)\right]} \tag{30}$$

$$\sigma_t = p\frac{r_o^2 + R^2}{r_o^2 - R^2} \tag{31}$$

where E_D, E_R are Young's modulus and ν_D ,ν_R are the Poisson ratio for the disk and ring, respectively. Having σ_t, one can determine failure and fracture of the ring based on its fracture toughness. A thermal expansion mismatch test is performed using a specially-designed apparatus on a boron nitride (BN) ring and a CuCrZr disk, as summarized below.

4.3.2 Thermal Expansion Mismatch Test

Thermal expansion can cause pressure at interface of assemblies leading to crack propagation and failure. This can be prevented either by careful material selection for assembly considering components thermal expansion coefficients and assembly gap at interface or by using foam structures instead of bulky material to compensate for induced pressure via ligaments deformation. However, this needs to be tested carefully for different loading conditions.

In this section an experimental result is presented for assembly of CuCrZr disk and BN ring to study the magnitude and effect of interface pressure. Figures 43 shows the experimental setup for this test. It can be seen that BN ring and CuCrZr disk assembly are placed between spring loaded clamps to allow free radial expansion for assembly under thermal loading. Thermocouples are placed on heating and cooling face of materials to measure their temperatures during the experiment. Temperature measurement presented in Figure 44 shows a maximum of 1150°C on CuCrZr disk and 900°C on BN ring. Considering an average temperature of 1000°C at interface, equation 30 yields 333 MP pressure at interface which can cause 676 MPa stress in hoop direction at inner radius of BN ring according to equation 31. This stress is significantly higher than BN flexural strength (59 MPa) causing crack initiation and propagation on BN ring at two locations as shown in Figure 45.

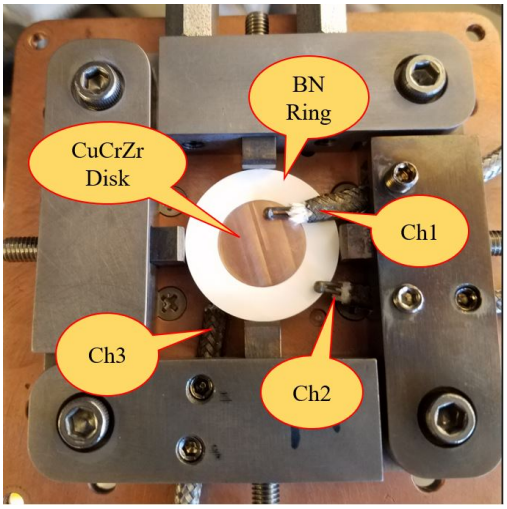

Figure 43: Thermal expansion mismatch test setup for BN ring and CuCrZr disk assembly.

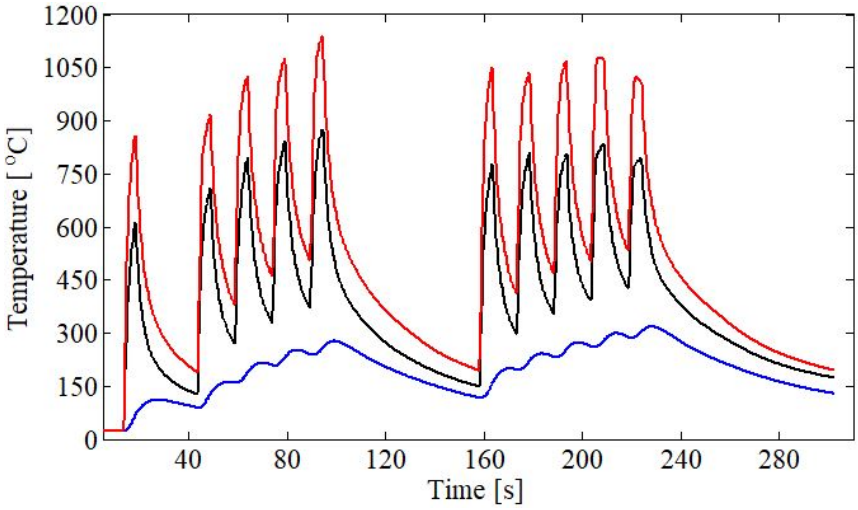

Figure 44: Temperature measurements on BN ring and CuCrZr disk during thermal expansion mismatch test. Temperature measurements of Ch1 located at CuCrZr disk exposed face 5 mm from center of loading is plotted in red, measurements of Ch2 located at BN ring exposed face 13 mm from center of loading is plotted in black and measurements of Ch3 located at BN ring cooled face is plotted in blue.

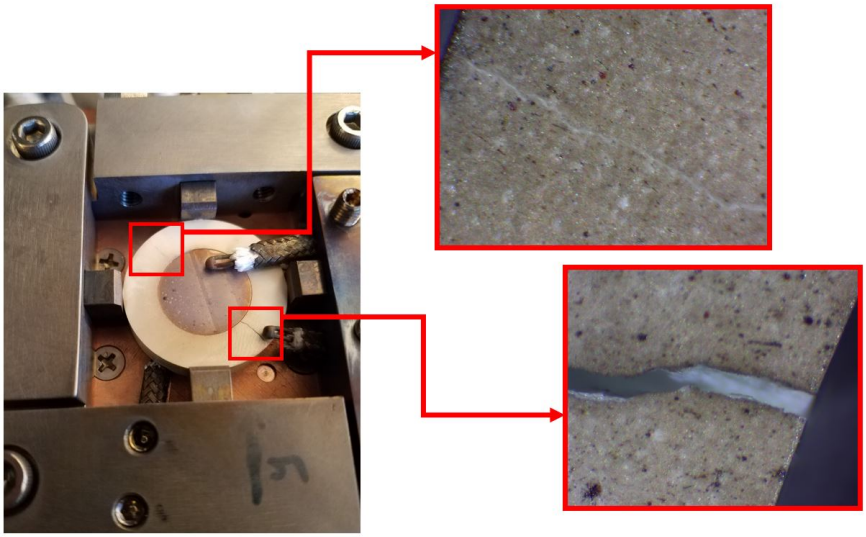

Figure 45: Cracks observed on BN ring due to thermal expansion miss-match between BN ring and CuCrZr disk.

4.4 Temperature Gradient Effects

High heat flux facing components usually undergo significant temperature difference across their thickness where one side is exposed to the heat flux and the opposite side is being cooled continuously. Depending on the placement of the component on its assembly, the component can experience free thermal expansion or may be externally constrained building up thermal stresses. Following section will discuss the difference between these two cases by a simple example.

4.4.1 Single-Sided Heated Strip Model

A simple 2D study is conducted here to distinguish the differences between these two cases.

(i) *Free thermal expansion*:

Components having a temperature gradient across their thickness can experience free thermal expansion with no thermal stress if the deformation is not restricted and constrained. Figure 46 shows a simple 2D study of a rectangular cross section of a component subjected to 900 °C temperature difference across its thickness. It can be seen

that the component is free to expand in x-direction from its right side where the top face experience greater expansion as compared to the bottom face due to its higher temperature and this causes a shape change and the bowing observed on the deformed configuration shown in Figure 46. Having free thermal expansion results in no stress, as shown here.

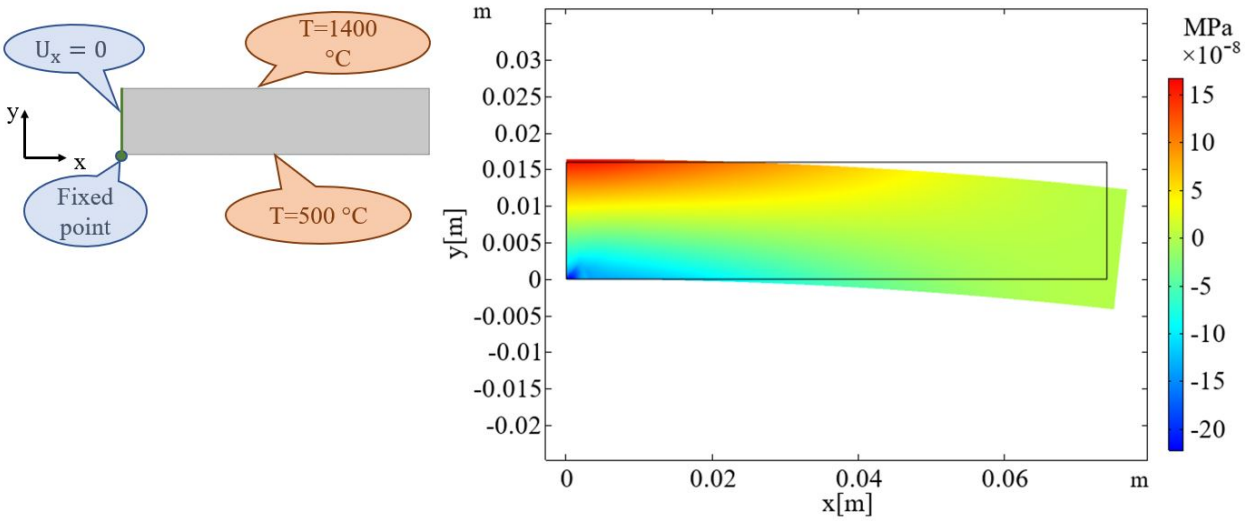

Figure 46: Free thermal expansion of a heated strip showing x-component of the stress tensor.

(ii) *Constrained out-of-plane deformation*:

If the component is constrained from free deformation and bowing (no displacement in the out-of-plane (y-direction)), the hot material on the top face would be constrained by the cool material on the bottom face. Therefore, the material on the top face experiences compression while the material on the bottom face experiences tension so as to reach to the same amount of elongation as the top face. This happens either by an elastic strain along the x-axis, plastic deformation along the x-axis or crack opening on the bottom face. It can be seen from Figure 47 that the stress field produced by a thermal gradient is similar to the stress field of an applied moment (compressive stress on one side and tensile stress on the other side). This can be used to compare some experimental results under thermal loading with analytical models having an applied mechanical moment.

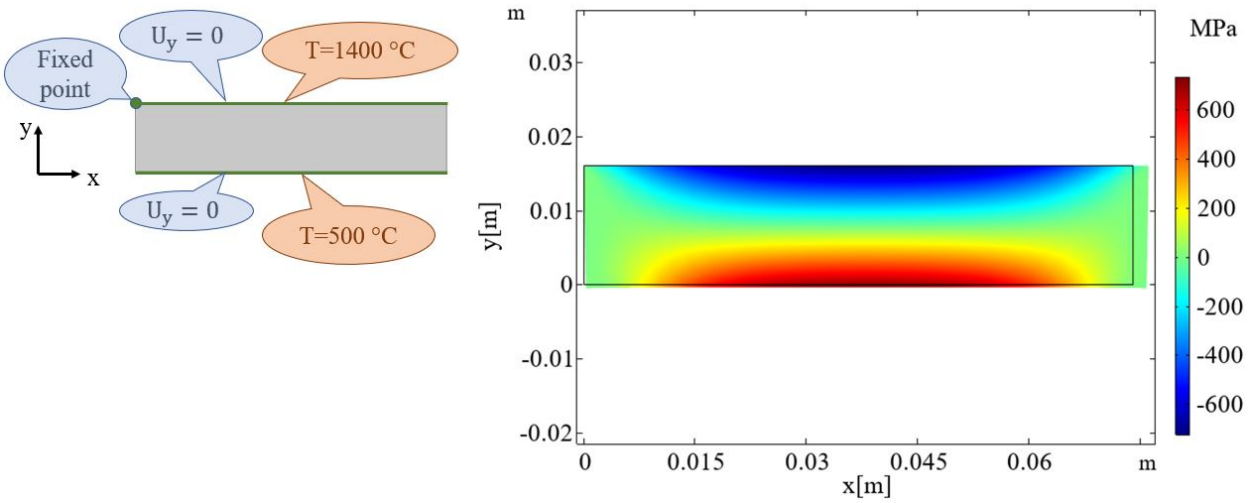

Figure 47: Stress distribution (x-component of stress tensor) on a constrained strip under temperature gradient.

The following equations can be used to estimate the equivalent moment required to produce a stress field similar to the one produced by a heat flux q'' through the thickness Δy of a beam:

$$q'' = k\frac{\Delta T}{\Delta y} \tag{32}$$

$$|\varepsilon_{top}| = |\varepsilon_{bottom}| = \left|\frac{\alpha \Delta T}{2}\right| \tag{33}$$

$$|\sigma_{T\ top}| = |\sigma_{T\ bottom}| = \left|\frac{E\alpha \Delta T}{2}\right| \tag{34}$$

$$|\sigma_{M\ Top}| = |\sigma_{M\ bottom}| = \left|\frac{M\Delta y/2}{I}\right| \tag{35}$$

$$\left|\frac{E\alpha \Delta T}{2}\right| = \left|\frac{M\Delta y/2}{I}\right| \tag{36}$$

$$M = \frac{EI\alpha \Delta T}{\Delta y} = \frac{EI\alpha q''}{k} \tag{37}$$

where M is the moment, E is the Young's modulus, α is the thermal expansion coefficient, I is the second moment of inertia, k is the thermal conductivity, ΔT is temperature difference across the thickness of the beam, σ is the stress and ε is the strain.

4.4.2 Temperature Gradient Test

The sample fixture shown in Figure 36 can be used to constrain and push a rectangular sample on the cooling plate by a ceramic thermal insulator. The experimental setup is shown in Figures 48a, 48b and 48c, where a SiC/SiC composite sample is constrained from bending. It can be seen that the SiC/SiC sample is free at both ends and is constrained from bending using the ceramic insulator pushing it form the top (Figure 48b). The heat flux impinges on the top face of the sample from an aperture opening and the bottom face of the sample is in a perfect contact with the cooling plate, which is continuously cooled by a water jet. Thermal loading is shown in Figure 49. It can be seen that during the ON-time of the plasma arc-jet (peaks on the figure), the exposed face of the sample reads an average temperature of 690°C (channel 2 reading an average peak of 950°C at the center of exposed face and channel 1 reading an average peak of 430°C on exposed face 15 mm from the center of loading) and the cooling face of sample reads an average of 37°C during ON-time from channel 3 placed underneath the sample at its center. This provides a temperature difference of 653°C across the sample during the ON-time. Having this ΔT in equation 34 leads to 215 MPa tensile stress on the cooled face of the sample as shown:

$$\sigma_{\text{T bottom}} = \frac{E\alpha\Delta T}{2} = \frac{220\,[GPa] \times 3 \times 10^{-6}\,[1/K] \times 653[K]}{2} = 215MPa \qquad (38)$$

This tensile stress is sufficient for crack propagation in SiC/SiC composite, since the matrix cracking stress takes place at 100 MPa. The damage and micro-cracks observed in this experiment are shown in Figure 50. This experiment is performed to test the capability of designed sample fixture to apply the required conditions for a thermal gradient test.

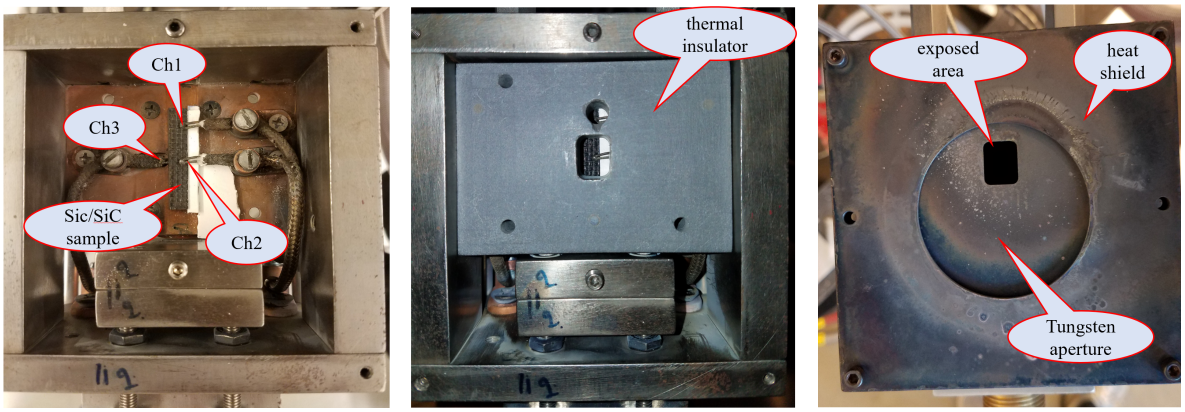

(a) (b) (c)

Figure 48: Temperature gradient test on SiC/SiC ceramic matrix composite. (a) Thermocouples setup showing ch1 is located at the exposed face 15 mm from center of loading, ch2 is located at the center of exposed face and ch3 is located at the center of cooling face. (b) Thermal insulator pushing the sample on cooling plate preventing it from bowing out under high temperature gradient. (c) Heat shield and aperture providing desired exposure area on center of sample and keeping CuCrZr cooling plate from direct exposure to increase temperature difference across the thickness of the sample.

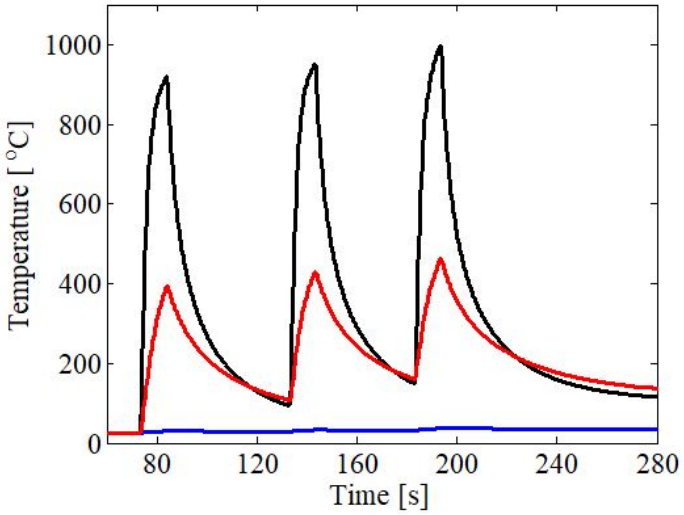

Figure 49: Temperature measurements on Sic/Sic bar during temperature gradient test. Temperature measurements from Ch2 located at the center of exposed face is plotted in black, measurements form Ch1 located at the exposed face 15 mm from center of loading is plotted in red and measurements from Ch3 located at the center of cooled face is plotted in blue.

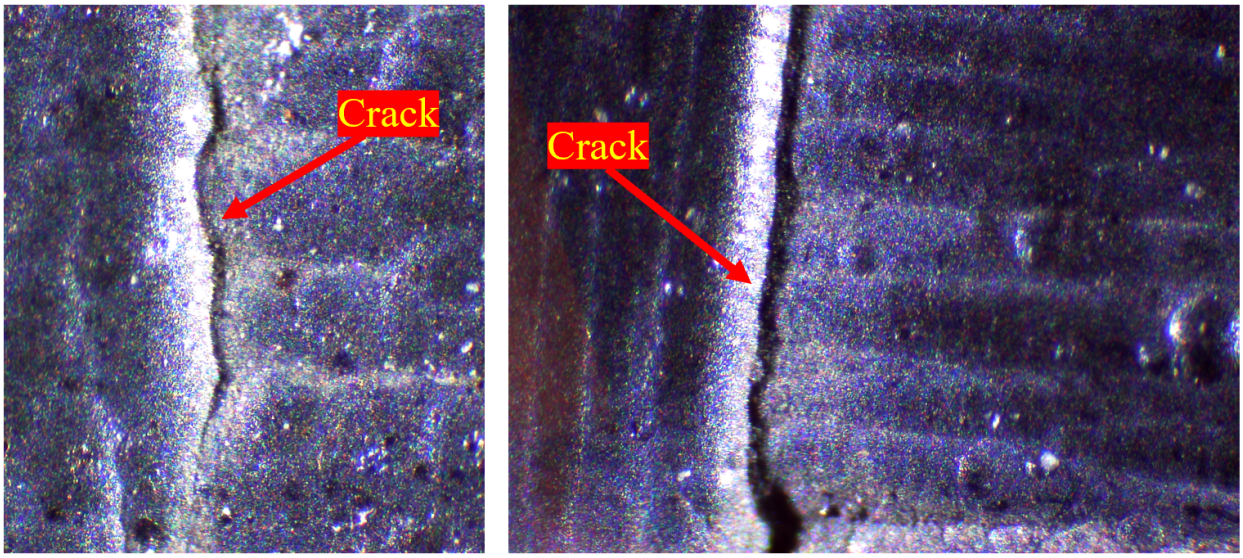

Figure 50: Micro-cracks and damage on Sic/Sic bar after temperature gradient test.

4.5 Effects of Simultaneous Mechanical and Thermal Loading

Using tungsten in high heat flux facing components brings concerns about the affects of combined mechanical and thermal loading on its deformation and potential failure. Having an applied constant mechanical load and a cycling thermal load can cause severe failure in tungsten due to continues deformation of material with each cycle (ratcheting). These conditions are studied in section 3.1 for a pressurized tube having a temperature gradient across its wall due to thermal cyclic loading. This geometry can be simplified as a slab under uni-axial loading, and having a linear temperature distribution across its thickness, as shown in Figure 17. The purpose of this experimental work is to utilize HEFTY (Figure 33) along with a sample fixture designed for combined loading (Figure 36) to test tungsten bars under a variety of loading conditions. The objective here is to induce stress states that can result in the material being in one of the Bree diagram regimes, shown in Figure 18.

The constant mechanical load can be applied by a power screw, as shown in Figure 36, and a temperature gradient can be introduced by the high heat flux of the plasma arc-jet in HEFTY. This creates a simplified uni-axial loading condition, shown in Figure 17. One can follow the map shown in Figure 51 to investigate various stress regimes introduced by Bree

(Figure 18 [21]) on a 5 mm thick tungsten bar in HEFTY.

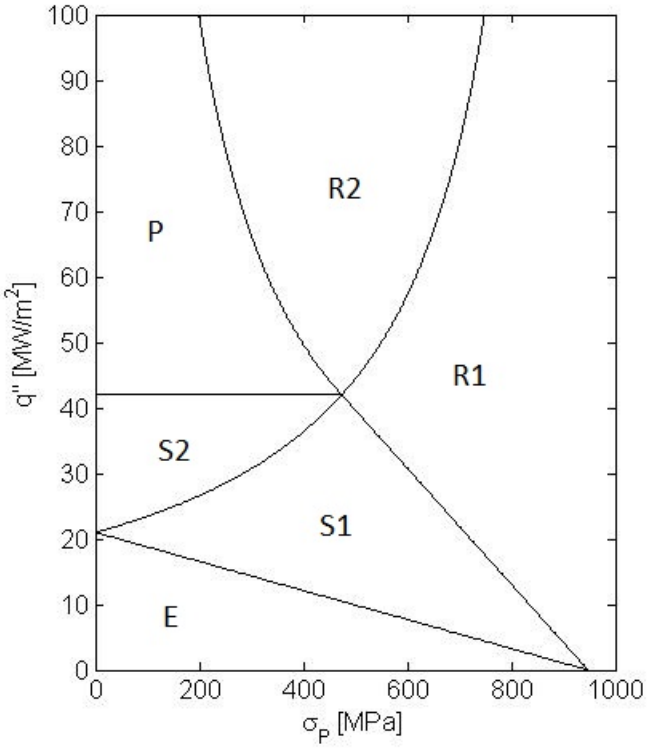

Figure 51: Loading map in HEFTY to investigate stress regimes on a 5 mm thick tungsten bar.

CHAPTER 5

Design and Calibration of the Heat Flux Sensor

In order to have a better understanding of material response under high heat flux loading in HEFTY, and to perform detailed analytical calculations and finite element (FE) simulations, one needs to have a good determination of the magnitude of the applied heat flux and its spatial and temporal distributions. The HEFTY arc-jet heat flux is assumed to have an exponential decay in radial direction (r shown in Figure 52a), with its maximum at the core of the plasma ($r = 0$). Also, this redial decay is function of the axial distance (distance x shown in Figure 52a) from the arc-jet. In addition, the magnitude of the heat flux at the plasma core ($r = 0$) is function of axial distance x (Figure 52a) from the arc-jet exit plane.

I will discuss here the design of a heat flux sensor that I designed and fabricated in order to measure the temporal and spatial distributions of the heat flux within the HEFTY plasma chamber. Measuring extreme heat flux requires careful experimental analysis so as not to melt the heat flux sensor. In this work, the sensor is designed with active cooling, where the slug is in thermal contact with a cooling plate from its bottom face (Figure 52b). Active cooling allows the use of materials with low melting point and high thermal conductivity in slug fabrication. The slug in this sensor is fabricated from a CuCrZr alloy with ≈ 1070 °C melting point and ≈ 320 $w/(m.K)$ thermal conductivity [37]. The advantage of having an actively cooled heat flux sensor is that it can be exposed to the arc-jet plasma for long duration without melting. The downside of this kind of sensors is that the heat loss to the back side cooling plate needs to be approximated in heat flux calculations.

After discussing the heat flux sensor, a designed experiment will be discussed to determine the radial distribution of heat flux at several axial distances from the arc-jet exit plane. The heat flux sensor is assembled in HEFTY, as shown in Figure 52, and several tests are

performed at each axial distance starting at 8.9 cm from the arc-jet exit plane to 3.8 cm with 1.27 cm increments.

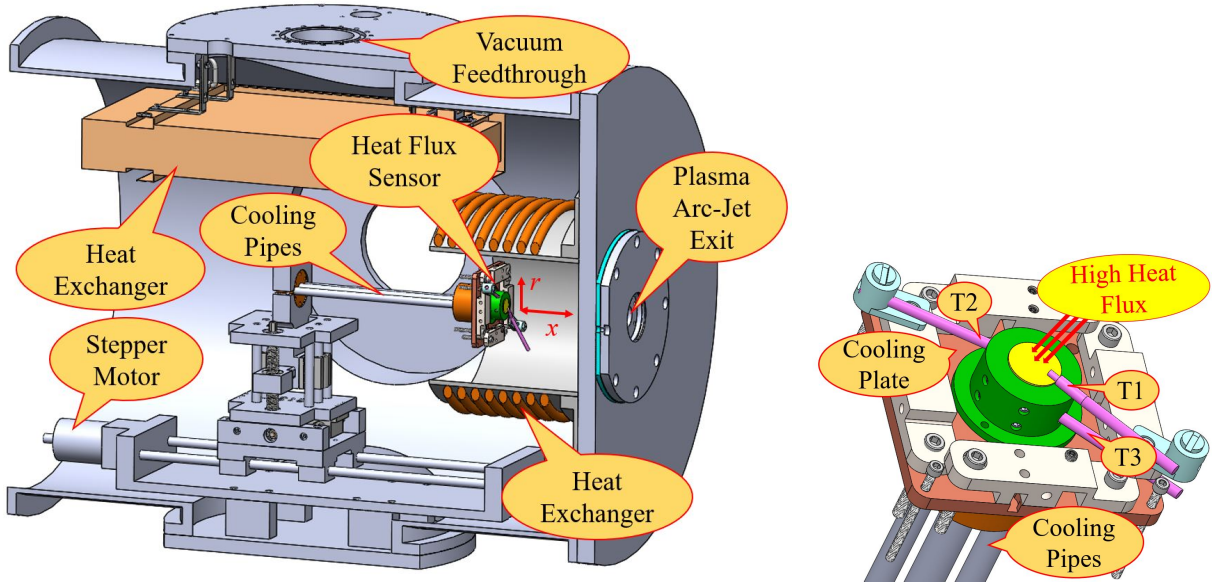

(a) (b)

Figure 52: (a) Assembly of the heat flux sensor in HEFTY and (b) The heat flux sensor mounted on the HEFTY cooling plate.

5.1 Heat Flux Sensor (Cooled CuCrZr Slug)

In order to estimate the heat flux in HEFTY series of tests are performed at each distance form arc-jet using the designed heat flux sensor. In these tests HEFTY's chamber is taken to vacuum (0.01 torr) and then filled partially with argon to 100 torr to reduce oxidation. In order to consider the influence of chamber back pressure on the magnitude of the arc-jet heat flux, we performed the tests once at 100 torr (cycle 1) and once at 400 torr (cycle 2) and then computed the heat flux for comparison (Figure 54b). This section will discuss the design of the heat flux sensor and data reduction methods used in heat flux determination.

The heat flux sensor is fabricated of a CuCrZr slug and Cu mounting with a 1.3 mm air gap between them. The slug has an overhanging section on the top to prevent direct flow of hot gas between the slug and mounting. This sensor utilises three thermocouples: one of them is located at the top face of the slug, while the other two are embedded inside

the slug. All thermocouples are secured with set screws on the mounting and are tested for good connection. The slug is fixed in the mounting using eight cone-point set screws in two rows, as shown in Figure 53a. This is to minimize surface contact between the slug and the Cu mounting. The heat flux sensor cross section is shown in Figure 53b, including its key dimensions. The sensor is installed in the HEFTY chamber as shown in Figure 52. The sensor faces the arc-jet while being mounted on the cooling plate. A series of tests were performed at distances of 8.9 cm from arc-jet to 3.8 cm, with 1.27 cm increments. The temperature measurements at each distance from the arc-jet were recorded using the developed LabVIEW VI and were used in heat flux calculations.

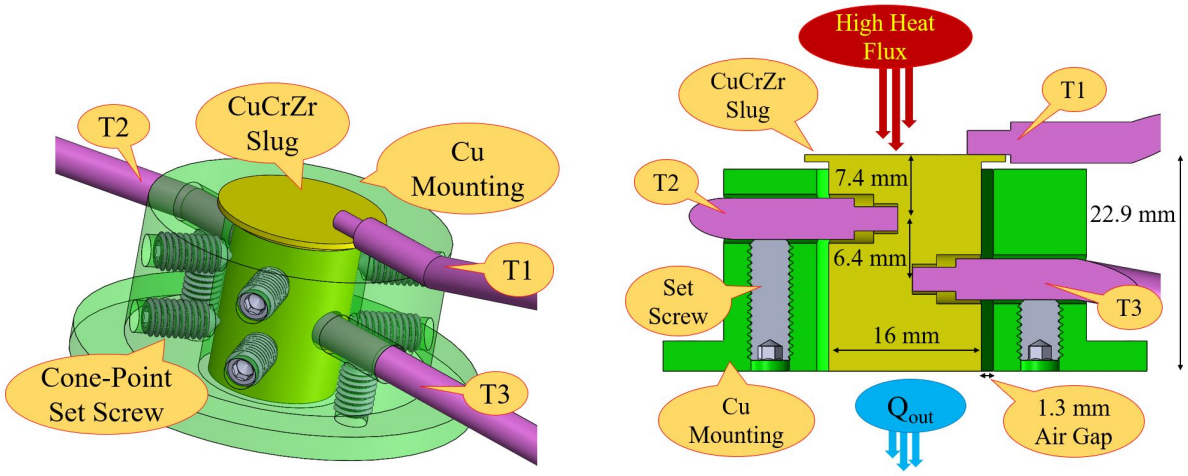

(a) (b)

Figure 53: (a) Heat Flux Sensor CAD showing CuCrZr slug and Cu mounting assembly and (b) Cross-section view showing the thermocouples T1, T2 and T3.

With the temperature measurements recorded at each distance from the arc-jet, the heat flux is computed using calorimetry. Two additional methods will be described next for heat flux determination, and these are: (1) The thick-wall technique [38], and (2) the inverse Method.

5.1.1 Calorimetry

In this method, the enthalpy of the slug is balanced, where the input heat flux at the surface minus any losses is balanced with the enthalpy change of the slug. The heat flux is computed using changes in the slug internal energy considering heat loss due to conduction at the bottom of the slug, where it is in contact with the cooling plate (Figure 52b). The heat loss (Q_{out}) can be calculated either by computing the heat removed by the cooling plate and water, or it can be calculated from the heat flux inside the slug, knowing the thermal conductivity and the temperature difference T_2-T_3 and assuming that the radial heat loss is negligible. This is given by:

$$Q = U + Q_{out} \tag{39}$$

$$q'' = \frac{Q}{A} = \frac{c\rho V \frac{d\bar{T}}{dt}}{A} + \frac{k}{L}(T_2 - T_3) \tag{40}$$

where Q is the heat supplied by the arc-jet, U is the slug internal energy, Q_{out} is the heat leaving the slug through its bottom face, q'' is the heat flux from the arc-jet, A is the slug area exposed to the heat flux (top face area), c is the slug specific heat, ρ is the slug density, V is the slug volume, $\bar{T}$ is the average slug temperature, t is time, k the slug thermal conductivity, L is the axial distance between Thermocouples T2 and T3, T_2 is the temperature of thermocouple T2, and T_3 the temperature of thermocouple T3.

Once the temperatures of the thermocouples T1, T2 and T3 are measured (Figure 53b), one can find an average temperature for the slug ($\bar{T}$), and then use numerical differentiation to compute $d\bar{T}/dt$ for the slug's internal energy in equation 40. The heat flux as a function of axial distance from the arc-jet is shown in Figure 54b. Here I computed and plotted the heat flux for both cycle 1 (beginning of each test, where the chamber is at 100 torr) and cycle 2 (towards the end of each test, where the chamber is at 400 torr). All tests were repeated twice at each distance to the arc-jet, and the results of measurements were used to determine the influence of the Ar gas back-pressure on the heat flux. However, for the other two data reduction methods (the thick-wall technique and the inverse method), I will compute the heat flux only using measurements from cycle 1 since most of the HEFTY tests are performed at this condition. It can be seen from Figure 54b that the computed heat flux

magnitudes are higher for cycle 1 (*blue plus signs*) as expected.

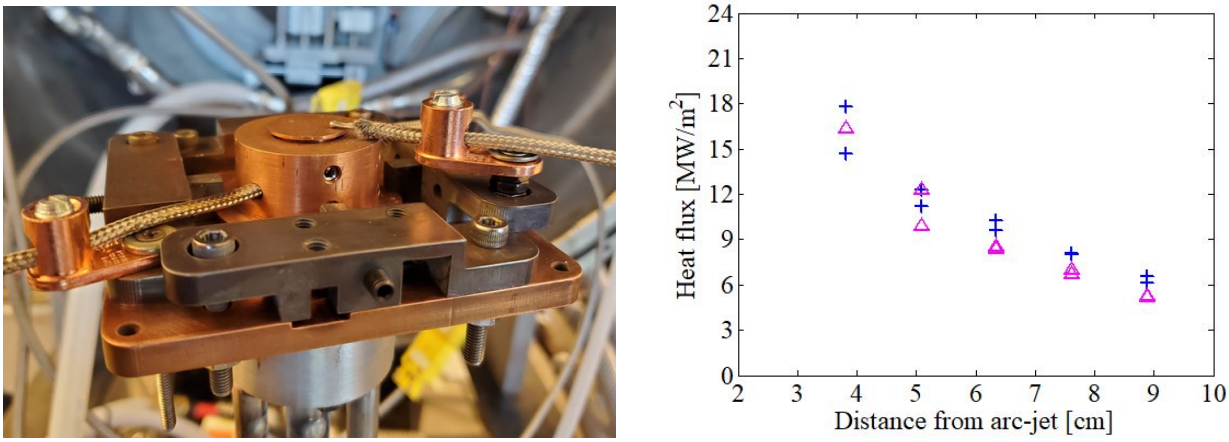

(a) (b)

Figure 54: (a) Fabricated heat flux sensor and its thermocouple setup. (b) Heat flux magnitude computed using the calorimetry method showing the difference between loading at cycle 1 and 2 (two tests was performed at each cycle). *Blue plus signs* are for cycle 1 and *magenta triangles* are for cycle 2 at each axial distance from arc-jet.

5.1.2 The inverse method

In this section, the CuCrZr slug in the sensor is modeled with the Finite Element Analysis method using the COMSOL multiphysics software. The model is in 3D, where the measured temperature at T3 (Figure 53b) is applied as time-dependent boundary condition representing the plane where T3 is located. An assumed heat flux is applied on the top surface of the slug, and the computed temperature at the location of T2 (Figure 53b) is compared with the measured value at this location. An iterative method is performed with various values of the heat flux till the calculated temperature is close to the measured one. An example of this process is presented in Figure 55a, where the applied boundary condition (measured temperature at T3) is shown in green and the calculated temperature at T2 (shown in blue) is compared with the measured values at T2 (shown in red). The heat flux magnitudes at each distance from the arc-jet are determined using this method, and are plotted in Figure 55b.

In these simulations, the applied heat flux is a function of rise time τ_1, the decay time τ_2, the parameter *b(x)* in the radial exponential decay function (calculated and discussed in

section 5.2.1), and the heating pulse period t_0, as shown in the heat flux profile in equation 50. $q_0(x)$ is the magnitude of heat flux at each distance x from arc-jet.

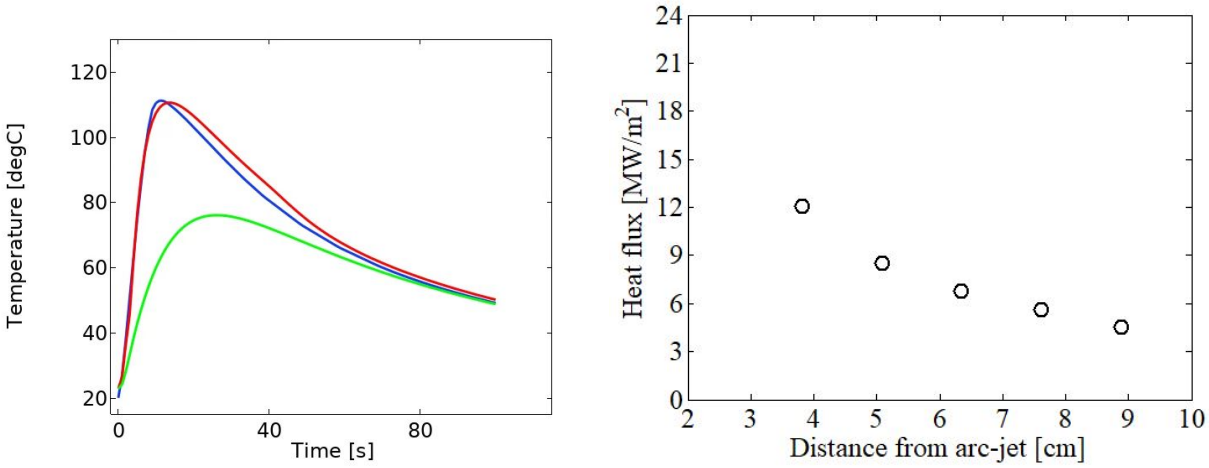

(a) (b)

Figure 55: (a) A comparison of T_2 profiles of the measured and calculated values at 7.62 cm from arc-jet using the inverse method (calculated temperature at T2 is shown in blue, measured temperature at T2 is shown in red and measured temperature at T3 is shown in green). (b) Computed heat flux magnitudes using the inverse method from a test performed at each distance from arc-jet.

5.1.3 Thick-wall technique (Semi-infinite model)

An analytical model is developed and reported in [38] for a thick-wall heat flux sensor using the transient heat conduction equation in a one-dimensional semi-infinite model. This technique can be used where the exposure time of the sensor is short enough that conductive heating does not reach the rear surface of the sensor and its temperature remains nearly constant. The idea is to rely on transient heat propagation in response to a suddenly applied heat flux on the front surface. The heat conduction equation and boundary conditions for the semi-infinite model are given by:

$$\frac{\partial T}{\partial t} = \frac{k}{\rho C_p}\frac{\partial^2 T}{\partial x^2} \tag{41}$$

$$T(0,t) = T_1(t) = T(t) \tag{42}$$

$$q_s''(t) = k\left(\frac{\partial T_1(t)}{\partial x}\right)_{x=0} = k\left(\frac{\partial T(t)}{\partial x}\right)_{x=0} \tag{43}$$

$$T(L,t) = T(\infty,t) = T_3 \tag{44}$$

Solution of equation 41 subject to the initial and boundary conditions gives the heat flux for a semi-infinite probe as following [38]:

$$q''(t) = \sqrt{\frac{\rho C_p k}{\pi}} \left(\frac{T(t)}{\sqrt{t}} + \frac{1}{2} \int_0^t \frac{T(t) - T(\tau)}{(t-\tau)^{\frac{3}{2}}} d\tau \right) \tag{45}$$

where T is the exposed face temperature (T_1 in Figure 53b), t is the time, x is the axial distance from slug exposed face and k, ρ and C_p are thermal conductivity, density and specific heat of the slug, respectively. Using the temperature measurements from T_1 located at the exposed face of the sensor, the heat flux is computed and plotted for the two tests performed at each distance from the arc-jet (Figure 56b). The semi-infinite model approximation is reasonable as long as the rear surface temperature does not significantly change. Hence, measurements are recorded only up to the time when the rear surface change is less than 1 °C.

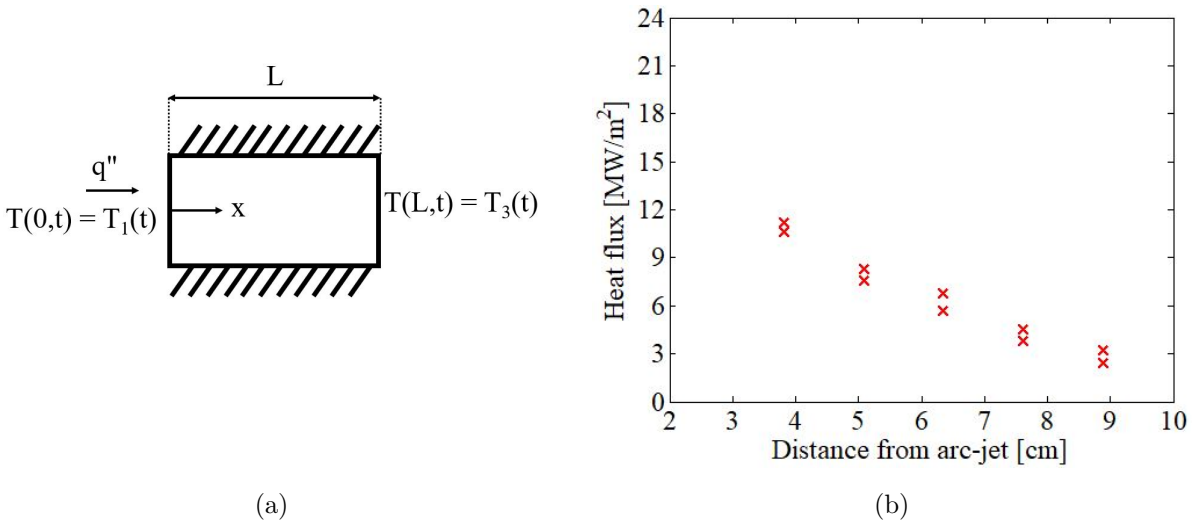

(a) (b)

Figure 56: (a) Semi-infinite model's boundary conditions. (b) Computed heat flux magnitude using the thick-wall technique from two tests performed with the heat flux sensor at each distance from the arc-jet.

The computed heat flux magnitudes from the calorimetry, inverse method, and the thick-wall technique are all plotted in Figure 57a for comparison. Also, the average heat flux at each distance from the arc-jet (average of computed heat flux from the calorimetry cycle 1, inverse method and thick-wall technique) are plotted in Figure 57b. The resulting heat flux versus axial distance curve can then be used as a reference heat flux for HEFTY. Equation

46 represents the green curve fit through the average heat flux magnitudes at each distance from arc-jet.

$$q_0(x) = 40.07 - 11.47x + 1.4x^2 - 0.063x^3 \tag{46}$$

where x (the distance to the arc-jet) is in cm and the heat flux $q_o(x)$ in MW/m^2.

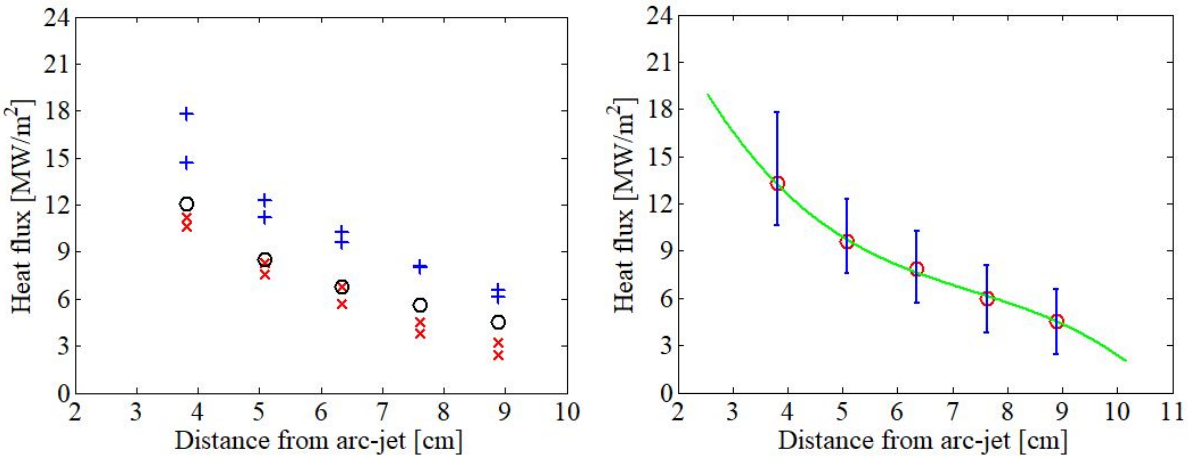

(a) (b)

Figure 57: (a) Heat flux magnitudes computed from the sensor temperature measurements at cycle 1 using the calorimetry method (*blue plus signs*), the inverse method (*black circles*), and the thick-wall technique (*red crosses*). (b) The average values (*red circles*) represent the heat flux magnitude at each distance from the arc-jet. Also, the curve fit through these average values is plotted in green.

5.2 Heat Flux Distribution

5.2.1 Radial Distribution

This section discuss the experimental setup to measure the radial heat flux distribution at each distance from arc-jet in the HEFTY chamber. In addition to measuring the magnitude of heat flux at plasma core at each distance from the plasma arc-jet, it is important to measure its radial distribution at each distance. The radial distribution of heat flux at each distance from the arc-jet has an exponential decay shape with a proposed function *f(r)* (equation 47) where r is radial distance from plasma core and b is a parameter that defines

the shape of the decay function at each distance from the arc-jet.

$$f(r) = \exp\left[-\frac{1}{2}(\frac{r}{b})^2\right] \tag{47}$$

The distribution function *f(r)* shown in Figure 60a has its maximum value at the center ($r = 0$) representing the maximum heat flux at the center of plasma (plasma core) and its value decays as r increases representing the decay in heat flux with increasing radial distance from plasma core. In HEFTY experiments the parameter b can be found by defining *f(r)* as T_2/T_1 where T_1 is the temperature of the sample at the center of plasma and T_2 is the temperature at a known distance from center. As the distance between T_1 and T_2 (r in equation 47) reduces ($r \to 0$) the value of *f(r)* gets closer to unity which means temperature of T_2 gets closer to T_1 as expected.

A series of experiments were performed using a 3.43 mm thick tungsten disk having two thermocouples installed on its back face (non-exposed face) one at the center (T1) and another one at 1.8 cm from the center (T2) as shown in Figure 58a. The thermocouples are spring loaded from the pockets made on the cooling plate to keep their contact with the W disk during experiment, and are mechanically fixed using set screws. The thermocouples used here are K-type and are not directly exposed to the plasma, which allows the radial heat flux distribution measurements all the way up to 2.54 cm from the plasma arc-jet. The perimeter of the W disk is covered with high temperature ceramic paste to prevent hot gases sneaking under the disk (Figure 58b). Having temperature measurements from these two thermocouples (T1 and T2) and knowing their radial distances (r=1.8 cm), the parameter b can be found for the exponential decay function (equation 47) at each distance from the arc-jet as follows:

$$b = \sqrt{\frac{r^2}{-2Ln(f(r))}} \tag{48}$$

where $f(r) = T2/T1$.

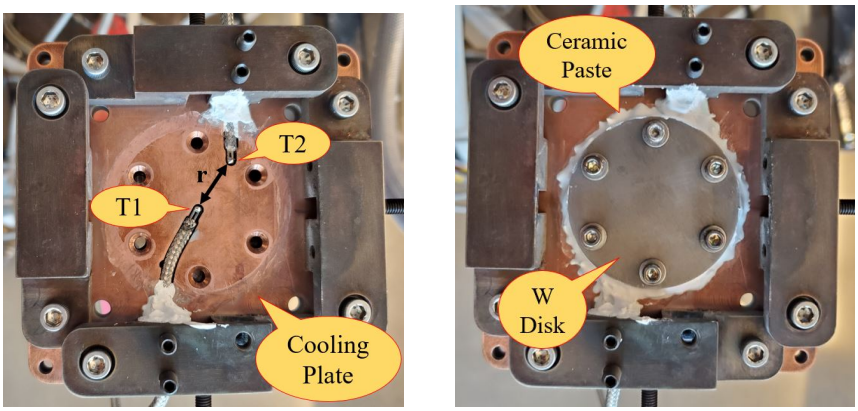

(a) (b)

Figure 58: Experimental setup to measure the radial heat flux distribution at each distance from the plasma arc-jet showing (a) thermocouple placement underneath the W disk and (b) ceramic paste on the W disk perimeter preventing hot gases sneaking under the disk.

Three tests are performed at each distance form the arc-jet and the calculated b values at each distance form arc-jet are plotted in Figure 59a. The average b at each distance from the arc-jet is plotted in Figure 59b, including its curve fit as given by:

$$b(x) = 1.36 - 0.094x + 0.0366x^2 - 0.00125x^3 \tag{49}$$

where x (the distance to the arc-jet) and $b(x)$ are both in cm. Having b at each distance x from arc-jet (equation 49) the radial distribution of heat flux at each distance from arc-jet is plotted in Figure 60b using equation 47. It can be seen that as getting further from arc-jet the heat spreads more on the sample compare to the focused central heating at 2.5 cm from arc-jet.

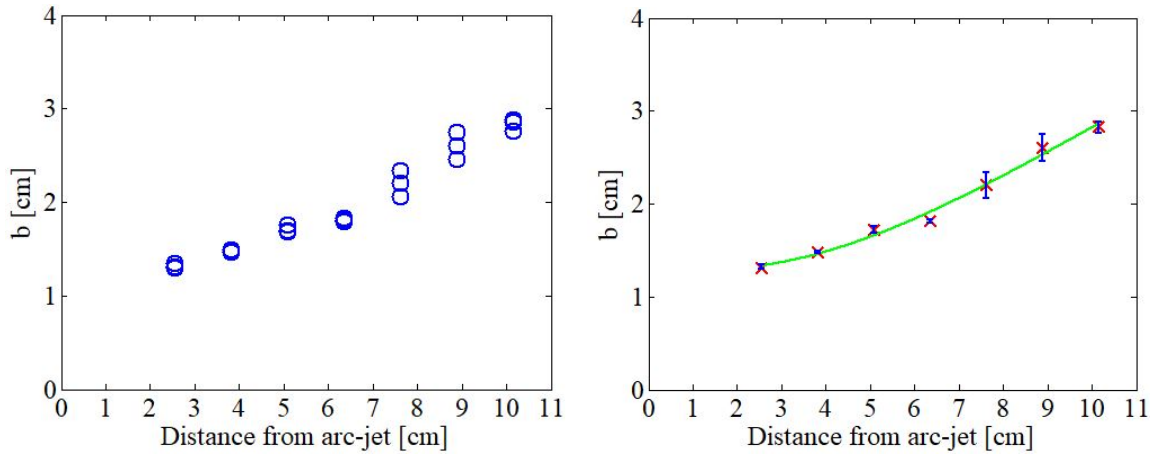

(a) (b)

Figure 59: (a) Calculated values for parameter b in radial exponential decay function *f(r)* at each distance from the arc-jet (three tests at each distance) and (b) their average value at each distance (*red cross signs*) and the corresponding curve fit (green curve).

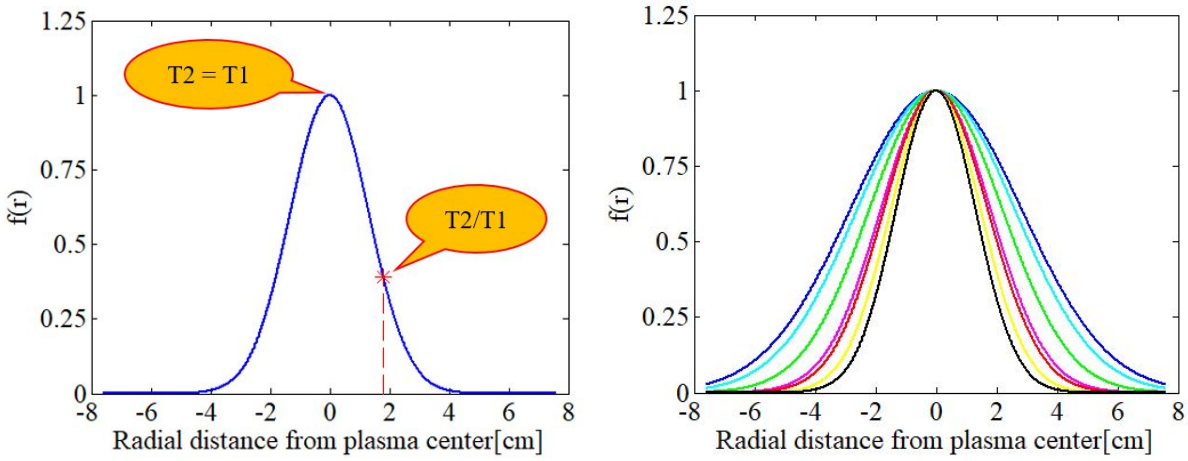

(a) (b)

Figure 60: (a) Shape of the proposed exponential decay function for radial heat flux distribution and the data point at r=1.8 cm used in defining parameter b for the decay function (equation 47) having T_2/T_1 from experimental measurements. (b) Plotted radial heat flux distribution at each distance from arc-jet as an exponential decay function. The radial heat flux distribution at 2.5 cm from arc-jet is plotted in black, 3.8 cm in yellow, 5.1 cm in red, 6.4 cm in magenta, 7.6 cm in green, 8.9 cm in light blue and 10.2 cm in dark blue.

5.2.2 Three-dimensional Heat Flux Profile

This section describes the development of an equation for the HEFTY arc-jet heat flux profile considering all the parameters discussed in the previous sections ($q_0(x)$ and $b(x)$). The developed equation can be used in our Finite Element Analysis (FEA) as an applied thermal load to perform heat transfer and structural analysis on samples tested in HEFTY. In order to represent the heat flux for FE transient structural analysis, a space-time heat flux profile is established utilizing the heat flux measurements. The heat flux profile in HEFTY is described by a set of parameters, as follows:

$$\begin{aligned} q(r,t,x) =& q_0(x) \exp\left(\frac{-r^2}{2b^2(x)}\right) \{(1-U(t-t_0))\left(1-e^{-t/\tau_1}\right) + \\ & \left(1-e^{-t_0/\tau_1}\right) U(t-t_0) e^{-(t-t_0)/\tau_2}\} \end{aligned} \tag{50}$$

Here, x is the distance between the exit plane of the arc-jet and the sample exposed surface (Figure 52a), r is the radial distance from the plasma (sample) center (Figure 52a), t is time, $q_0(x)$ is the magnitude of heat flux measured by the heat flux sensor as a function of the distance x from arc-jet (equation 46), $b(x)$ is the parameter used in exponential decay function for radial heat flux distribution (equation 49) describing the radial decay of heat from the plasma center, U is the standard unit step function, τ_1 is the rise time of the heat flux after the arc-jet has been turned on, τ_2 is the decay time of the heat flux due to hot gases after the arc-jet has been turned off, and t_0 is the heating pulse period.

Heat flux distribution at each distance form arc-jet is plotted in Figure 61b considering its magnitude at the plasma core (equation 46) and the radial distribution (equation 47) at each distance from arc-jet. Also, heat flux profile at the center of a sample ($r = 0$) located at 2.5 cm from the arc-jet ($x = 2.5$) is plotted as a function of time using developed equation 50 ($x = 2.5$, $r = 0$, $t_0 = 6$ s, $\tau_1 = 0.6$ s, $\tau_2 = 1.29$ s, and $b = 15.3$ mm) as shown in Figure 61a.

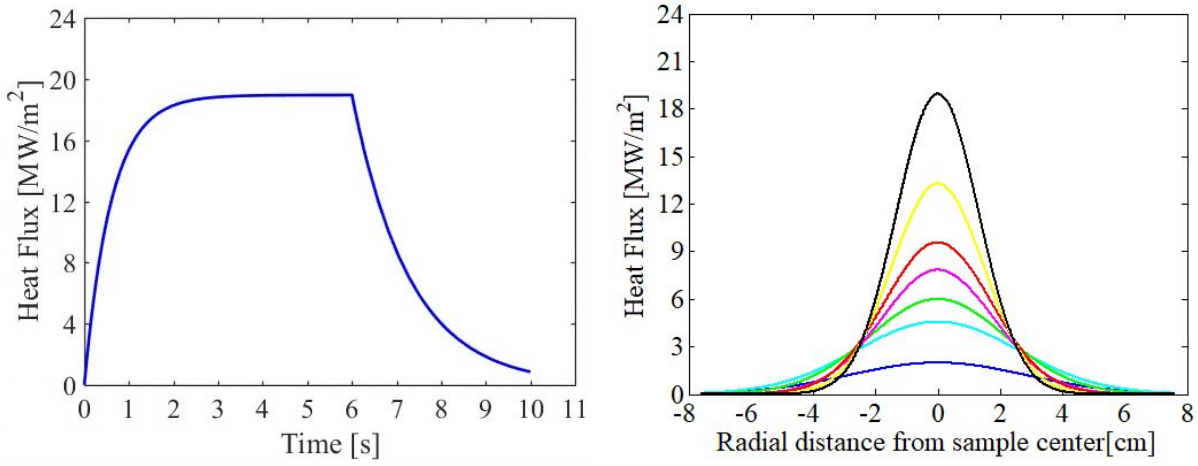

(a) (b)

Figure 61: (a) HEFTY arc-jet heat flux profile during one cycle (6s arc-jet ON-time and 4s OFF-time) at the center of the exposed face of the sample located 2.5 cm from the plasma arc-jet. (b) HEFTY arc-jet heat flux distribution on the sample's exposed face as a function of distance from the arc-jet. The heat flux distribution at 2.5 cm from arc-jet is plotted in black, 3.8 cm in yellow, 5.1 cm in red, 6.4 cm in magenta, 7.6 cm in green, 8.9 cm in light blue and 10.2 cm in dark blue.

CHAPTER 6

Cyclic Heating Effects on Surface Damage of Micro-Porous Tungsten

6.1 Introduction

Plasma-Facing Components (PFCs), such as the divertor of a Tokamak fusion reactor, are expected to receive a high heat flux on the order of 10 MW/m^2 [23, 39] during on- and off-operational cycles. In addition, occasional fast plasma excursions depositing up to 1 GW of power in 1-10 ms are also expected. Tungsten is the leading solid material for divertor applications, with a narrow temperature window of operation (roughly 300-1300 °C), limited by the DBTT at lower temperatures and recrystallization at higher temperatures. Outside this range, its fracture toughness drops, and it develops massive through-the-thickness cracks as a result of residual tensile stresses developing during transient plasma operations. One approach to mitigate massive cracking (and hence failure) of W is to use a micro-porous form with an interconnected 3-D network of ligaments (foam) [40]. As the surface of such structure expands and contracts, ligaments can rotate at their interconnections as hinges, and bend rather than crack in between. Thus, massive cracks can be avoided, and instead, a benign network of micro-cracks can accommodate the expansion/contraction strain generated by plasma transients. The basic scientific phenomenon that we are addressing here is the thermal stress resilience of a new form of tungsten, and that is the open-cell cellular structure. This is a new "meta-material" that possesses the ability to deform substantially because of its flexible geometry.

The thermal resilience of foam stems from its porous nature and geometry where flexible ligaments provide enough room for free thermal expansion. The brittle nature of solid

tungsten, specially below its DBTT, is the source of crack formation due to residual stresses or thermal shock. When solid tungsten goes under extreme and sudden local thermal loading, the material surrounding the loading zone constrains the loading area's free thermal expansion. This results in the generation of residual stresses in the loaded area which will introduce tensile stress upon cool-down causing crack formation and propagation. However, under the same loading conditions, tungsten foam does not develop extreme residual stresses because the loaded area has enough porosity to accommodate thermal expansion through ligament rotation without experiencing constraints from the surrounding material.

The two key parameters that control the thermomechanical response of micro-porous structures are the foam density (or volume fraction) and the mean cell size expressed in Pores Per Inch (PPI). These parameters have direct influence on the effective properties, such as thermal conductivity, elastic modulus, and strength of the foam. We present here experimental results of W foam samples under three different loading conditions designed to investigate the influence of high heat-flux (generated by an atmospheric plasma jet) on the thermomechanical resilience of micro-porous tungsten foam. The foam samples were fabricated at Ultramet, Inc., using the Chemical Vapor Deposition (CVD) process and bonded to tungsten substrates for easier assembly. More details about the CVD process can be found in our previous publication [41]. We include here testing of two tungsten foams (45 PPI, 25% density shown in Figure 64a and 45 PPI, 54% density shown in Figure 64c) and nine tungsten foams (65-80 PPI, 23-43 % density) that have nano-porous features (fuzz) due to their prior exposure to the low-energy helium plasma of the UCSD PISCES device prior to our tests. The fuzz formation experiments are summarized in another work from our group [42]. In section 6.2, we outline our test procedures in HEFTY at UCLA. In section 7.5, we present the results of testing W foams exposed to three different types of plasma heating/cooling cycles. Finally, a summary and conclusions are given in section 6.4.

6.2 Experimental Conditions

Samples have been exposed to the plasma arc-jet from one side and cooled by a water-jet connected to a CuCrZr cooling plate in contact with the back side of the solid W substrate, as shown in Figure 62. A variety of molybdenum and tungsten apertures with 3.2 mm and 6.4 mm exposure radius were used to confine the heat flux to a desired area at the sample center, introducing radial and axial temperature gradients. The solid W substrate is constrained using spring loaded clamps allowing radial thermal expansion of the solid substrate and the foam itself is not in touch with these clamps (Figure 62b). Three thermocouples were attached to the tungsten foam mechanically using set screws (Figure 62b) and the accuracy of attachments was inspected before each test by running the water jet connected to the cooling plate (Figure 62) and checking the temperature of each thermocouple against the water temperature in the reservoir. Thermocouple 1 (T1) measures the temperate at the exposed face center, thermocouple 2 (T2) at the exposed face edge, and thermocouple 3 (T3) at the W-substrate cooling face. In our experiments, thermal cycling was implemented by controlling the on- and off-times of the high-enthalpy arc-jet plasma. The arc-jet is part of a control system driven by a LabVIEW program. The electric current supplied to the gun is switched on- and off- following control instructions of the LabVIEW program. The samples are assembled on a fixture that can be moved remotely with respect to the arc-jet to change the applied heat flux.

Samples were tested under three different thermal cycling categories: A, B and C. The idea is to investigate the effects of different thermal loading scenarios on the damage and fracture of tungsten foams. In category A, the sample surface temperature exceeds the re-crystallization temperature (1300 °C) during plasma heating ($\approx$ 7 MW/m^2 for 5 seconds) and cools down for 10 seconds to temperatures above the DBTT (300 °C). This thermal loading is repeated for 20 cycles and allows us to investigate the effects of cyclic plasma heating above the tungsten recrystallization temperature. Typical temperature measurements from the first 2 cycles of this category is shown in Figure 63a. In some tests performed in category A, the cooling time was reduced from 10 seconds to 5 seconds so as to increase the foam

exposed face temperature to ≈ 2000°C during each cycle to study the effects of higher temperatures. Category B is designed to result in the sample surface temperature to be above the recrystallization temperature during heat-up (≈ 7 MW/m^2 for 5 seconds) and below the DBTT during cool-down (120 seconds) between cycles. This category includes 10 cycles, and Figure 63b shows the first two. This category is designed to investigate the effects of a wider temperature difference encompassing both critical temperatures (recrystallization and DBTT). Category C has a higher power density (≈ 12 MW/m^2), but is applied for a shorter time (≈ 1.5 seconds), reaching a rapid surface temperature rise of 900 °C/s, thus allowing thermal shock investigations. In this category, the exposed face temperature exceeds the recrystallization temperature during thermal loading and reduces below the DBTT during cool-down (120 seconds) between each cycle. This category includes 10 cycles, and its first two cycles are shown in Figure 63c.

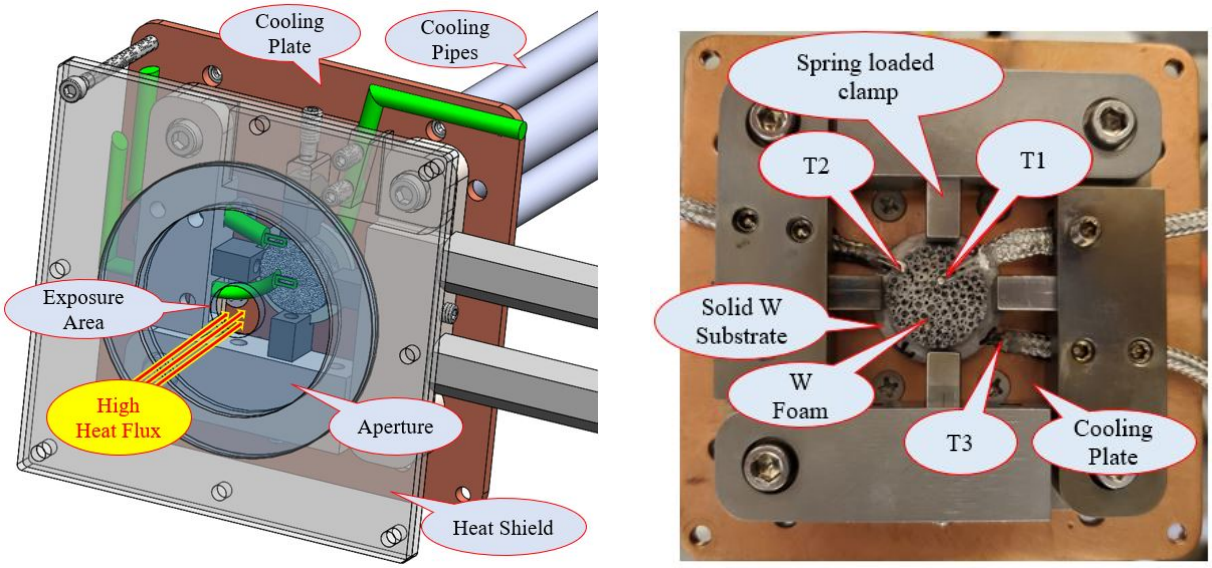

(a) (b)

Figure 62: The apparatus designed to test materials under cyclic thermal loading and thermal shock conditions. (a) Heat shield and aperture confining direct plasma exposure to a desired radius on the center of sample to study local loading and material self-constraint effects. (b) Thermocouples setup on sample.

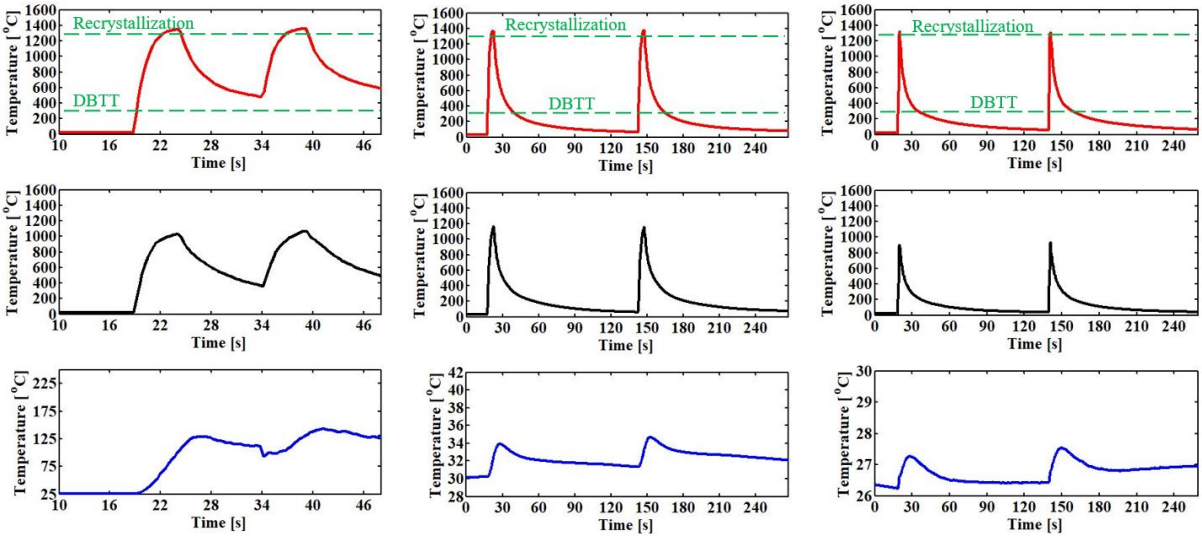

Figure 63: Temperature measurements for the first two cycles in each test category. (a) Testing category A, (b) testing category B and (c) testing category C. Red curves show the temperature of the tungsten foam at the plasma-exposed face at the loading zone center (T1 shown in Figure 62b), black curves show the temperature of the exposed face at the sample edge (T2 shown in Figure 62b) and blue curves show the temperature of the substrate cooling face close to the sample edge (T3 shown in Figure 62b).

6.3 Test Results

Experiments were performed on eleven tungsten foams having 45-80 PPI and 23-54 % densities. A circular region at the center of each sample was directly exposed to the arc-jet plasma utilizing 3.2 and 6.4 radius apertures (Figure 62a). Also, several tests were performed with no aperture to raise the foam surface temperature uniformly and to increase the overall thermal strain. Each sample is inspected carefully under the scanning electron microscope (SEM) for any possible pre-exposure damage, and pre-exposure images are taken. Figures 64a, 64c and 65a show typical images with no damage before testing. After each test, the samples are again inspected carefully with the SEM to investigate the effects of thermal loading. Typical images showing microcracks are shown in Figures 64b, 64d and 65c. From these observations, we conclude that these micro-cracks result from arc-jet plasma exposures and are not present in the pre-exposed samples.

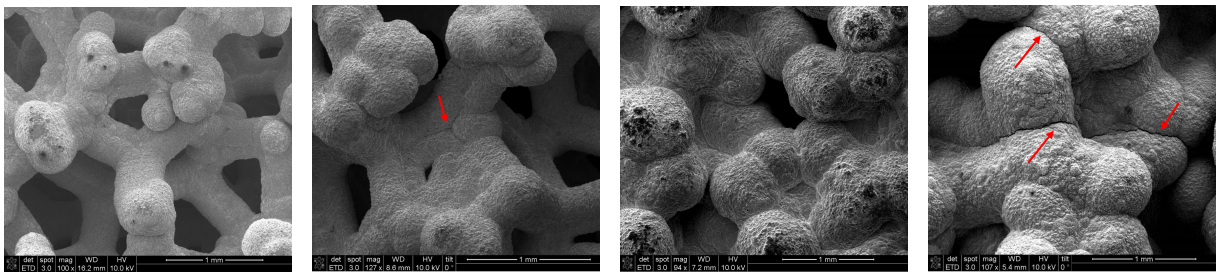

(a) (b) (c) (d)

Figure 64: (a) A typical pre-exposure SEM image of the 45 PPI, 25 % density foam showing no damage and (b) a typical post-exposure SEM image of the 45 PPI, 25% density foam showing minimal damage. (c) A typical pre-exposure SEM image of the 45 PPI, 54 % density foam showing no damage and (d) a typical post-exposure SEM image of the 45 PPI, 54% density foam showing several micro-cracks on foam ligaments (cracks are shown with red arrows). Both 45 PPI, 25 % and 45 PPI, 54% foams were tested utilizing a 3.2 mm aperture under category A with 10 seconds cool-down between each cycle.

Post exposure observations on the foam samples revealed three types of damage. The first is manifest as a network of micro-cracks observed at ligament triple junctions. An example is shown in the SEM image in Figures 64b and 64d. The second includes localized melting and re-solidification in small regions of $< 500\mu m$. Also, post-exposure SEM images from the nine samples with nano-porous features (fuzz) show that these nano-foam features have undergone melting and solidification due to their low effective conductivity, forming a "shell" around the ligaments (Figure 66). In addition, localized melting was mostly observed on the highest exposed ligament surfaces, along with sublimation of pyramid-like textures. The third type of damage includes ligament separation, as shown in Figures 65b and 65c. Few ligaments were found to be completely separated, while no ligaments were found to be fractured in between triple junctions.

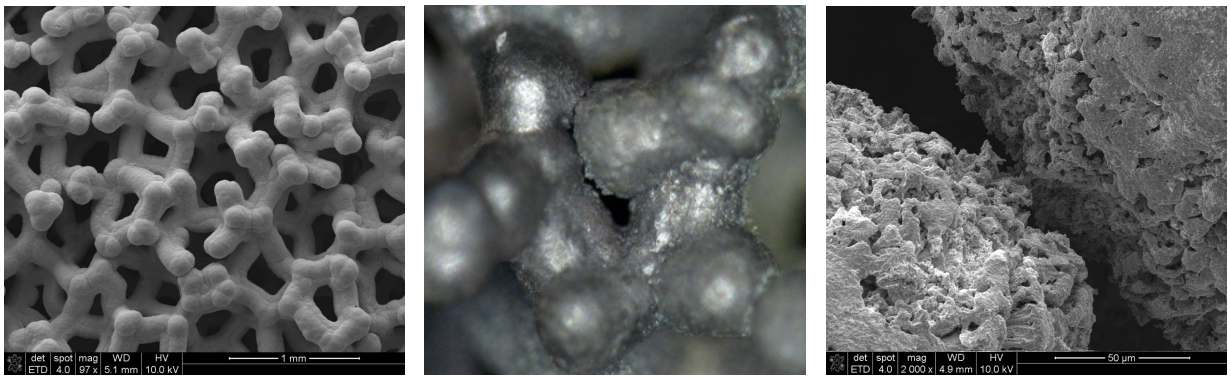

(a) (b) (c)

Figure 65: (a) A typical pre-exposure image of 80 PPI, 23 % density foam showing no damage, (b) optical microscopy image of the foam showing a separated ligaments and (c) SEM image of the foam showing two ligaments almost completely separated. This foam was tested with no aperture to expose the entire foam to direct plasma under category A with 5 seconds cool-down between each cycle.

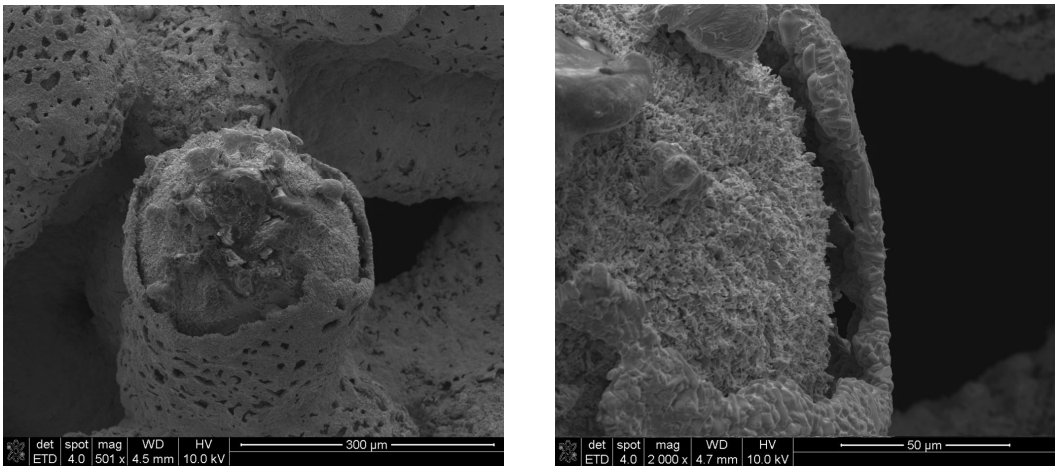

(a) (b)

Figure 66: (a) Post exposure SEM image showing solidification of nano-porous features (fuzz) and shell formation around the ligaments and (b) higher magnification image showing a 10 μm gap between ligament core and solidified shell.

We noticed that cracks mostly occurred in two loading conditions. First, category A with the 3.2 mm aperture and 10s cool-down time. Foam samples tested under this condition showed larger radial temperature gradient. Cracks were observed closer to the edge of the foams (outside direct exposure area). These cracks are shown in Figures 64b and 64d. Our interpretation is that while thermal strains were accommodated in the ductile hot zone of

the samples (center of the foams), micro-cracks formed in the cooler regions, where tungsten ductility is low. The second condition is category A with no aperture to elevate the entire exposed face temperature uniformly to $\approx$ 2000 °C by reducing the cool-down time to 5 seconds between cycles. This extreme thermal loading resulted in large thermal strains and caused some ligament separation, as shown in Figures 65b and 65c. The foam density was found to be another important factor in controlling W foam fracture. Foams with very high density (54%, Figure 64c) act more like a solid and don't allow free thermal expansion resulting in micro-cracks under thermal loading. Low density foams (23%, Figure 64a) do not have enough stiffness and show less resistance to thermal loading. However, we found that foams with 43% density have the best combination of stiffness and flexibility to withstand the extreme thermal loading with minimal or no damage, as compared to foams with 23% and 54% density. It is important to note that cracks in the foams tested in this work were distributed as a network, and that there were no major cracks through the material as observed in solid tungsten [41, 1]. More quantitative and theoretical analyses is included in section 7 comparing failure modes in solid tungsten and tungsten foam under thermal cyclic loading.

Energy Dispersive x-ray Spectroscopy (EDS) was used to monitor changes in surface chemistry post-exposure, in particular, the amount of oxidation occurring on the W surface. Tungsten oxide was found in a handful of forms (WO_3, $WO_{2.9}$, $WO_{2.72}$, WO_2) which is typically undesirable due to its brittle nature. Various forms of tungsten oxide rapidly form at elevated temperatures (>600°C) in oxygen-rich environments, and can vary from atomic layer depth to micron-sized particulates. Another indication of oxide formation is the visible "bluing" of the sample surface after some of the exposures. The blue color often accompanies $WO_{2.9}$ and on occasion $WO_{2.72}$, depending on the structure of the oxide layer.

6.4 Summary and Conclusions

Solid W armor for PFC applications is known to have some undesirable features. First, its temperature cannot exceed ≈1300°C because of primary re-crystallization affecting its

low-temperature ductility. Second, if the temperature drops below 300°C, it is prone to massive cracking because of the low fracture toughness. And third, if a crack is initiated at the surface exposed to a severe plasma transient, it grows uncontrollably all the way down to the interface with cooling channels rendering the component inoperable. Tungsten foam, on the other hand, can alleviate some of these deleterious effects due to the geometric flexibility of its 3-D architecture of interconnected ligaments. The W foam samples tested here showed significant resistance to thermomechanical damage. Three different thermal loading conditions (category A, B and C) were designed to investigate the resilience of this newly developed material to cyclic loading under ≈ 7 MW/m^2 and ≈ 12 MW/m^2 heat fluxes with varying heating and cooling times to reach to desired temperature profiles designed for each category. In category C (≈ 12 MW/m^2), a rapid temperature rise was recorded at 900 $^\circ C$/s producing thermal shock conditions. Foams tested under this condition showed minimal or no damage. Foams tested under category A (≈ 7 MW/m^2) showed the most damage and micro-cracking due to large temperature gradient in the radial direction introduced by the smaller aperture (3.2 mm exposure radius). Also, in another group of tests performed in Category A where surface temperature was uniformly raised to ≈ 2000 °C, benign (does not lead to massive failure) surface damage and ligament separation were observed. Foams with 43% density showed the most resilient to thermal loading.

We conclude here that the majority of foam samples survived severe cyclic plasma thermal loading, showing no significant damage. Micro-cracks were observed generally at ligament triple junctions (Figures 64b and 64d). Other features of observed thermomechanical damage includes: ligament separation, needle-like tungsten oxide formation, and substantial changes in surface texture. Large-scale cracks, typical of what is observed in solid W exposed to similar conditions, were not observed in any of the tested foam samples. The presence of micro-cracks in foam samples as compared to massive cracks in solid W samples is indicative of thermomechanical resilience. The accommodation of many micro-cracks in ligaments is possible without adverse effects on component integrity, as compared to massive through-the-thickness cracks [41, 1] that can lead to rupture and coolant ingress into the core plasma. Temperature measurements have shown that W foam can provide a degree of heat shielding

for the substrate material due to a lower effective thermal conductivity. Thus, a plasma-facing component may include a top non-structural layer (armor) of W foam, bonded to a structural solid W substrate.

CHAPTER 7

Thermo-Fracture and Thermal Shock of Open-Cell Tungsten Foam

7.1 Introduction

Plasma facing components (PFCs), such as divertor modules in Tokamak-type fusion reactors and the Leading Edges (LE) of hypersonic aircraft, must to be designed to perform reliably under normal and transient operating conditions. The most challenging environment for PFCs is the extreme heat flux incident on such components, reaching up to 10 MW/m^2 [23] during steady-state operation. More severe conditions are also expected during thermal transients generated by plasma instabilities leading to heat flux levels of hundreds of MW/m^2 up to GW/m^2 for brief periods and at various frequencies. Tungsten has the highest melting point of any element in the periodic table (3422 °C). Its low thermal expansion and high melting point and tensile strength originate from strong covalent bonds formed between tungsten atoms by the 5d electrons. For these reasons, it has been selected as the material of choice for PFCs. However, solid W tends to be brittle at low temperatures (below the Ductile-Brittle-Transition-Temperature , DBTT, of 200-400 °C). *Through-thickness* cracks develop as a result of thermal stresses, often associated with rapid temperature transients. The exact origin of such "component-failure" type cracks is not always clear, although such cracks are often described to result from *thermal shock*. In a numerical study of the phenomenon of catastrophic cracking of W mono-blocks employed in the divertor design of the International Thermonuclear Experimental Reactor (ITER), [43] showed that W mono-block armor suffered from catastrophic cracking due to thermal fatigue, when the applied high-heat-flux load approaches 20 MW/m^2. Crack initiation and growth were shown to result

from plastic strain accumulation first, followed by brittle fracture upon cool-down.

Traditionally, thermal shock resistance of a material is measured by the maximum temperature difference that a sample can tolerate when it is suddenly brought to a higher (or lower temperature) before it completely fractures. Sample heating is thus transient, and can be from one or all surfaces. The basic reason for fracture under these idealized test conditions is the self-constraint of the material as steep temperature (and expansion) gradients develop during the transient heating or cooling stage. However, potential thermal fracture of PFCs can result from a variety of reasons related to the geometry (self-constraint), the boundary conditions, residual stresses due to plastic deformation, and temperature (and microstructure) dependent material properties. Since it is unclear whether a component fractures in a temperature transient from steep temperature gradients resulting from poor heat diffusion, or due to external constraints on free expansion/contraction, it is prudent to investigate the conditions for "thermo-fracture" of solid and porous (foam) tungsten during heating and cooling plasma cycles.

Not all thermal shock damage is catastrophic, leading to "through-thickness" cracks that are associated with component loss of function. If energy deposition is very fast and intense, most fracture damage will be close to the surface in a "network" of micro-cracks. Such damage is not immediately catastrophic, and may be useful in accommodating surface expansion/contraction strains from cycle-to-cycle. Eventual component failure may be delayed to many operational cycles if such cracking damage inhibits catastrophic cracks that propagate with every cycle. Stress-relieved and recrystallized W were exposed to 100 (Edge Localized Mode) ELM-like thermal shock events in the electron beam facility JUDITH-1 [44]. In this study, it was found that surface roughening due to plastic deformation is more pronounced in recrystallized W, and that crack propagation is inter-granular. In contrast to the "slow" transients at a heat flux of 20 MW/m^2 which result in catastrophic cracks, [44] performed experiments on W at the JUDITH facility at a power level of 0.16-1.27 GW/m^2, for a short duration of only 1 ms. The study showed that if the W base temperature was lower than 100 °C, a crack pattern on the surface was observed at power densities above 200 MW/m^2. Unlike the "catastrophic crack" observed in slow transients at lower heat flux

levels (20 MW/m^2), thermal shock damage was observed to be distributed in a thin surface layer as a network of average crack length in the range 400-500 μm, and depth of 200-250 μm [44]. Recrystallized W samples showed a lower cracking damage threshold because of the lower yield strength leading to more extensive plastic deformation upon heating and subsequent residual stresses during the cooling phase. A more focused study on the effects of recrystallization by [45] confirmed a decrease in the thermal shock resistance of W, and that the damage threshold was at around 0.22 GW/m^2. The effects of alloying with tantalum on the thermal shock behavior was also studied in the JUDITH e-beam facility . Tantalum alloying was found to shift the damage threshold power from 0.2 to 0.4 GW/m^2 and the base brittle temperature of W from $\approx$ 200 °C to below 100 °C for Ta content of 5%. However, the crack network pattern remained the same, although alloying with 5% Ta reduced these values by $\approx$ 50% [46].

Open-cell W foams have been proposed as armor materials for PFCs because of their potential in absorbing thermal shock without the catastrophic failure mode that is often observed in solid W in response to slow plasma heating transients [47, 48, 49, 50]. This possibility is a consequence of the flexible geometric structure of the open-cell foam as a 3-dimensional truss. When the open-cell foam is stretched or compressed beyond its elastic regime, the applied external strain is absorbed mainly at ligament junctions in the form of "plastic hinge" rotations [51, 52]. Thus, large external strains (including thermal strains) can be accommodated by a combination of ligament rotation and ligament bending. However, the bending strain in ligaments is small, and estimated to be about one order of magnitude smaller than externally applied strain [52]. The mechanical behavior of metal foams has been under experimental and theoretical investigations [52, 53, 54, 55, 56] because of the prospect of tailoring their properties by changing geometric parameters that describe the foam. Although cellular metallic foams have been around for some time, most experimental and theoretical investigations focused mainly on their mechanical properties alone (e.g. deformation characteristics [54]), or fluid or thermal properties alone [57, 58]. While the influence of mechanical shock waves on the response of metallic foams has been studied [59], the influence of thermal shock loading on the mechanical behavior of metallic foams has not

been extensively considered.

The objective of the present investigation is to determine the influence of plasma heating/cooling cycles on the thermomechanical response of tungsten. To achieve this goal, we developed models for the thermomechanical behavior of both solid and porous W samples and performed an extensive set of experiments to explore the following four questions:

1. What is the influence of external versus self-constraint on W fracture?

2. Is there an effect of sample geometry on the deformation mode (bending versus in-plane), and hence on fracture?

3. Does the micro-truss-like geometry of the porous W-foam allow it to accommodate thermal strain without fracture?

4. What is the difference between thermal shock of W foam at extreme power (GW/m^2)/ short duration (ms) and high-power (MW/m^2)/ long duration (seconds)?

We first present the W foam fabrication process in section 7.2. A description of test procedures and conditions for the plasma arc-jet in the UCLA HEFTY facility is given in section 7.3. A computational model for the effects of thermal shock loading on the deformation and stress state of solid and tungsten foam is given in section 7.4. We show the influence of sample geometry and constraints by Finite Element (FE) simulations. A summary of the effective properties of W foam samples is also given. Experimental results are then presented, where we first show the effects of low-energy helium plasma on W foam in subsection 7.5.1, followed by the effects of high heat flux on W recrystallization and thin disk failure in subsection 7.5.2.1, the results of material self-constraint in subsection 7.5.2.2, the influence of fully constrained samples on grain growth and crack initiation in subsection 7.5.2.3, and a direct comparison between W foam and solid W disk behavior under the same thermal loading in subsection 7.5.2.4. Experimental results performed at the PSI-2 Laser facility at the Forschungszentrum in Jülich, Germany, are presented in subsection 7.5.3. Finally, we give a summary of the results and conclusions in section 7.6.

7.2 Fabrication

Open-cell tungsten foam is produced by Chemical Vapor Deposition (CVD). It is an extremely versatile and relatively inexpensive method of forming structures that are difficult to create by conventional powder metallurgy and machining, as exemplified by tungsten. A precursor vapor containing a tungsten compound is flowed over a heated substrate, where it reacts to deposit W with reaction byproducts then exhausted from the system. The benefits of CVD include the ability to produce deposits of controlled density, thickness, orientation, and composition. Purity levels in excess of 99.99% are achievable. In addition, the CVD process exhibits the greatest throwing power, or ability to uniformly deposit materials onto/into intricately shaped or textured substrates, thus allowing fabrication of near-net shape parts with geometries that cannot be produced through conventional processing and machining. Metal deposits are formed on the substrate at the molecular level. The typical deposition rate for W is $\approx$ 0.2-0.3 mm/hr (it takes 10-12 hours to fabricate a sample, 3 mm thick). CVD allows the ability to control grain size and orientation for optimizing W behavior for specific applications.

CVD W is deposited at just 550 °C through the hydrogen reduction of its hexafluoride under vacuum, flowed over a heated substrate in accordance with the following chemical reaction: $WF_6 + 3H_2 \Longrightarrow W + 6HF$. Ultramet Inc. has developed the technology to fabricate open-cell refractory metal and ceramic foams starting from commercially available and inexpensive polyurethane foam. The polyurethane foam, which has pore densities ranging from 3 to 100 pores per linear inch (PPI), is infiltrated with a furfural (C_4H_3OCHO)-phenolic (C_6H_6O) resin, then pyrolyzed at 1100 °C to yield a vitreous carbon foam that precisely replicates the reticulated structure of the original polyurethane foam. The carbon foam is then used as a skeleton for the fabrication of W metal foam. Carbon foam can be easily machined or pressed into or over complex curved shapes, and can first be converted into a more desirable material, such as TaC, prior to infiltration, or removed via oxidation to produce hollow ligaments. The foam skeleton is then infiltrated with W until the target density is achieved. A thin CVD interlayer (proprietary) is first deposited to prevent reaction

between tungsten and the carbon foam at elevated temperatures. This process yields porous W structures with far superior thermal and mechanical stress tolerance due to the ability of individual ligaments to distort and relieve stress.

7.3 Experimental Apparatuses

An arc-jet plasma is utilized as the high heat flux source with maximum flexibility in testing solid and foam samples under a variety of boundary conditions in the HEFTY. During our experiments, the sample is assembled on a CuCrZr cooling plate from the bottom face while the top face of the sample is directly exposed to the high heat flux Ar plasma arc-jet. The cooling plate is continuously cooled by a room temperature water jet. This setup can introduce a steep axial temperature gradient through the sample thickness. Also, the arc-jet plasma power in HEFTY has a radial exponential decay shape with a higher intensity at the sample center. This feature is exploited in the introduction of radial temperature gradients in tested samples, allowing studies of the influence of self-constraints, where the outer cooler regions constrain the middle region of the sample. We have also designed a variety of molybdenum and tungsten apertures to confine arc-jet heating to a desired spot at the sample center (3.2 & 6.4 mm radius). The resulting arc-jet heat-flux radial distribution can be tailored to control the radial temperature gradient. The maximum applied heat flux and the radial distribution can be controlled by varying the sample's distance from plasma arc-jet. This is accomplished by a specially designed fixture that can be moved remotely with respect to the arc-jet from our HEFTY control computer program. More details about HEFTY test setup and heat flux calibration can be found in section 4.1 and chapter 5 respectively.

Solid W disks were tested under two different boundary conditions, as shown in Figures 67a and 67b. The fully constrained setup (Figure 67b) is designed to test the resilience of solid W under high heat flux in fully constrained assemblies. On the other hand, the free thermal expansion setup (Figure 67a) features spring loaded clamps, which allow free thermal expansion to study the effects of self-constraints. Testing W disks with these two

different boundary conditions while keeping thermal loading the same reveals the effects of different constraints on tungsten failure.

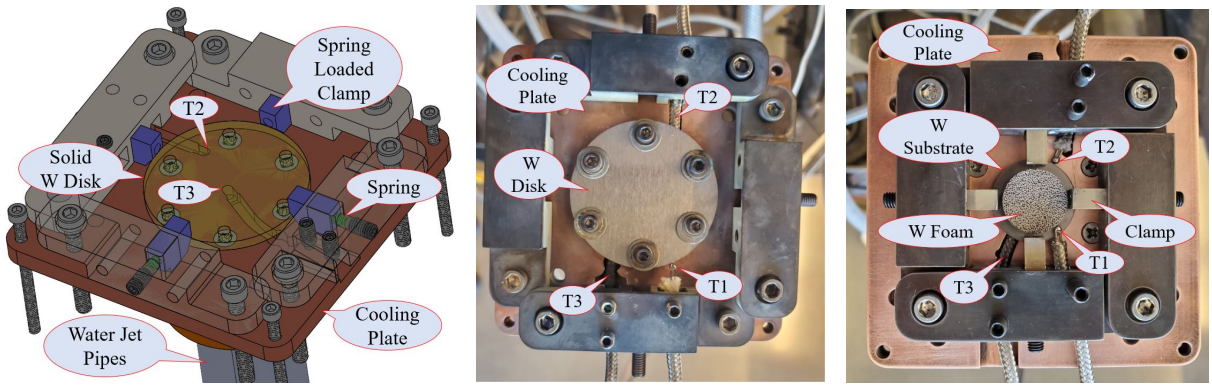

(a) (b) (c)

Figure 67: (a) CAD illustration of apparatus designed to allow W disk free thermal expansion utilizing spring loaded clamps. K-type thermocouples T2 and T3 will be assembled on springs in their designated place on CuCrZr cooling plate pushing the thermocouples on samples cooled face through the entire experiment. (b) The second configuration of the designed apparatus utilized to test fully constrained boundary condition using the 6 bolts on W disk periphery and (c) the third configuration of the apparatus used to test foam/substrate under high heat flux loading in HEFTY.

In these experimental setups (Figure 67) three thermocouples are typically attached to the sample mechanically using set screws. The accuracy of attachment is inspected before each test by running the water jet to the cooling plate and then checking the temperature of each thermocouple against the reservoir water temperature as described in [60]. Thermocouple 1 (T1) measures the sample's temperature at its plasma-exposed face edge, thermocouple 2 (T2) at the edge of W disk cooled face (Figures 67a and 67b) or edge of substrate (Figure 67c) and thermocouple 3 (T3) at the center of the sample's cooled face. Thermal cycling is implemented by controlling the on- and off-times of the high-enthalpy arc-jet plasma using a control system driven by a LabVIEW program. During these tests HEFTY chamber is taken to low vacuum and filled partially with Ar to reduce oxidation. However, some oxidation of the tungsten foam was seen from oxygen introduced by the test system.

Apparatus shown in Figure 67c was used to test tungsten foam samples which were brazed onto tungsten substrates. Here the substrate is forced onto the cooling plate using the 4 stepped clamps enhancing the cooling and allowing free thermal expansion of the foam.

7.4 Modeling Specimen Thermomechanics

Although traditional thermal shock is associated with transient temperature distributions within a sample, the sample geometry and how it is supported at its boundary have significant effects on fracture. We focus here on the influence of boundary and transient conditions on the thermal stress and thermal shock of plastically-deforming materials. We investigate the thermal shock of circular W disk and W foam exposed to a transient heat flux using multiphysics Finite Element (FE) simulations. Results of these simulations will be utilized later to shed light on experimental tests on solid and porous tungsten (W foam) disks. If a disk is totally free to expand when a heat flux is applied on one surface, the top plane normal to the heat flux will expand faster than bottom plane. Additionally, if the heat flux is localized in a central region on the disk surface, the rate of thermal expansion will decrease as a function of the radial distance. In the simplest case where the disk is totally free, such axial and radial temperature gradients can result in the plastic deformation of a central exposed region of the disk, as it is constrained by the cooler part of the disk. Cool-down of the sample is fully elastic because the thermal load is removed, and this can result in residual tensile stresses in the central top region of the sample, with possible fracture during the cool-down phase. The onset of fracture is determined by the magnitudes of the residual stress and associated residual plastic deformation. To show possible modes of fracture due to heating/cooling cycles coupled with external constraints, the sample edge may be allowed to expand freely or to be fully constrained (e.g. by bolting). Thus, possible case studies of sample geometry and boundary conditions are:

1. Free Expansion
    - (1-a): The sample is totally free to expand.
    - (1-b): The sample's cooled face is constrained from out-of plane displacement preventing bending type deformation.
2. Externally-constrained Expansion

7.4.1 Heat Transfer Analysis

We established a space-time heat flux profile within the HEFTY plasma chamber utilizing specially-designed heat flux sensors as described in chapter 5. The main dependencies of the heat flux are described by a number of parameters that are determined by a set of experiments with heat flux sensors. The relationship between the surface heat flux and the radial position r, the axial distance of the sample away from the plasma source x and exposure time t is given in equation 50. The heat flux distribution on sample's exposed face at each distance from arc-jet is shown in Figure 68b and the heat flux profile at the center of a sample located 2.5 cm from arc-jet is plotted in Figure 68a using equation 50. It is important to notice that the heat flux magnitudes reported in Figure 68 which is used through this chapter are slightly higher than the ones presented in chapter 5. The values reported in Figure 68 were our initial measurements including some uncertainties which were resolved in our final measurements reported in chapter 5.

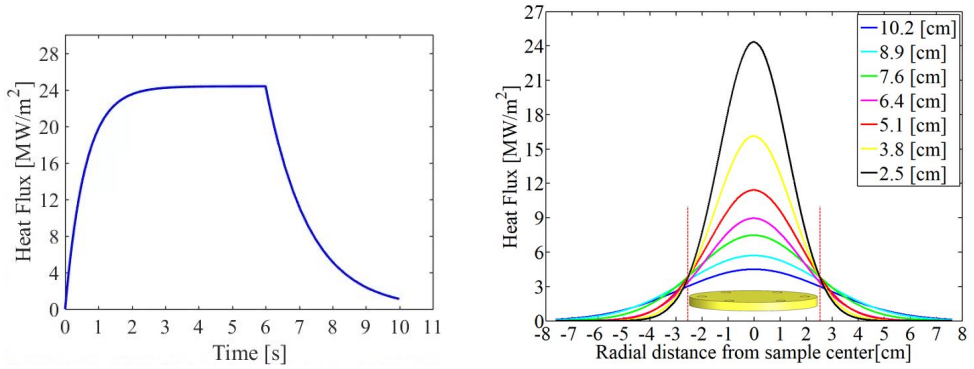

(a) (b)

Figure 68: (a) HEFTY arc-jet Heat flux profile during one cycle (6s arc-jet on-time and 4s off-time) at the center of the exposed face of the sample located 2.5 cm from plasma arc-jet. (b) HEFTY arc-jet heat flux distribution on sample's exposed face at different distances (2.5-10.2 cm) from arc-jet [61]

Multiphysics Finite Element (FE) simulations have been performed with the commercial software COMSOL. In these simulations, heat transfer is coupled with solid mechanics to study samples that are exposed to a cyclic heat flux on their top surface and are attached to a CuCrZr plate (cooling-plate) that is cooled by a water jet from the back side. The results

presented in this section correspond to tests where the top face of the W disk was located at 2.5 cm from the plasma arc-jet experiencing the heat flux profile shown in Figure 68a at the center of the sample's exposed face. Also, at this distance, the radial distribution of the heat flux is measured and plotted [61], as shown in Figure 68b. The W disk samples were exposed to 10 cycles of 6 s thermal heating (plasma arc-jet ON-time) and 4 s plasma arc-jet OFF-time. The exposed face of the W disk reaches to $\approx$ 24 MW/m^2 at the center of the sample during the on-time (Figure 68a), and the bottom face is cooled through conduction to the cooling plate. The temperature profile of the W disk can vary, depending on its assembly method on the cooling plate (fully constrained using the bolts or free thermal expansion). Our experimental temperature measurements from thermocouples placed on the cooling face of the W disk (T2 at the edge of cooled face and T3 at the center of cooled face) showed that the cooling face of the fully constrained sample (bolted sample) stays at a lower temperature compared to the sample that undergoes free thermal expansion. This is attributed to better thermal contact between the cold face of the bolted W disk and the cooling-plate throughout the entire experiment (10 cycles) which can be seen by comparing the experimental temperature measurements (T2 and T3) in Figure 69a with 69b (only one cycle is plotted in these figures). The temperature measurements T2 and T3 shown in Figures 69a and 69b are used in a linear distribution along radial direction on the sample's cooled face as applied time-dependent boundary conditions. The applied temperatures (T2 and T3) are the ones measured after the first few cycles into the test where sample temperature (base temperature) was at 256 °C for the fully-constrained case, and 950 °C for the free-thermal expansion case at the beginning of the cycle.

Temperature-dependent properties of solid W in these simulations are taken from [62], [26], [5]. Figures 69a and 69b display the FE computed temperatures at the center of exposed face and at the edge of exposed face which agrees with our experimental measurements from T1 located at the edge of exposed face.

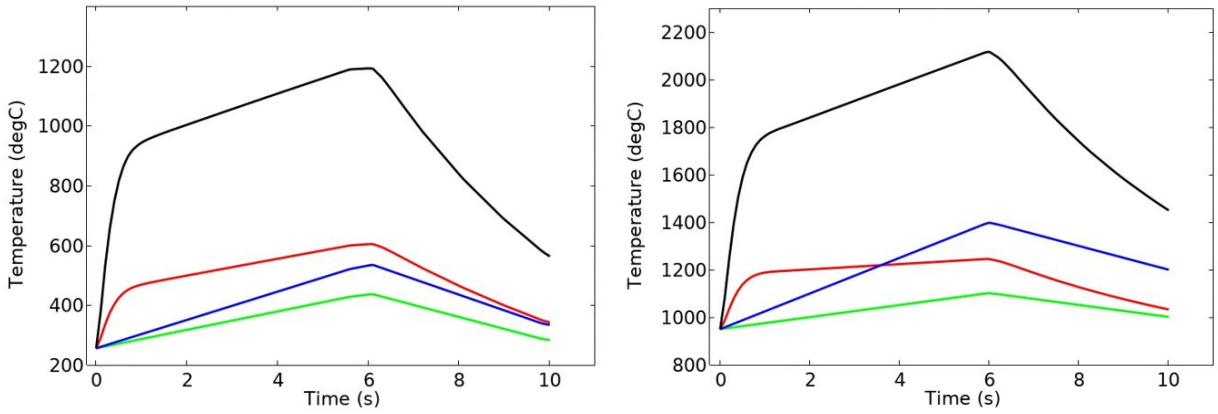

Figure 69: Temperature profile of a thermal loading cycle (6s on-time and 4s off-time) for: (a) Fully-constrained setup (Figure 67b) and (b) free thermal expansion setup (Figure 67a) for W disk with 5.1 cm diameter and 3.4 mm thickness. Green curve is experimental temperature measurements from W disk cooled face edge (T2 in Figures 67a and 67b) and blue curve is the one measured at the center of W disk cooled face (T3 in Figures 67a and 67b) which are used as time dependent boundary conditions in our simulations. The red curve is FE computed temperature at W disk exposed face edge and the black curve is the one computed at the center of exposed face.

Additional results obtained from heat transfer analysis for the fully-constrained and the free thermal expansion setups are shown in Figures 70 and 71, respectively.

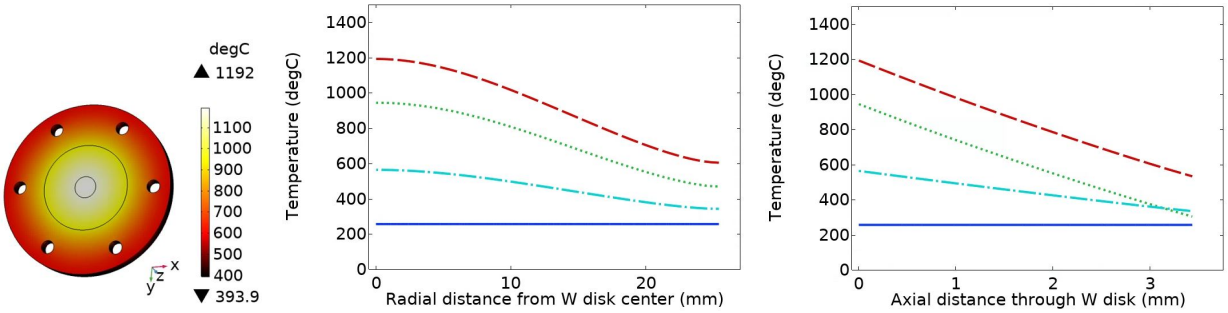

Figure 70: FE heat transfer results for the fully-constrained (bolted) setup (Figure 67b) for the W disk with 5.1 cm diameter and 3.4 mm thickness showing (a) W disk exposed face temperature distribution at the end of thermal loading (6s arc-jet on-time), (b) radial temperature distribution on the exposed face showing temperature decay closer to the sample edge due to the exponential decay of the heat flux in radial direction and (c) axial temperature distribution through the thickness of the W disk at its center. The dark blue solid line shows the temperature at t=0, the green dots at t=1s, the red dash line at t=6s and the light blue dash-dot at t=10s.

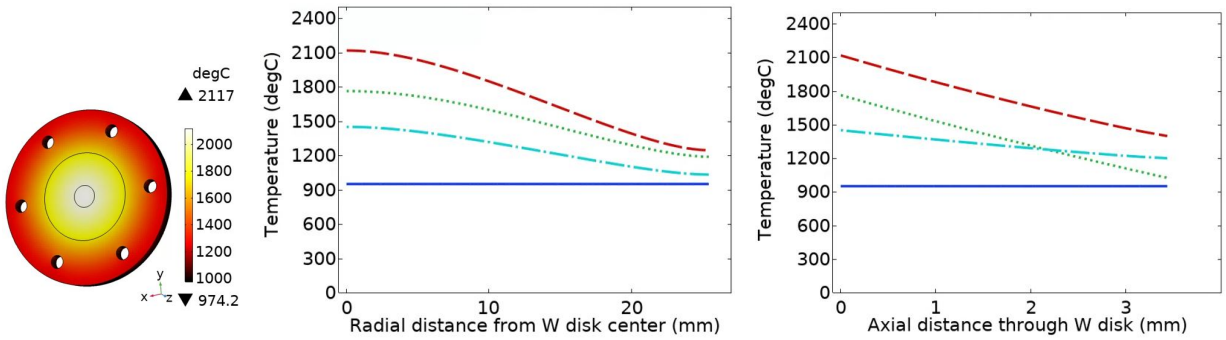

(a) (b) (c)

Figure 71: FE heat transfer results for the free thermal expansion setup (Figure 67a) for the W disk with 5.1 cm diameter and 3.4 mm thickness showing (a) W disk exposed face temperature distribution at the end of thermal loading (6s arc-jet on-time), (b) radial temperature distribution on the exposed face showing temperature decay closer to the sample edge due to the exponential decay of the heat flux in radial direction and (c) axial temperature distribution through the thickness of the W disk at its center. The dark blue solid line shows the temperature at t=0, the green dots at t=1s, the red dash line at t=6s and the light blue dash-dot at t=10s.

7.4.2 FE Simulations of Stress Evolution in Solid W Samples

FE Structural analyses are performed using temperature-dependent material properties including plasticity with a linear hardening model based on a temperature-dependent tangent modulus for tungsten. These analyses are done for both fully constrained and free thermal expansion cases which are described in details in following sections including some key results from simulations.

7.4.2.1 Bolted W Disk (Fully Constrained)

Thick samples have enough bending rigidity to resist buckling as a result of edge constraints that prevent radial thermal expansion. Samples will tend to undergo membrane deformation (in-plane), and if thermal strain cannot be accommodated elastically, then plastic strain will generate permanent deformation (residual strain) upon heat-up. To simulate the structural response of fully-constrained W disk (bolted), we applied a zero displacement condition on the cylindrical surfaces of all bolting holes and constrained the cooled face of W disk from out-of-plane displacement. The hoop stress and effective plastic strain at the end of the

heat-up phase are shown in Figure 72. As expected, during sample heating the hoop stress is compressive on the hot face and tensile on the cooled face except near the bolt holes. Apart from the localized high stresses at the bolts, the compressive stress on the hot face results in generating a central zone of plasticity, with strains approaching 0.5%. While localized plastic zones at the bolts will tend to relax stresses, formation of the central plastic zone at the hot face is significant because it can result in tensile stresses upon sample cool-down.

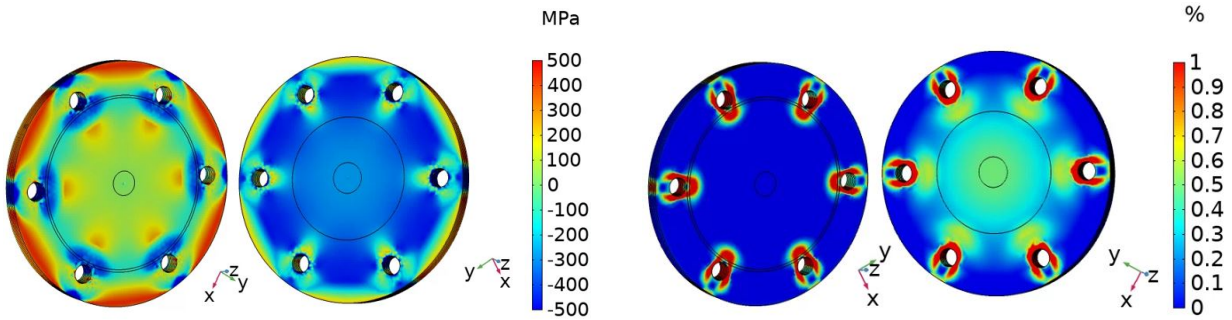

(a) (b)

Figure 72: (a) Hoop stress on the exposed (right) and cooled (left) faces and (b) effective plastic strain on the exposed (right) and cooled (left) faces of a solid W disk (5.1 cm diameter, 3.4 mm thickness) under fully-constrained condition (bolted) after heat-up to maximum temperature at the end of thermal loading (6s arc-jet on-time) shown in Figure 70a.

The accumulated plastic strain during sample heat-up (Figure 72b) results in residual stresses upon cool-down. Figure 73 shows the hoop stress distribution on W disk after cool-down to room temperature. It can be seen that stress state is tensile through the thickness at the center of the disk (Figure 73b) and along radial direction on both exposed and cooled face (Figure 73c) all the way to the edge of the disk where we see some compressive stress. The intense levels of stresses on the exposed face indicates that if fracture occurs, it will most likely take place on this face during cool-down. This point will be discussed further in the experimental results section.

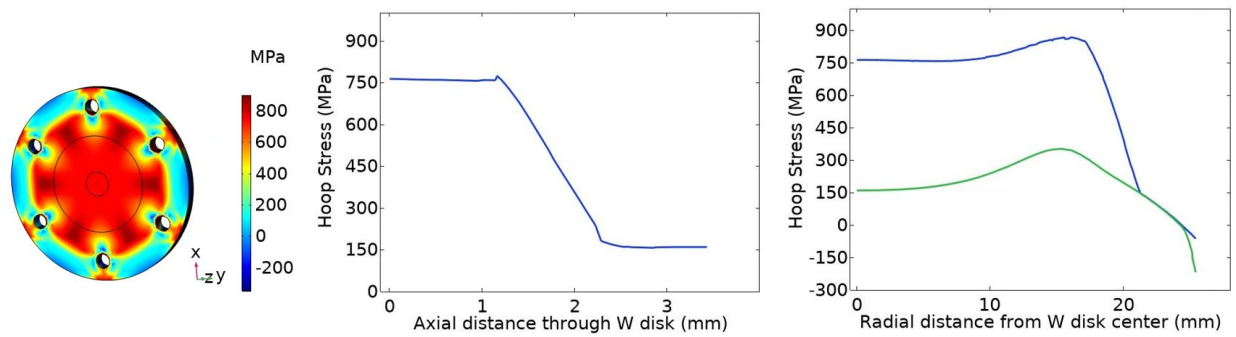

(a) (b) (c)

Figure 73: FE results for W disk (5.1 cm diameter, 3.4 mm thickness) under fully constrained condition (bolted) after cool-down to room temperature showing (a) hoop stress on the exposed face, (b) axial distribution of hoop stress at the disk center and (c) radial distribution of hoop stress on the exposed face plotted in blue and cooled face plotted in green.

7.4.2.2 Clamped W Disk (Free Thermal Expansion)

When the W disk is constrained with spring loaded clamps as shown in Figure 67a, thermal expansion can be partially accommodated by the clamps allowing free thermal expansion and self-constraint will develop where the expansion of the hotter region (center of disk) is constrained by the cooler regions (perimeter). Setting up the FE analysis to simulate this experimental condition one can setup the problem either as free thermal expansion allowing out-of-plane deformation or free thermal expansion constraining out-of-plane deformation. These two cases are described in detail in following sections. Stress states obtained from simulations for these two cases can be studied along with the damage observed from this experiment to determine which condition was hold during experiment having W disk assembled with spring loaded clamps.

Case I (Free expansion and allowing out-of-plane displacement):

Here, the W disk is free to expand radially and can also bend towards the plasma because of the axial gradient in the temperature field promoting faster expansion of the top surface as compared to the bottom surface. This condition is similar to applying an edge moment that causes the disk to curve towards the surface. The simulation is performed in COMSOL by prescribing zero displacement in the x-direction at 4 points on the z-y plane of symmetry, zero prescribed displacement in the y-direction at 4 points on the z-x plane of symmetry,

and zero prescribed displacement in the z-direction at 2 points on the x-y plane. The x-y-z coordinate system is shown in Figure 74a. These boundary conditions prevent free body motion of the disk and allow free radial expansion as well as out-of-plane displacement. The results of this simulation are shown in Figure 74 at the end of the heat-up part of the cycle, and in Figure 75 at the end of the cool-down phase. It is interesting to note that during sample heating, the top surface of the sample is in a state of tension at the sample outer region and compression in the central zone. The same trend is observed on the bottom face where the entire bottom surface is under tension except for the small central zone. The stress state changes during sample cool-down, as can be seen in Figure 75a, where tensile stress develops in the central zone of the exposed face. Axial and radial stress distributions upon cool-down are also shown in Figures 75b and 75c.

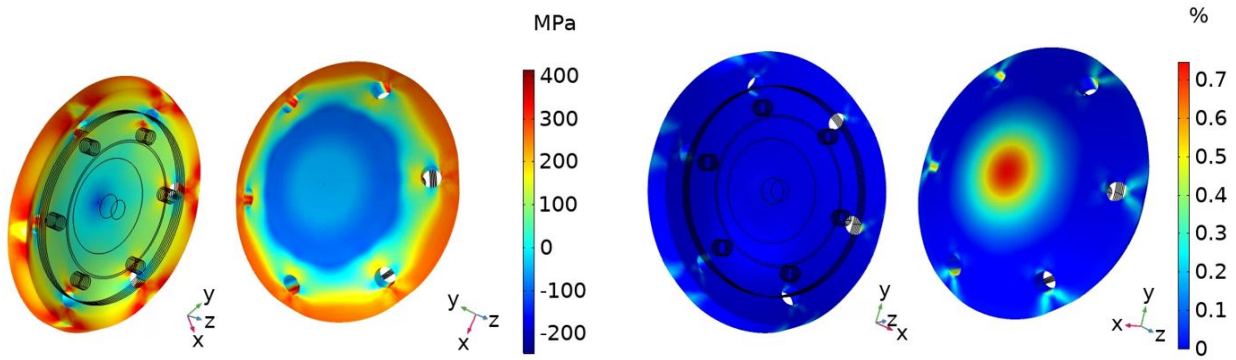

(a) (b)

Figure 74: (a) The hoop stress on exposed (right) and cooled (left) faces and (b) effective plastic strain on exposed (right) and cooled (left) faces of the solid W disk (5.1 cm diameter, 3.4 mm thickness) under free radial expansion and free out-of-plane displacement boundary conditions after heat-up to maximum temperature at the end of thermal loading shown in Figure 71a (the deformation is exaggerated 50 times).

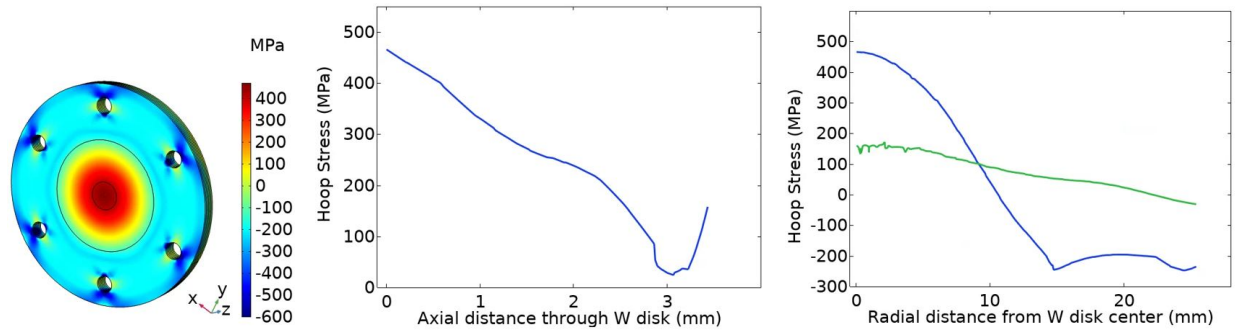

(a) (b) (c)

Figure 75: FE results for W disk (5.1 cm diameter, 3.4 mm thickness) under free radial expansion and free out-of-plane displacement boundary conditions after cool-down to room temperature showing (a) hoop stress on the exposed face, (b) axial distribution of hoop stress at the disk center and (c) radial distribution of hoop stress on the exposed face plotted in blue and cooled face plotted in green.

Case II (Free expansion and constraining out-of-plane displacement):

Here, the FE model is setup as described in the previous case. However, the entire cooled face of the W disk is constrained from any out-of-plane (z-axis) displacement. Structural analysis results during the heat-up and cool-down phases of the cycle are shown in Figures 76 and 77, respectively.

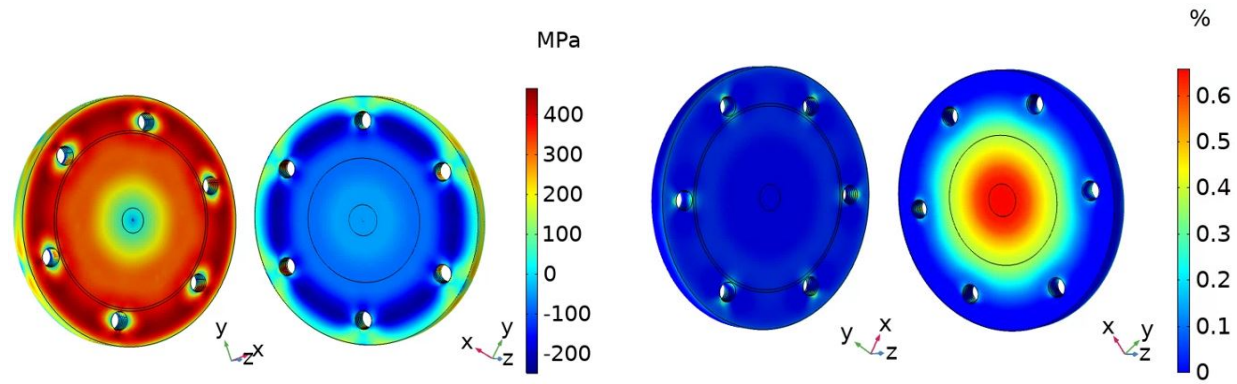

(a) (b)

Figure 76: (a) The hoop stress on the exposed (right) and cooled (left) faces, and (b) The effective plastic strain on the exposed (right) and cooled (left) faces of the W disk (5.1 cm diameter, 3.4 mm thickness) under free radial expansion and constrained out-of-plane displacement of cooled face after heat-up to its maximum temperature at the end of the thermal loading shown in Figure 71a.

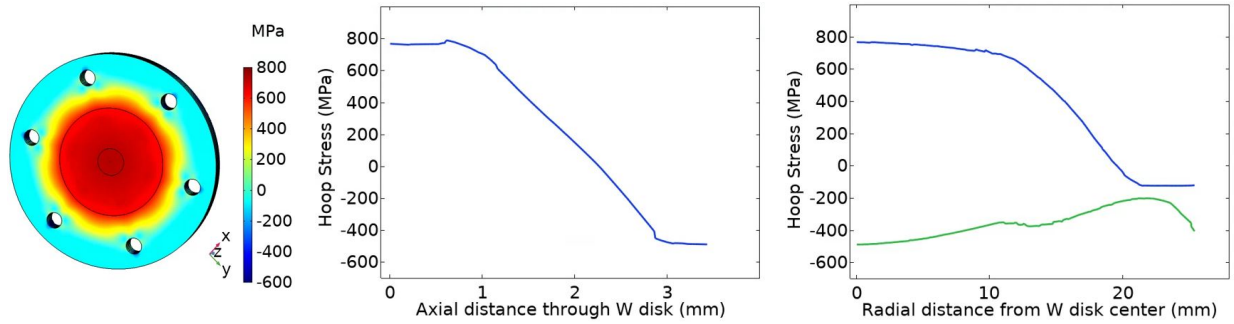

Figure 77: FE results for W disk (5.1 cm diameter, 3.4 mm thickness) under free thermal expansion and constrained out of plane displacement of cooled face after cool-down to room temperature showing (a) hoop stress on the exposed face, (b) axial distribution of hoop stress at the disk center and (c) radial distribution of hoop stress on the exposed face plotted in blue and cooled face plotted in green.

In this case the stress state is all compressive on the exposed face and tensile on the cooled face during heat-up as shown in Figure 76a. It can be seen from Figure 77c that upon cool-down the stress state reverses and the exposed face goes entirely under tension (except the edge of the disk which is slightly compressive) and the cooled face under compression.

Structural analysis demonstrated that for both cases the sample undergoes compressive plastic deformation at the center of the exposed face during heat-up (Figures 74b and 76b), where the heat flux is maximum and the yield strength is small at high temperature. The accumulated plastic strain during sample heat-up can introduce tensile residual stresses at the center of the exposed face during cool-down, as shown in Figures 75a and 77a. This, in turn, can develop micro-cracks in this region of the sample. The stress state obtained in Case I and II will be analysed with experimental observations in the results section.

7.4.3 Heat Transfer Analysis of W Foam Samples

Heat transfer analysis for W foam samples were performed on the W foam/substrate assembly. The foam was modeled as a homogeneous material with effective properties obtained from prior computer simulations [40] or from correlations [51]. The heat flux was applied in two components. The first is an effective surface heat flux (q_s) adjusted by the fractional

surface area of the foam ligaments ($f_v^{2/3}$), where f_v is the volume fraction (relative density). The second and remaining component is modeled as a volumetric heat source q_v deposited exponentially from the surface with an extinction length, as detailed in reference [63]. These are given by:

$$q_s = f_v^{2/3} q(r,t,x), \quad q_v = (1 - f_v^{2/3}) H(z) q(r,t,x), \quad H(z) = 1340 \exp(-1340z) \tag{51}$$

Here, z (m) is the distance into the foam surface, $H(z)$ is heat deposition function having its maximum value at the top face of the foam ($z = 0$). Also, in order to simulate the exact experimental conditions, we applied $q(r,t,x)$ to the top face of the exposed substrate outside the foam armor. The FE simulations were performed for a thermal loading cycle which starts at 360 °C as a base temperature for the foam/substrate. Time-dependent temperature boundary conditions were applied to the cooled face of the substrate, which were obtained directly from experimental measurements of each test. The substrate cooled face temperature increased from 360 °C to 526 °C during the plasma arc-jet on-Time (6s) and decreased to 370 °C at the end of the cycle after 4s of cooling time (the blue curve shown in Figure 78b). The following temperature dependent effective foam properties were used in our heat transfer and solid mechanics multiphysics simulations: $E_e(T) = f_v^2 E(T)$, $\sigma_{y,e}(T) = f_v^{2.2} \sigma_y(T)$, $c_{p,e} = c_p(T)$, $k_e(T) = (-1.24 f_v^3 + 2.29 f_v^2 - 0.059 f_v + 0.012) k(T)$.

In the equations listed above, E_e and $c_{p,e}$ are the effective Young's modulus and specific heat of W foam. These are functions of the properties of solid W (E, c_p) and the foam's volume fraction f_v [51]. Here, we assumed that the effective tangent modulus ($E_{t,e}$) scales with f_v similar to Young's modulus. The foam effective yield strength ($\sigma_{y,e}$) and thermal conductivity (k_e) are obtained by careful and detailed FE simulations of a W foam sample that was geometrically reconstructed from X-ray tomography, meshed for FE analysis, and studied for a variety of f_v and PPI conditions [40, 63]. $\sigma_{y,e}$ and k_e are functions of the solid W properties and the foam's volume fraction, f_v. The thermal expansion coefficient of the foam was taken to be the same as that of solid W [51].

FE heat transfer simulations were then performed for a case where the foam's exposed face is 3.8 cm from the plasma arc-jet ($x = 3.8\ cm,\ q_0(x) = 16.13\ MW/m^2$). Temperature

distributions from this study are shown in Figures 78 and 79.

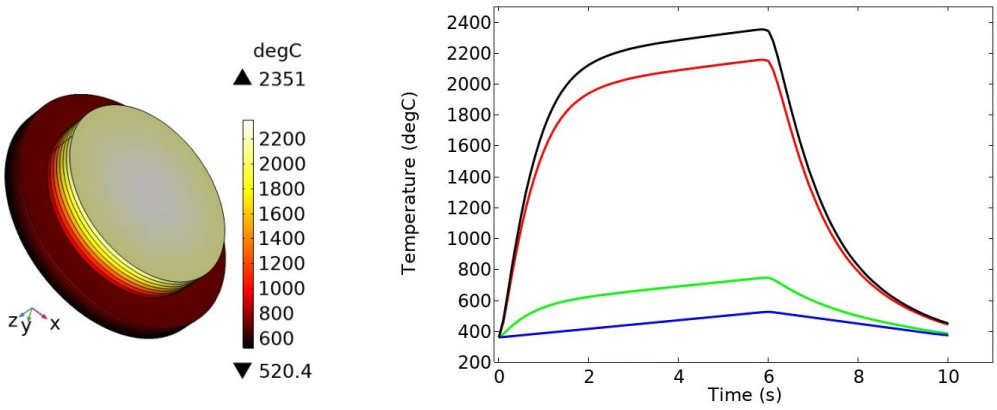

(a) (b)

Figure 78: Temperature distributions for a W foam/substrate sample at 3.8 cm from the plasma arc-jet showing (a) temperature profile on the exposed face at the end of thermal loading after 6s on-time, and (b) temperature profiles of a loading cycle with 6s on-time and 4s off-time. The blue curve is the measured experimental temperature on the cooled substrate center (T3 shown in Figures 67c), which is used as a time-dependent boundary condition. The black curve is the FE computed temperature at the W foam exposed face center, the red curve is at the W foam exposed face edge, and the green curve is at the substrate exposed face edge.

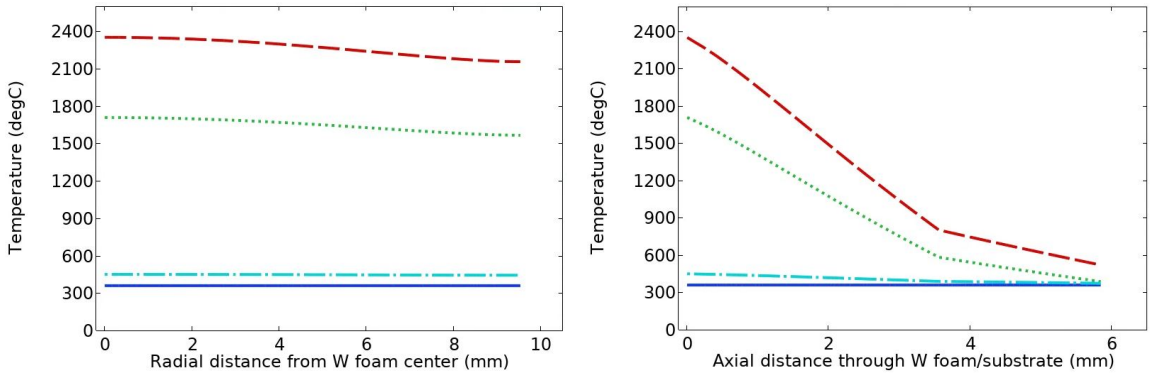

(a) (b)

Figure 79: Temperature distributions for the foam/substrate sample at 3.8 cm from the plasma arc-jet showing (a) radial distribution on the foam exposed face and (b) axial distribution through the thickness of the foam (3.6 mm) and substrate (2.3 mm). The dark blue solid line shows the temperature at t=0, the green dots at t=1s, the red dashed line at t=6s, and the light blue dash-dot line at t=10s.

The foam's exposed face temperature reached 2350 °C at the end of the heat-up phase (Figure 78a) due to its lower thermal conductivity k_e compared to solid W. The influence of

the lower thermal conductivity of porous W is reflected in Figure 79b, where the temperature changes more rapidly in the W foam section (0 - 3.6 mm through W foam/substrate) compared to the solid W substrate (3.6 - 5.9 mm through W foam/substrate). The lower thermal conductivity of the W foam helps to keep the W substrate at a lower temperature preventing its recrystallization. Thus, the W foam can be used as an armor on top of structural solid W in high heat flux applications to prevent extreme temperature effects on solid W and prevent recrystallization. Careful analysis needs to be performed to optimize the foam structure to keep its temperature below the melting point, yet protect the underlying substrate. Similar methods have been developed in thermal protection of jet engine turbine blades with a porous layer of plasma-sprayed ceramic on top of the blade's nickel-based superalloy [64].

7.4.4 FE Simulations of Stress Evolution in W Foam Samples

Structural analyses were performed on the foam/substrate sample by applying boundary conditions to fix the substrate cooled face from out-of-plane displacement and preventing free body motion by prescribing zero displacements in the x-direction at 4 points on the substrate's z-y plane of symmetry and in the y-direction at 4 points of the substrate's z-x plane of symmetry. This boundary conditions allows free radial thermal expansion to simulate our experimental conditions shown in Figure 67c. The *effective* thermophysical properties of W foam were used in all simulations. Our structural analysis includes plasticity with temperature dependent linear hardening for the foam/substrate assembly. Stress distributions and the equivalent effective plastic strain at the end of the 6s arc-jet on-time are shown in Figure 80.

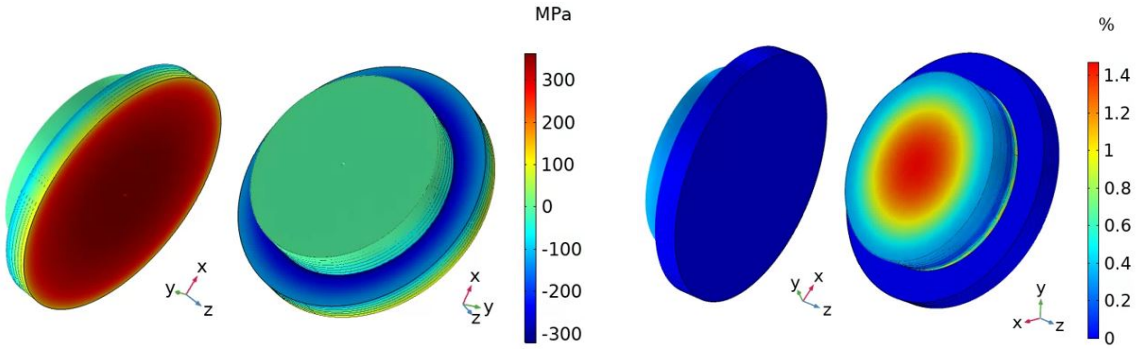

(a) (b)

Figure 80: (a) The hoop stress on the W foam exposed face (right) and the substrate cooled face (left), and (b) the equivalent effective plastic strain on the W foam exposed face (right) and the substrate cooled face (left) under free radial expansion and constrained out-of-plane displacement on the substrate cooled face after heat-up to the sample's maximum temperature (Figure 78a) at the end of thermal loading (6s arc-jet on-time) at 3.8 cm from the plasma arc-jet.

Having extreme temperatures (2350 °C) on the W foam exposed surface (Figure 78a) reduces its "effective" yield strength ($\sigma_{y,e}$) to ≈ 8 [MPa], for f_v=43%. The exposed foam surface shows compressive hoop stress (≈-8 [MPa]) with an effective plastic strain reaching 1.4 %, as shown in Figure 80b. Thanks to the foam's low thermal conductivity, the substrate temperature didn't exceed ≈ 520 °C (Figure 78a), thus keeping a relatively high yield strength of ≈ 430 [MPa]. Because of this high yield strength, the substrate material remained elastic throughout the heat-up phase (Figure 80b). The accumulated compressive plastic strain at the end of the heat-up phase at the center of foam's exposed face (Figure 80b) generates residual stresses on the foam/substrate during cool-down. FE simulation results at the end of the cool-down phase are shown in Figure 81.

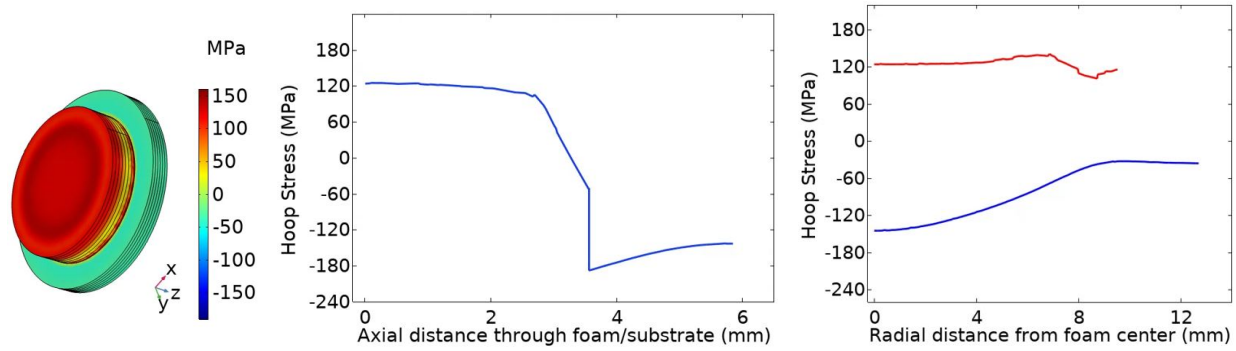

(a) (b) (c)

Figure 81: FE results for W foam/substrate under free thermal expansion and constrained out-of-plane displacement on substrate cooled face after cool-down to room temperature showing (a) hoop stress on the exposed face, (b) axial distribution of hoop stress at the foam/substrate center (zero is at the foam exposed face) and (c) radial distribution of hoop stress on the foam exposed face plotted in red and at the cooled surface of substrate plotted in blue (zero is at the center of the foam/substrate).

Upon cool-down to room temperature, the exposed face of the foam goes under residual tensile stress reaching ≈140 [MPa] (Figure 81a), thus exceeding $\sigma_{y,e}$ at room temperature and increasing the magnitude of the effective plastic strain on the foam. Tensile plastic strain at room temperature can cause micro-cracks in foam ligaments and at triple junctions which will be discussed further in experimental results section. Axial and radial distribution of hoop stress (Figures 81b and 81c) shows tensile stress on foam exposed face and compressive stress on substrate cooled face upon cool-down to room temperature.

7.5 Experimental Results

An extensive series of experiments on solid W and on W foam have been carried out to determine the effects of intense heating on the thermomechanical behavior under a variety of conditions. First, a set of W foam samples were exposed to the low-energy helium plasma at the PISCES lab at UCSD (USA) to study the effects of helium plasma on the foam surface texture and structure. These samples were subsequently tested with intense heating of two limiting conditions: (1) long-duration, high-enthalpy cyclic heating in the HEFTY arc-jet facility at UCLA (USA); and (2) very short duration, high-power cyclic laser heating at the PSI-2 facility in Forschungszentrum Jülich (Germany). Another set of as-fabricated

solid W disk samples were tested in the HEFTY Arc-jet facility at UCLA for comparison. The conditions for these samples are summarized in table 2. The results of these tests with a variety of conditions, and the understanding based on thermo-structural modeling are presented next.

Table 2: Samples description and loading conditions for cyclic high heat flux tests performed in HEFTY with 10 cycles of 6s arc-jet on-time and 4s off-time. D1 to D8 are solid tungsten samples and F1 to F3 are tungsten foam samples with $f_v = 43\%$. F1 and F2 are 80 PPI and F3 is 65 PPI. The last 2 columns describe He plasma testing conditions (He fluence and temperature) performed on F1-F3 at the PISCES lab at UCSD prior to HEFTY tests at UCLA. He plasma tests caused no cracking or mechanical damage on the foam but resulted in a W-fuzz layer on the ligaments. D stands for diameter, t thickness, B.C. boundary conditions, x distance between sample surface and arc-jet exit plane, q''_{max} is the maximum heat flux, and $T_{\text{top face}}$ is the maximum temperature at sample exposed face in HEFTY.

Sample ID	D (cm)	t (mm)	B.C.	x (cm)	q''_{max} MW/m^2	$T_{\text{top face}}$ [K]	Recrystallized	Cracked	He fluence [10^{25} m^{-2}]	Temp [K]
Solid W - External-Constraint										
D1	5.1	0.5	Bolted	2.5	24.4	3473	✓	✓	-	-
D2	5.1	0.5	Bolted	5.1	11.4	2073	✓	X	-	-
D7	5.1	3.4	Bolted	2.5	24.4	1465	X	✓	-	-
D8	5.1	3.4	Bolted	2.5	24.4	1465	X	X	-	-
Solid W - Self-Constraint										
D3	2.5	3.4	Free	2.5	24.4	2390	✓	✓	-	-
D4	5.1	3.4	Free	2.5	24.4	2390	✓	✓	-	-
D5	5.1	3.4	Free	2.5	24.4	2390	✓	✓	-	-
D6	5.1	3.4	Free	3.8	16.1	1473	X	✓	-	-
Porous W Foam - Self-Constraint										
F1	2.0	3.6	Free	3.8	16.1	2623	✓	✓	5	1100
F2	2.0	3.6	Free	3.8	16.1	2623	✓	X	10	1200
F3	2.0	3.6	Free	3.8	16.1	2623	✓	X	5	1100

7.5.1 Low-Energy Helium-Plasma Effects on W foam

The W foam armor for Plasma-Facing Components (PFCs) will be subjected to a high fluence of low-energy helium and hydrogen plasma that can cause erosion and surface morphology changes. The armor must also survive the high heat flux due to plasma transients. To mimic

this environment, we first tested a number of W foam samples in the linear plasma device (PISCES) at UCSD, which provides conditions for high fluence, low energy (100-200 eV) helium plasma similar to what is expected in a Tokamak reactor, but without the intense heating due to severe transients. Then we tested samples for the severe thermomechanical transients at the HEFTY and PSI-2 facilities.

The samples were exposed to a low energy (100-200 eV) continuous helium plasma, where the conditions are shown in Table 2. For PISCES tests, the key parameters are shown in the last two columns (helium ion fluence and sample temperature). On the other hand, the key parameters for the HEFTY thermomechanical tests are the distance to the plasma arc-jet, which determines the heat flux, and the pulse duration (6 s on-time and 4 s off-time).

The primary goal of the low-energy helium plasma exposure tests at UCSD was to determine the sputtering and erosion rate of the open-cell W foam (see our work in reference [63] for details). Since the fluence is low, no significant mechanical damage was detected for these samples. Hence, they were subsequently tested in the HEFTY facility to determine their thermomechanical response to intense heating transients. We discuss here the microstructure observations of one of the samples that were tested at PISCES first before the HEFTY tests. We selected the F2 foam sample, which was exposed to helium plasma at 1200 K with ion energy of 200 eV at a fluence of 1×10^{26} m^{-2} because of the higher helium plasma exposure temperature (1200 K) resulting in more dramatic effects on the surface texture. The overall structure of the open-cell foam remained intact with no micro-cracks after the helium plasma exposure. However, the surface texture of the foam changed, exhibiting nano-scale tendrils (fuzz). More detailed surface texture (fuzz) can be seen in Figure 82, where a higher resolution image of the top layer of ligaments directly facing the plasma is shown in Figures 82b.

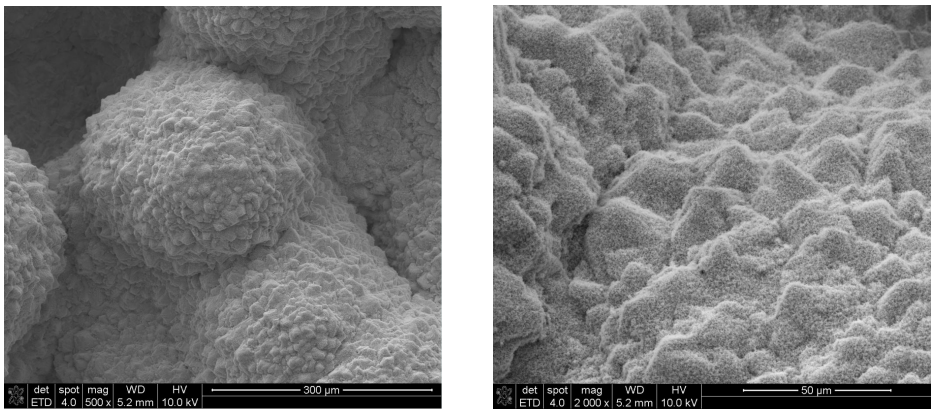

(a) (b)

Figure 82: Appearance of F2 after exposure to helium ion flux of 10^{26} m^{-2} with an average ion energy of 200 eV and at a temperature of 1200 K showing (a) pyramid shape surface structures of foam ligaments getting covered with W-fuzz after helium plasma exposure and (b) higher magnification image of the new surface texture (fuzz).

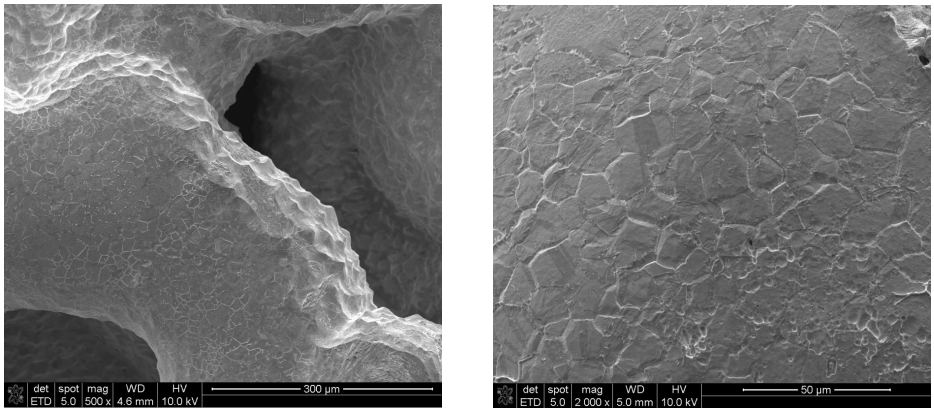

(a) (b)

Figure 83: Appearance of F2 after exposure to HEFTY arc-jet plasma ($\approx$ 16.1 MW/m^2) for 10 cycles of 6s arc-jet on-time and 4s off-time showing (a) removed pyramid shape structures on exposed face of ligaments and (b) eliminated fuzz surface texture and recrystallized foam.

The results of helium ion irradiation tests performed at UCSD showed that, relative to solid tungsten, the main benefit of the 3D foam architecture is ion shadowing, protecting ligaments beneath from fuzz growth by allowing microscopic damage to occur on the ion-facing ligaments only. In addition, the foam ligament geometry causes ions to impact at higher incident angles, leading to greater ion back-scattering. Textured tungsten coatings deposited on the surface of foam ligaments (pyramid shape structures in Figure 82a) provided

additional damage reduction for the ion-facing ligaments simply by increasing surface area and ion back-scattering, thereby reducing effective ion fluence.

7.5.2 The Effects of High-Enthalpy Arc-Jet Plasma

7.5.2.1 The Effects of Heat Flux on Thin W Disks

A series of experiments were performed to investigate the effects of high heat flux on W re-crystallization, grain growth, and crack initiation and propagation. Prior to plasma exposure, a focused ion beam (FIB) cross-section was taken and ion-contrast imaging was used to evaluate the initial grain structure. Elongated lamellar structure of W grains were observed as a result of rolling, and the lamellar thickness was measured to be $6.2 \pm 2.4\ \mu m$ with an average grain size of $\approx$ 7-10 μm. In these tests W disks with 0.5 mm thickness and 5.1 cm diameter were fully constrained using 6 bolts, similar to the sample shown in Figure 67b. The disks were thermally loaded for 10 cycles of 6s arc-jet on-time and 4s off-time while being continuously cooled from the back side connected to the cooling plate. We performed this test once at a distance of 2.5 cm from the arc-jet and once at 5.1 cm. The heat flux distribution at these distances from the arc-jet are shown in Figure 68b. It can be seen that at 2.5 cm from the arc-jet the center of W disk was exposed to 24.4 MW/m^2, which decreased to 3.8 MW/m^2 at the edge of the disk. However, at 5.1 cm from the arc-jet, the heat flux at the center of W disk was 11.4 MW/m^2 decreasing to the same value of 3.8 MW/m^2 at the edge of the W disk. Temperature measurements showed that the exposed face of D1 (exposed at 2.5 cm from the arc-jet) exceeded the tungsten re-crystallization temperature (1300°C) during it's thermal loading causing re-crystallization with larger grains ($\approx$ 200 μm) at the center of the sample and smaller grains ($\approx$ 40 μm) near its edge, as shown in Figure 85. The radial exponential decay of the heat flux from the arc-jet (Figure 68b) caused a radial temperature gradient on the exposed face of D1, which resulted in a gradual grain size distribution, as shown in Figure 85b. It is interesting to note that while D1 showed considerable grain growth as a result of recrystallization, the average grain size of D2 (exposed at 5.1 cm from arc-jet) did not change as much due to the smaller heat flux and lower temperature on this sample.

The average post-exposure grain size for D2 is measured to be 15 μm as shown in Figure 85b. To measure changes in grain size with respect to the radial distance form the W disk center, a line-intersection method was used at varying radial distances for D1 and D2. The grain size distribution is shown in Figure 85b. The contrast between the grain size in D1 and D2 is illustrated in Figure 84, where D1 shows substantial grain growth during the brief periods of high-temperature exposure. Both D1 and D2 recrystallized and showed plasma etching that resulted in grain boundary and grain orientation visibility, as shown in Figure 84. The arc-jet plasma had a preferential etching effect on the grain boundaries and along preferred crystallographic orientations that resulted in grain boundary and grain orientation visibility (Figure 84c). The etching is similar to what is observed after targeted chemical etching for metallographic sample preparation in order to visualize grain boundaries. The grain structure is visible for both D1 and D2 up to a distance of 10 mm from the center of the sample. Several studies on recrystallization of W have shown that W is embrittled after recrystallization [65, 66]. They concluded that grain growth and embrittlement involving impurities segregated at the grain boundaries was responsible for initiating brittle cracks at grain boundaries [65] which is also observed in our test on D1 as shown in Figures 87b and 87c.

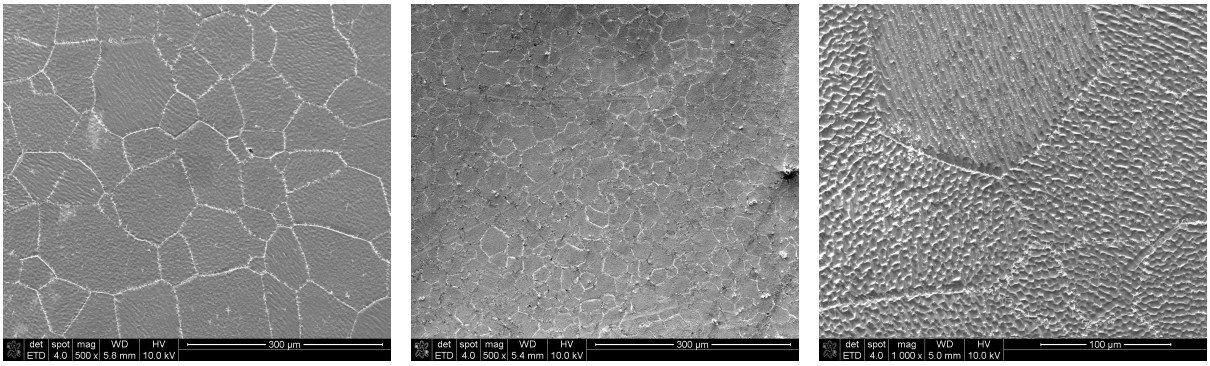

(a) (b) (c)

Figure 84: Exposed face post-exposure SEM images showing (a) D1 grain distribution, (b) D2 grain distribution and (c) etched grain boundaries and orientation-dependent patterning and preferential etching on D1.

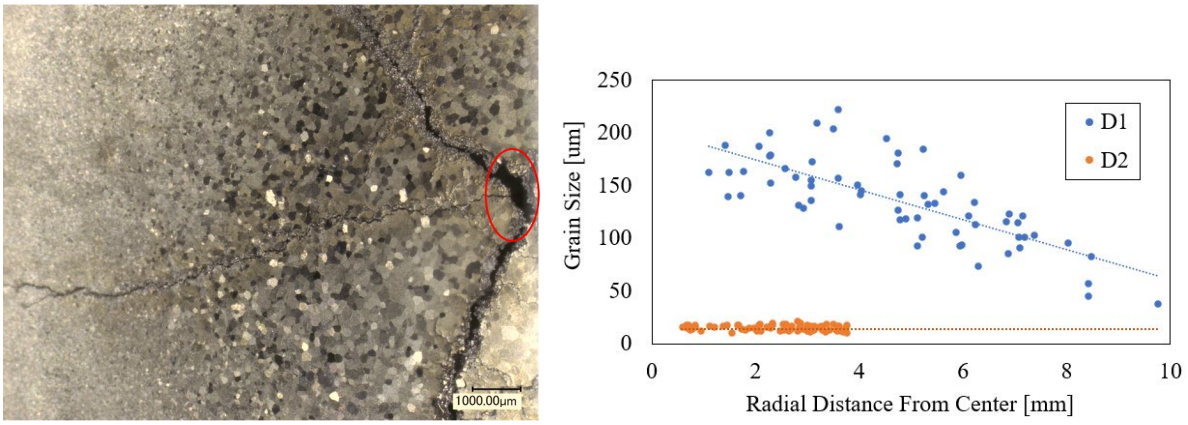

(a) (b)

Figure 85: (a) Post-exposure optical microscopy image of D1 etched under plasma loading showing radial grain size distribution with respect to sample's center (center of loading) marked in red. (b) Grain size as a function of radial distance from sample center for D1 and D2.

Post-exposure analysis of the D1 sample showed considerable damage including cracking, buckling of the central zone, and material ejection at crack edges, as shown in Figure 86a. A higher magnification SEM image of the crack center is shown in Figure 87a. Several prominent damage modes are visible for D1 (Figure 87), with the most obvious one at the center of the sample where five cracks originated and propagated to the edge of the sample. D1 had a FIB cut on its exposed face center, which acted as a crack initiation point for these large cracks. At their origin, these cracks are ductile in nature with Crack Opening Displacement (COD) reaching 250 μm, with considerable amount of ductile tearing around the crack edges (Figure 87a). The ductile nature of the cracks in the center of the sample, combined with the ejected material at their edges, suggest that these cracks formed during heat-up by tensile stresses from buckling (bending type stress). The ductile cracks continue outward across the sample till they transition to a sharp, brittle failure mode at the edge of the exposed zone, as shown in the higher magnification image of Figure 86a. Several purely brittle cracks (Figure 87b) were observed with flat and clean fractured faces and crack paths that often followed grain boundaries (inter-granular cracks), as shown in Figure 87c. In contrast to ductile cracks, the COD of brittle cracks was approximately 30 μm, and no ejected material was observed at crack edges. Additionally, brittle cracks were blunted before

reaching the edge of the sample, possibly due to overall sample accommodation of thermal strains through buckling, plasticity, and fracture. The contrasting features of the purely brittle and ductile cracks suggest that they formed at different times during the experiment. Brittle cracks may have formed during cool-down, and most likely due to residual thermal stresses. As a result of the lower heat flux, the damage to sample D2 is minimal in comparison to sample D1, as is illustrated in Figure 86. Sample D2 was free of cracks after exposure. The only observed damage was slight buckling and out of plane deformation at the center to accommodate thermal strain.

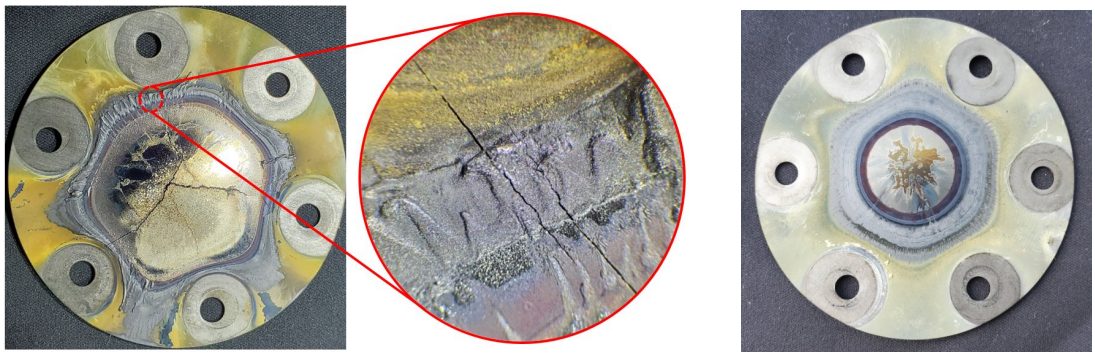

(a) (b)

Figure 86: Optical post-exposure image of (a) D1, thermally loaded at 2.5 cm from the arc-jet showing ductile cracking at the center of the sample and brittle cracking close to its edge. (b) D2, thermally loaded at 5.1 cm from the arc-jet showing no cracks. Both of these samples are 0.5 mm thick with 5.1 cm diameter and were fully constrained (bolted as shown in Figure 67b) and exposed to 10 cycles of 6s arc-jet on-time and 4s off-time.

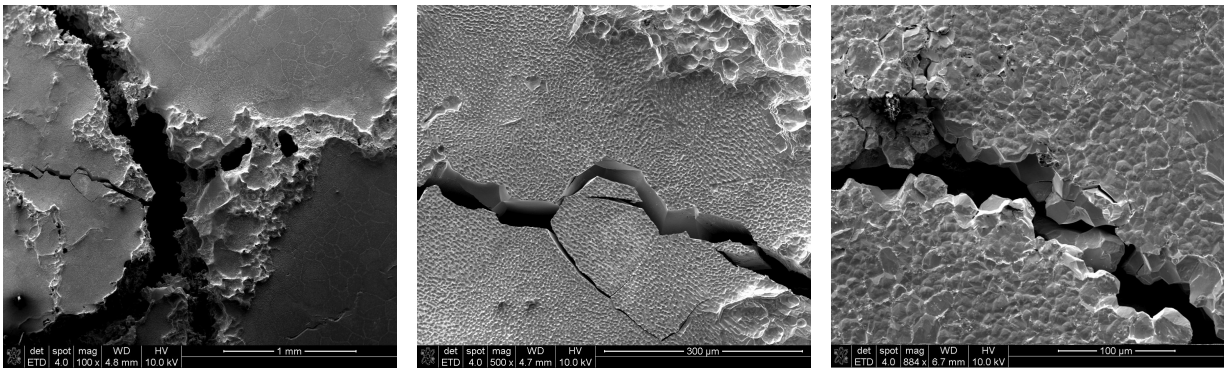

(a) (b) (c)

Figure 87: Post-exposure SEM images of D1 showing (a) cracks originating from the center of the sample, (b) brittle cracks and (c) inter-granular cracks.

7.5.2.2 The Influence of Material Self-constraint on Fracture

In order to study the effects of material self-constraint on thermo-fracture, we performed a series of experiments in which W disks were assembled using spring loaded clamps allowing free thermal expansion, as shown in Figure 67a. In these experiments, samples were placed 2.5 cm from arc-jet exit plane and were exposed to 10 cycles of 6s arc-jet on-time and 4s off-time while being continuously cooled from the back side by the cooling plate. Heat flux distribution at this distance from the arc-jet is shown in Figure 68b, which gives a maximum value of 24.4 MW/m^2 at the disk center. These tests were performed on 3.4 mm thick W disks with 2.5 cm and 5.1 cm diameters to study the influence of a colder material on the sample perimeter on constraining the central hot zone. Such conditions are also typical of laser or electron beam heating [46, 67]. Post-exposure optical images from these tests are shown in Figure 88. It can be seen that W disks with 5.1 cm diameter (D4 and D5) show significant damage and cracking compared to the 2.5 cm diameter disk (D3). Since these samples were assembled with spring loaded clamps, they experienced free thermal expansion during heat-up and the only constraint causing stress development is from the material itself. Having steep temperature gradients through the thickness (Figure 71c) during arc-jet on-time constrained the exposed face from free thermal expansion, resulting in compressive stress regimes. The exposed face of the W disk (T$\approx$ 2100 °C) experienced larger thermal expansion compared to the cooled face (T$\approx$ 1400 °C). In addition, due to the radial exponential decay in the arc-jet's heat flux, there is a radial temperature gradient on the exposed face of the sample as well (Figure 71b). In this case, the colder material on the perimeter, which has higher strength, prevents the central zone from free thermal expansion during heat-up and produces a compressive stress regime. This effect is more pronounced for larger diameter samples (D4 and D5) due to the steeper radial temperature gradients on their exposed face.

Having compressive stress on the exposed face center due to both radial and through thickness temperature gradients, and the reduced yield strength at elevated temperatures, caused this region to experience compressive plasticity during heat-up, as show in Figures 74b and 76b. The compressive strain developed during heat-up introduced tensile residual

stresses on exposed face center (Figures 75a and 77a) upon cool-down initiating and propagating cracks in this area as shown in Figure 88. D3 (2.5 cm diameter, 3.4 mm thickness) showed only micro-cracks (no large cracks) due to the smaller radial temperature gradient compared to D4 and D5 (5.1 cm diameter, 3.4 mm thickness). The FIB cross section on the exposed face of D4 acted as crack initiation site for the 4 observed large cracks. However, crack initiation was more random in sample D5, which had no FIB cut on its surface. Cracks in D4 and D5 were through-thickness, and propagated all the way to the cooled face of these samples.

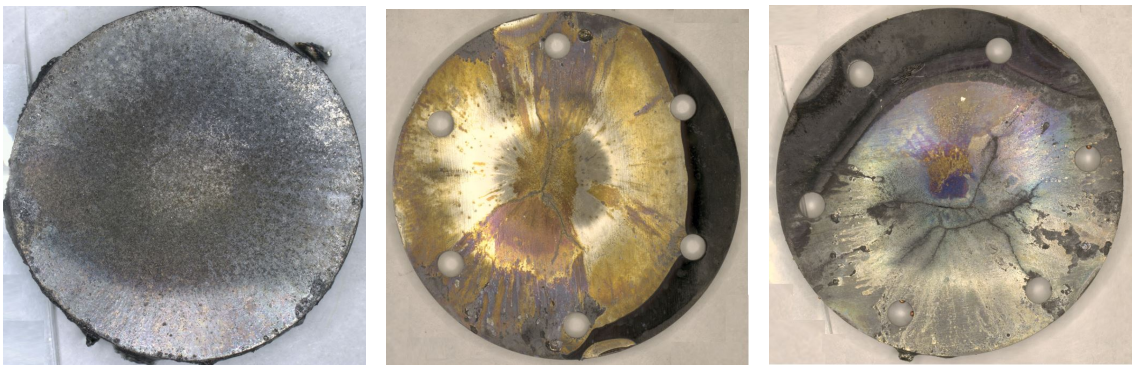

(a) (b) (c)

Figure 88: Optical images of the post-exposure faces of (a) D3 (2.5 cm diameter, 3.4 mm thickness), (b) D4 (5.1 cm diameter, 3.4 mm thickness) and (c) D5 (5.1 cm diameter, 3.4 mm thickness). These samples were thermally loaded with 10 cycles of 6s arc-jet on-time and 4s off-time at 2.5 cm from arc-jet under free thermal expansion conditions (assembled using spring loaded clamps as shown in Figure 67a).

To better illustrate the differences between fracture damage on the smaller diameter disk (D3) and the larger diameter ones (D4 and D5), we determined the frequency distribution of crack-COD and crack-length. The histograms of crack statistics are shown in Figure 89. It can be seen that W disks with larger diameters (D4 and D5) showed larger COD compared to D3. Also, D4 and D5 developed more cracks compared to D3 (Figure 89b). This is due to the greater radial temperature gradients on samples with larger diameters, which provide colder material on the perimeter to constrain the central hot zone. This results in larger compressive plastic strain during heat-up and the development of greater residual stresses during cool-down.

The experimental results presented here can be explained by the computer simulations discussed in section (7.4.2.2). Comparing the two cases simulated in section 7.4.2.2, it can be seen that the tensile stress at the center of the exposed face upon cool-down is much higher in Case II, where the cooled face of the W disk is constrained from out of plane displacement. This explains the extensive damage observed in samples D4 and D5 (Figures 88b and 88c). If one takes simple estimates for the maximum stress as 800 MPa (Case II, Figure 77a) at the central zone of the top face and the fracture toughness of tungsten as ≈ 5-10 MPa$\sqrt{m}$ [26] at room temperature, the critical crack size that will propagate at the end of cool-down is ≈ 12-50 μm. D4 had the 80 μm FIB cut on its exposed face center, which perfectly suited this condition. Also, such small flaws most likely existed in the other sample (D5), and thus one would expect fracture at the center of exposed face near the end of the cool-down phase of the thermal loading, as shown in Figures 88b and 88c.

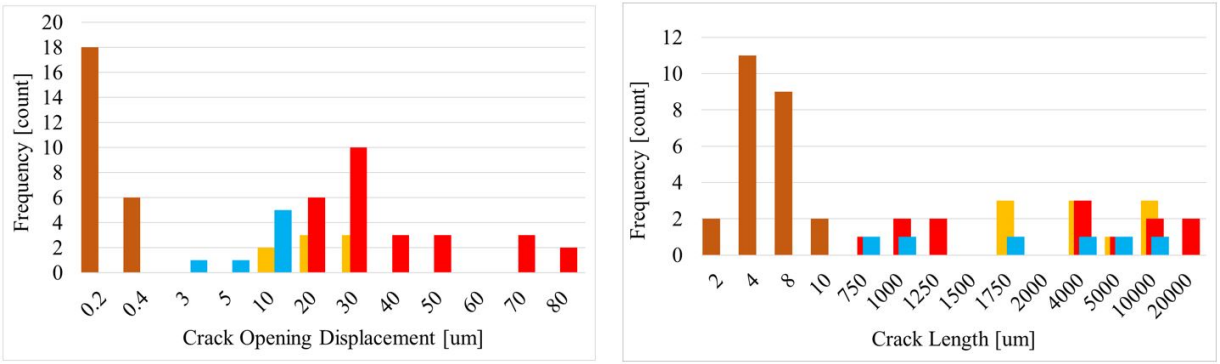

(a) (b)

Figure 89: (a) Frequency of COD and (b) crack length in samples: D3, D4, D5 and D7. The blue color represents D3, orange for D4, red for D5 and brown for D7 (sample D8 is not included in the histograms because it showed lack of cracks). All these samples are 3.4 mm thick and were loaded at 2.5 cm from the plasma arc-jet (q''_{max}=24.4 MW/m^2) for 10 cycles of 6s on-time and 4s off-time. D7 and D8 were fully constrained using 6 bolts, which provided better surface contact with the cooling plate (better cooling) and greater compressive stress state on the exposed face during heat-up due to fully constrained condition (bolted).

7.5.2.3 Thermomechanical Behavior of Fully-Constrained W disks

The influence of external constraints was explored by performing several tests where we fixed W disks on the CuCrZr cooling plate using 6 bolts (Figure 67b) to prevent free thermal ex-

pansion during heat-up. Samples D7 and D8 (5.1 cm diameter and 3.4 mm thickness) were tested under these boundary conditions at 2.54 cm (q''_{max} =24.4 MW/m^2) from the plasma arc-jet exit plane for 10 cycles of 6s arc-jet on-time and 4s off-time. The heat flux on the exposed face of these samples is shown in Figure 68b. Experimental temperature measurements at the center and edge of the sample's cooled face for one thermal cycle (6s on-time and 4s off-time) is shown in Figure 69a, using measured temperature as a time-dependent boundary condition. In these tests, bolting the samples to the cooling plate provided better surface contact and more effective cooling. This kept samples temperature below recrystallization, as shown in Figure 69a. Having lower temperatures and a compressive stress state on the sample's exposed face due to fixed boundary conditions prevented grain growth in D7 and D8 compared to samples tested with spring loaded clamps (D4 and D5). This seems to be consistent with observations on stress effects on recrystallization of Mo, where compressive stresses effectively suppress grain growth [68]. Figure 90 compares the damage in D4 with D7. It can be seen that in D4 grain growth was a cause of cracking. However, in D7 the lower temperature and compressive stress state prevented grain growth, which reduced the crack formation and thermomechanical damage significantly. The damage in these samples is quantified by comparing crack COD/length histograms shown in Figure 89. The COD and crack length distributions observed in D7 are significantly smaller than the ones in D4 and D5. Sample D8 did not show any cracks.

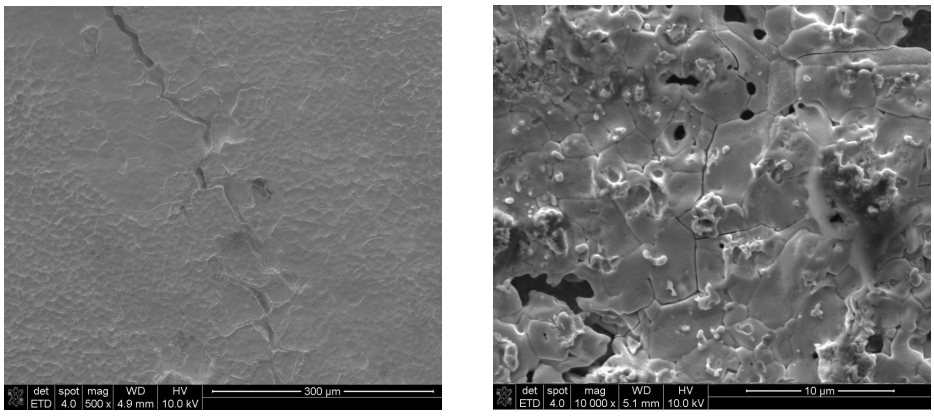

(a) (b)

Figure 90: Post exposure SEM images of (a) D4 showing larger grains adjacent to the crack, and (b) D7 showing smaller cracks and no grain growth due to the lower temperature and compressive stress state.

7.5.2.4 Comparison Between W-Foam and Solid W

In a previous study by [60], we showed that 43 % dense W foams are more resilient to cyclic high heat flux loading compared to the lower and higher density grades (23 % and 53 %). Therefore, W-foam samples in this work were all chosen to be 43 % dense with 3.6 mm thickness and 2 cm diameter. Samples were braised to 2.3 mm thick W substrates with a 2.5 cm diameter. Samples F1 and F2 have 80 PPI while F3 has 65 PPI. Samples were assembled using 4 clamps for perfect contact between the W-substrate and the cooling plate (Figure 67c). The samples were placed at a distance of 3.8 cm from arc-jet exit (q''_{max} =16.1 MW/m^2) and were thermally loaded with 10 cycles of 6s arc-jet on-time and 4s off-time. D6 (solid W disk with 3.4 mm thickness and 5.1 cm diameter) was loaded under same distance to the gun and the same loading schedule. Sample D6 was assembled on the cooling plate using 4 spring-loaded clamps (Figure 67a) to allow free thermal expansion similar to the foam on its substrate.

Post exposure SEM analysis showed no cracking on the W foam samples F2 and F3. However, F1 and D6 developed cracks after arc-jet exposure. The frequency distributions of cracks are presented quantitatively in Figure 91. Comparing the COD and crack length in F1 and D6, one can see that the COD of solid tungsten is approximately twice as large as W-foam F1 (Figure 91a). However, the crack length distribution and network pattern (Figure 91b) are similar. This suggests that under the same heat flux, solid W and W-foam develop similar network of cracks dictated by the surface temperature gradient. However, the COD distribution, which is a measure of stress relaxation, is much larger in solid W as compared to W-foam. In order to better understand the experimental results presented here, we performed detailed FE analysis and included the results in section 7.4.4. It can be seen from Figure 81 that the maximum tensile stress exceeds the yield strength at the center of the exposed face, consistent with the observed micro-cracks in (Figure 92b). Also, tensile stresses with magnitude of $\approx$ 150 [MPa] are predicted at the interface between the foam sample and its substrate, which can cause brazing failure at these areas, as was observed in some of our tests. Even though we see $\approx$ 360 [MPa] tensile stress on the cooled face of

the substrate during heat up (Figure 80a), this stress is not high enough to cause plasticity, as shown in figure 80b. It is also not high enough to initiate or propagate any cracks on the substrate considering the tungsten's higher fracture toughness during heat-up. The fracture toughness of W is $\approx$ 20 MPa$\sqrt{m}$ at 520 °C (substrate cooled face temperature during heat-up). Thus, to initiate crack propagation, a pre-existing flaw size of $\approx$ 980 μm is required on the substrate to fracture under 360 [Mpa]. A flaw size of nearly 1 mm was never observed in our pre-exposure characterisation. This was also confirmed in our post-exposure characterisation, showing the absence of cracks on the cooled face of the substrate.

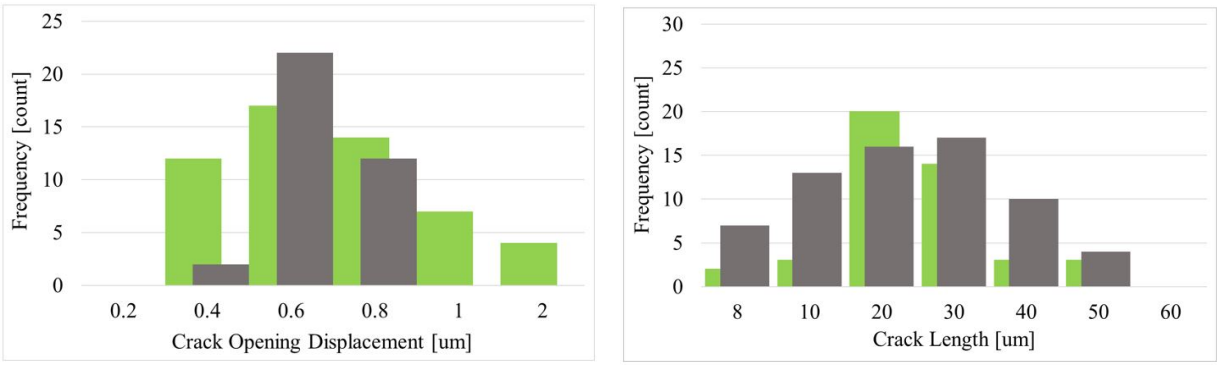

(a) (b)

Figure 91: Frequency distributions of (a) the COD and (b) crack length in D6 shown in green and F1 in gray. It is clear that F1 (W-foam) showed smaller COD compared to solid D6 but they developed similar crack network with alike crack lengths under same heat flux (foam samples F2 and F3 are not included in the histograms because they showed no cracks).

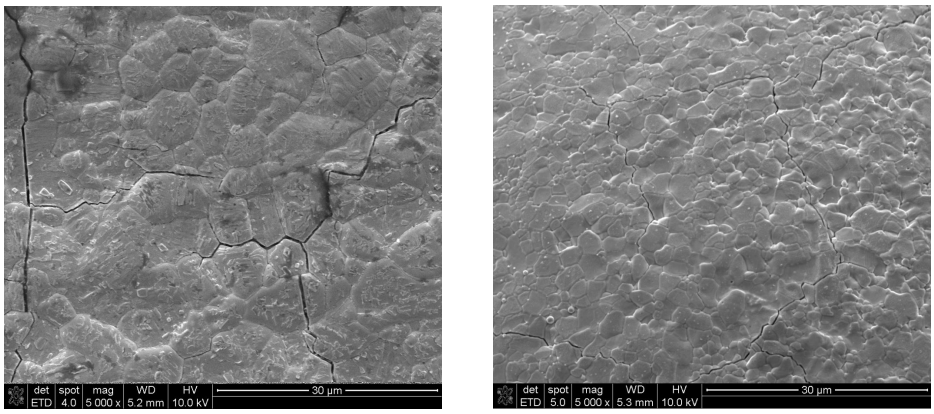

(a) (b)

Figure 92: Post-exposure SEM images showing inter-granular and trans-granular cracks in (a) D6 (solid W) and (b) F1 (W-foam), which were thermally loaded at 3.8 cm from the plasma arc-jet (q''_{max} =16.1 MW/m^2) for 10 cycles of 6s on-time and 4s off-time. It can be seen that COD is much bigger in D6 compare to F1.

Typical cracks from D6 and F1 are presented in Figure 92 showing both inter-granular and trans-granular cracks. It can be seen that COD is significantly larger in solid tungsten (D6) compared to the porous sample (F1).

7.5.3 The Effects of High Power Laser

The thermal shock behavior of W foam was evaluated at Forschungszentrum Jülich (Germany) via laser heating at the High Temperature Materials Laboratory in the linear plasma device PSI-2. The facility features a steady-state D, He, or Ar plasma, with column diameter of 60 mm, ion flux $\leq 10^{23}$ m^{-2}s^{-1}, and incident ion energy (bias) 10 – 300 eV. ELM-like heat pulse conditions can be generated with Nd:YAG laser of wavelength 1064 nm, and laser energy of 32 J. The following tungsten foam specimens were fabricated for testing:

1. Four samples, 23% dense, 80-PPI W foam, 10×12×4.2 mm (±0.2 mm on all dimensions).

2. Four samples, 43% dense, 80-PPI W foam, 10×12×4.2 mm (±0.2 mm on all dimensions).

Testing was performed under standard conditions, including different power densities,

base temperatures, and pulse numbers. All these conditions have been established by Forschungszentrum Jülich in other projects in order to compare the performance of different W products as plasma-facing materials [67]. The tests provide a good indication of the damage evolution to be expected during the operation of fusion devices like ITER and DEMO. The linear plasma device PSI-2 used to test the samples is described in reference [46].

Low pulse number thermal shock tests were performed on 80-PPI 23% dense tungsten foam and 80-PPI 43% dense tungsten foam, under the following conditions: base temperature =1000 °C, the number of pulses: 100 and 1000 pulses of $\Delta t = 1$ ms, power density = 0.19 and 0.38 GW/m^2, and the melting event: 1 pulse at 1.6 GW/m^2 for 2 ms. High pulse number thermal shock tests were performed on 80-PPI 23% dense W foam and 80-PPI 43% dense W foam under the following conditions: base temperature =700 °C, the number of pulses: 10k and 100k pulses of $\Delta t = 0.5$ ms, and power density= 0.19 and 0.38 GW/m^2.

For the low pulse number tests, the 1000 °C base temperature was selected to represent the high temperature regime for W PFCs. Absorbed power densities of 0.19 and 0.38 GW/m^2 (electron absorption coefficient of 0.55) were selected to represent levels that are above and below the expected damage threshold of pure W with an ELM-like pulse duration of 1 ms. Applying 100 pulses helps to determine the general damage behavior and 1000 pulses at the higher power density addresses the influence of thermal fatigue and helps quantify damage evolution. The conditions for the melting event were selected to be representative of a transient event (type I ELM).

For the high pulse number tests, the 700 °C base temperature was selected to represent the ductile temperature regime for W PFCs. Absorbed power densities of 0.19 and 0.38 GW/m^2 were again selected to represent levels that are above and below the expected damage threshold of pure W. Testing to high pulse numbers generally increases the risk of surface erosion and localized melting and the 10k and 100k pulse levels were selected to evaluate that behavior.

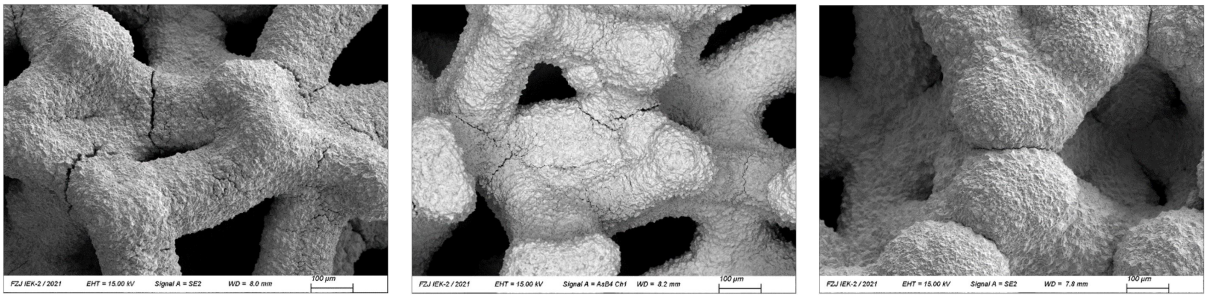

(a) (b) (c)

Figure 93: Laser heating post-exposure SEM images showing cracks in (a) 80 PPI 23 % W foam thermally loaded at 0.19 GW/m^2 power density with 10k pulses, (b) 80 PPI 23 % W foam thermally loaded at 0.38 GW/m^2 power density with 100k pulses and (c) 80 PPI 43 % W foam thermally loaded at 0.19 GW/m^2 power density with 10k pulses.

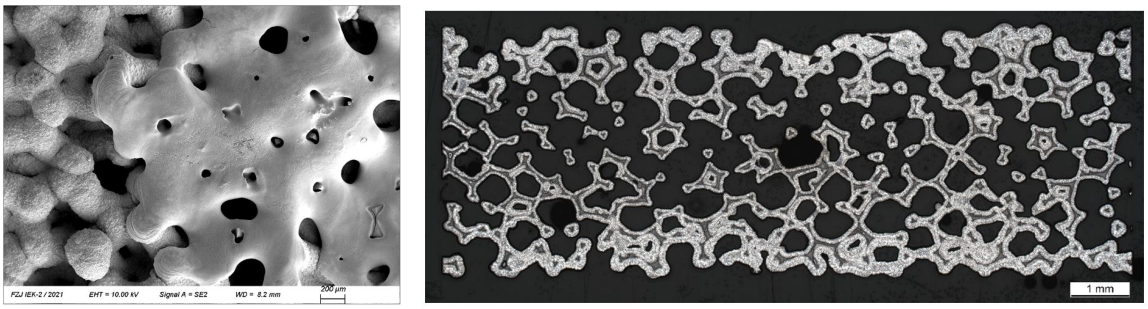

(a) (b)

Figure 94: SEM images of the 80 PPI 43% W foam melt event with laser at 1.6 GW/m^2 for 2 ms showing (a) the W foam exposed face and (b) cross section.

The tests indicated that under low pulse thermal shock test conditions, no visible damage was formed at 0.19 GW/m^2 and 0.38 GW/m^2 for both samples (23 % and 43 %). Small droplets of molten material were originated from already loose parts. The 43% dense sample showed small particles after exposure to a heat flux of 0.38 GW/m^2. EDX analysis showed that traces of Ca and O were found from an unknown origin, and that the density of the particles seems to increase with increasing number of thermal shock events (100$\longrightarrow$ 1000 pulses). The molten surface appeared to be similar for both 23 % and 43 % dense foams and seems not to depend on the volume fraction of the foam.

Cross sections of the samples showed a reduced density in the center of both materials but no loss of molten material or cracks. The molten layer seems to be very stable. Small

cracks are observed for both materials after 10k pulses at 0.19 GW/m^2, and in the material with lower density (23%) after 100k at 0.38 GW/m^2. In high pulse thermal shock tests the 23 % dense foam showed cracks under both testing conditions: A) 0.19 GW/m^2 power density with 10K pulses and B) 0.38 GW/m^2 power density with 100K pulses. The foam with 43 % volume fraction showed cracks under testing condition (A) and no cracking for testing condition (B).

It is concluded that the tungsten foam specimens performed well in terms of damage resistance following low pulse number thermal shock testing when compared to other tungsten products tested in previous work, such as pure tungsten grade IGP manufactured by Plansee SE (Austria) according to the ITER material specifications. Compared to tungsten foams, the IGP tungsten material exhibited much more extensive crack formation and propagation. Tungsten foam performance during high pulse number testing was also determined to be good compared to that seen for other tungsten materials.

7.6 Conclusions

In this comprehensive study of the thermomechanics of tungsten under intense cyclic heating, we utilized computational modeling and post-experiment material characterization to unravel the mechanisms of fracture and thermal damage in solid W, and to understand the extent by which such mechanisms operate in open-cell W foam. The study showed the differences between external and self-constraint effects on the fracture process. Variations of the external boundary conditions allowed separation of bending and in-plane deformation modes, and an understanding of the sources of crack formation associated with these modes. The porous, truss-like geometry of the W-foam samples was shown to accommodate greater thermal strains than solid counterparts through ligament rotation and micro-cracking, without the propagation of catastrophic through-thickness cracks. The comparative study of thermal shock of W foam at extreme power (GW/m^2)/ short duration (ms) and high-power (MW/m^2)/ long duration (seconds) indicated that the nature of thermo-fracture damage is similar in both cases, and that the damage is manifest through distributed micro-cracks

rather than destructive macro-cracks.

The following is concluded from the study:

1. Under extreme thermal *local* loading, W exhibits a self-constraint effect, developing cracks in the central hot zone. These cracks are a result of the accumulation of compressive plastic strain during heat-up, followed by elastic release of residual tensile stresses upon cool-down. This is illustrated by tests performed on D3, D4 and D5, where the diameter of D3 was half of D4 and D5 and showed less cracking. All of these samples were tested under free thermal expansion conditions where samples were mounted with spring loaded clamps to accommodate thermal expansion. However, they still developed cracks as a result of the *self-constraint effect*.

2. W disks tested with a free expansion boundary conditions (D4 and D5) developed more cracks compare to the bolted configuration (D7 and D8). This seems to be surprising at first glance. However, SEM images showed grain growth adjacent to cracks in free W disks, which resulted in crack initiation and propagation. Such samples received less cooling through the cooling plate compare to bolted samples. Less thermal contact with the cooling plate of free samples increased the exposed face temperature, thus enhancing the grain growth. On the other hand, grain growth was not observed in bolted W disks due to lower temperatures and the compressive stress state induced by thermal strains during heat-up.

3. W-foam and solid W were directly compared with each other via tests performed on foam samples F1, F2 and F3 and solid W D6 under similar loading and boundary conditions. F2 and F3 showed no cracks and F1 showed smaller COD compared to D6 (Figures 91a and 92). This is indicative of the resilience of the W-foam structure, which accommodates thermal strains by a combination of geometric rotations of ligaments and distributed micro-cracking.

4. Orientation-dependent and preferential etching under plasma was observed on most of the samples especially on D1 showing etched grain boundaries (Figure 84) and enabled

a study of the effects of heat flux and temperature on grain growth and distribution.

5. Trans-granular and inter-granular cracks were observed in both W disk (D6) and W foam (F1), as shown in Figure 92. However, most observed cracks are inter-granular, as shown in Figures 87c for D1 and 90a for D4.

6. Ductile carks are observed at the center of samples (center of loading) and become brittle on the edge, as shown for D1 in Figures 86a, 87a and 87b.

7. It can be seen from Table 2 that all the W disks that recrystallized displayed cracks, except for D2 which was thin enough to accommodate the thermal strain by out of plane deformation with no cracking.

8. The two thick bolted samples (D7 and D8) did not recrystallize due to better surface contact to the cooling plate through the experiment reducing the exposed face temperature (the thin bolted samples D1 and D2 deformed out of plane losing their surface contact with the cooling plate, increasing the exposed face temperature and recrystallizing). Also, extensive compressive stress state on the exposed face of thick bolted samples during heat up prevented recrystallization and grain growth on these samples reducing cracking in D7 and preventing it in D8.

9. All three foam samples tested in this work displayed recrystallization. However, only one sample showed cracks (F1) and the observed COD were much smaller compared to D6, which was tested under the same conditions. Recrystallization and grain growth can cause migration of impurities to grain boundaries weakening them and leading to crack formation and propagation in solid tungsten. However, W foams fabricated with the CVD process are very pure, and have a much finer grain structure in the as-fabricated condition. It can be seen that unlike solid W, porous tungsten (W foams F2 and F3) does not necessarily develop cracks after recrystallization due to the slower rates of grain growth, the high purity of W, and the flexible geometry.

10. HEFTY arc-jet testing of W foam samples that were exposed to a low-pressure helium plasma prior to HEFTY testing, showed that these samples lost the nano-features (W-

fuzz) on their surfaces. Helium plasma exposure did not result in thermomechanical fracture or damage.

11. High power laser testing of W-foam samples demonstrated that under low pulse (100-1000 pulses) thermal shock test conditions, no visible damage was formed at power levels of 0.19 GW/m^2 and 0.38 GW/m^2. High pulse testing (10,000 - 100,000) showed that the nature of thermo-fracture in W-foam is similar to what was observed in HEFTY experiments, and that the thermal damage is rather distributed in small micro-cracks as opposed to catastrophic macro-cracks. Microscopic cracks were observed after 10,000 pulses at 0.19 GW/m^2 in both low and high density foams (23% and 43%), and in the low density foam after 100,000 at 0.38 GW/m^2.

CHAPTER 8

Dimensional Stability of Large Fusion Energy Structures

8.1 Introduction

Concrete steps in the realization of practical fusion energy are being taken, as demonstrated by the design and construction of large-scale fusion devices. While the International Thermonuclear Experimental Reactor (ITER) is under construction in France, design efforts are underway in various countries for the next steps. ITER is expected to produce 500 megawatts (MW) of thermal output power for 6-8 minutes, with 50 MW of thermal power injected into the tokamak (power gain Q=10, without electricity production). First plasma operation is scheduled in December 2025. The United States is pursuing a two-step facility approach in preparation for post-ITER fusion power production. First, a conceptual design of a Fusion Nuclear Science Facility (FNSF) has been completed [69] and is now being updated. Furthermore, there is significant interest from the scientific community in the development of a "Compact Fusion Pilot Plant (CFPP)" [70]. The FNSF is envisioned as a device where the fusion nuclear environment is experienced in its fully integrated form for the first time [69].

An overview of the FNSF reactor is shown in Figure 95. On the right side of the figure, a top view of the doughnut- shape tokamak is shown, and is composed of 16 sectors with details shown on the left side. The plasma (red) is surrounded by the first wall/ blanket structure (blue) that acts as an essential heat exchanger to transfer fusion energy to a thermal system outside the fusion core. The entire system is located inside a vacuum chamber, and is surrounded by 16 strong toroidal magnets (green). At the top and bottom of the plasma region, energetic plasma particles (helium, tritium, and deuterium ions) as well as photons

strike plates that must transfer deposited energy into the thermal system and added to what is transferred by the first wall/blanket (FW/B). The reactor is designed to have flexibility so as to accommodate a variety of testing and operational conditions [69]. In FNSF, the plasma current is 7.9 MA, the toroidal magnetic field at the plasma center is 7.5 T, the ratio of magnetic-to-plasma pressure is β= 2.4, the effective charge is Z_{eff}=2.4, the total fusion power is P_{fusion}=518 MW with a Q=4. The neutron energy flux is Nw=1.2 MW/m^2, and the peak surface heating flux on the divertor is q_{div}=10 MW/m^2.

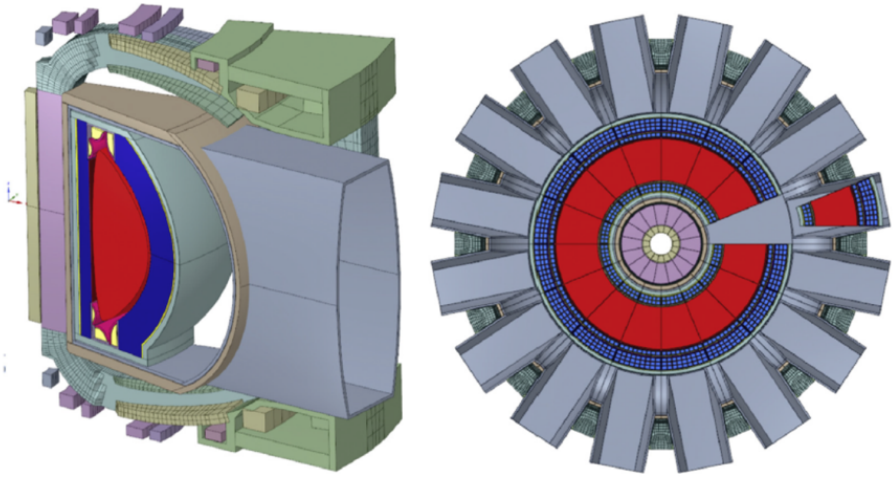

Figure 95: An overview of the Fusion Nuclear Science Facility (FNSF) [69].

Ferritic/martensitic steels have been proposed as fusion structures for the past few decades, mainly because of their favorable response to neutron irradiation and their potential low-activation characteristics as compared to austenitic steels [71, 72]. Nearly four decades ago, [73] estimated the effects of neutron irradiation on the lifetime of a ferritic/martensitic steel structural FW/B. They used available data and simple design rules (such as limiting the volumetric swelling strain to 5%) to show that an operating design window exists for such structures. The lower temperature limit is dictated by the shift in the Ductile-to-Brittle-Transition Temperature (DBTT), while the upper temperature limit is dictated by creep strain accumulation and potential rupture. The structure lifetime in the intermediate temperature range is limited by volumetric swelling. This simple picture remained roughly the same during the past four decades, albeit lacking concrete and detailed justification.

Recently, the advent of High Performance Computing (HPC) has opened the door to more thorough investigations of the thermomechanical response of large fusion structures, such as magnet systems [74], FW/B[75, 76] and the Divertor [40]. However, in all these studies, the effects of neutron irradiation were not considered, and thus, the simple picture of the operational design window presented by [73] remained the same. The difficulties in improving on these early estimates of FW/B structural lifetime are two fold. First, the effects of neutron irradiation on material properties under relevant fusion conditions are non-existent because of the lack of prototypical irradiation facilities. And, second, the computational methods that allow for the incorporation of *constitutive equations* into thermomechanics simulations are rudimentary.

The objective of this work is to investigate the effects of neutron irradiation on stress and plastic strain evolution and dimensional stability of a large section of the FW/B module of the FNSF device. This will be accomplished by making progress on the two fronts that hampered more realistic estimations of component lifetime. We plan to utilize recently developed constitutive equations for the dependence of irradiation swelling on the neutron dose, operational temperature and helium generation rate [33]. We will also assess the effects of radiation hardening and softening [35] on the stress state and dimensional stability of the FW/B structure. The motivation of the study is to enable detailed understanding of the effects of neutron irradiation on life-limiting properties of the FW/B structure, particularly volumetric swelling and radiation hardening or softening. Lifetime evaluations of the effects of irradiation require such detail, and will be pursued in a separate future publication.

8.2 System Description

The design approach of FNSF is based on full-sector maintenance, where all components inside the vacuum vessel are contained within 16 steel structural rings between Toroidal Field (TF) coils, as shown in Figure 95. The breeding blanket is attached to these structural rings using sliding joints that allow for free expansion in the vertical direction. The major design characteristics of Dual Coolant Lead-Lithium (DCLL) blanket include helium flow

paths for cooling the first wall and blanket structures, and LiPb liquid metal paths for cooling all blanket regions. The radial length of the Inboard (IB) blanket is 50 cm, including a 3.8 cm thick First Wall (FW) with a 3 cm cooling channel, 1.8 cm Back Wall (BW) as well as the breeding zone. An alternating toroidal coolant flow configuration is used for the FW to create more uniform temperature. In addition, there are SiC Flow-Channel Inserts (FCI) placed in breeding zones, serving as both electrical and thermal insulators between the structure walls and LiPb. The CAD model in Figure 96 for the IB blanket represents one of a total of 16 blanket sectors at mid-plane, showing the breeding zones, SiC inserts, stiffening, separation and back plates with poloidal cooling channels. There are 4 radial stiffening plates connecting the FW and the BW to accommodate bending stresses. The separation or Intermediate Wall (IW) divides the blanket into two sets of breeding zones (Figure 96b). The cooling pathways for IW was modified from the toroidal direction to a poloidal direction, similar to the cooling pattern of the BW. Each breeding cell is about 19.6 cm in the radial direction. The FW structure is curved with a radius of 3.5 m. Detailed descriptions of the system can be found in references [69, 75], as illustrated by the cross-section of the FNSF machine shown in Figure 96a.

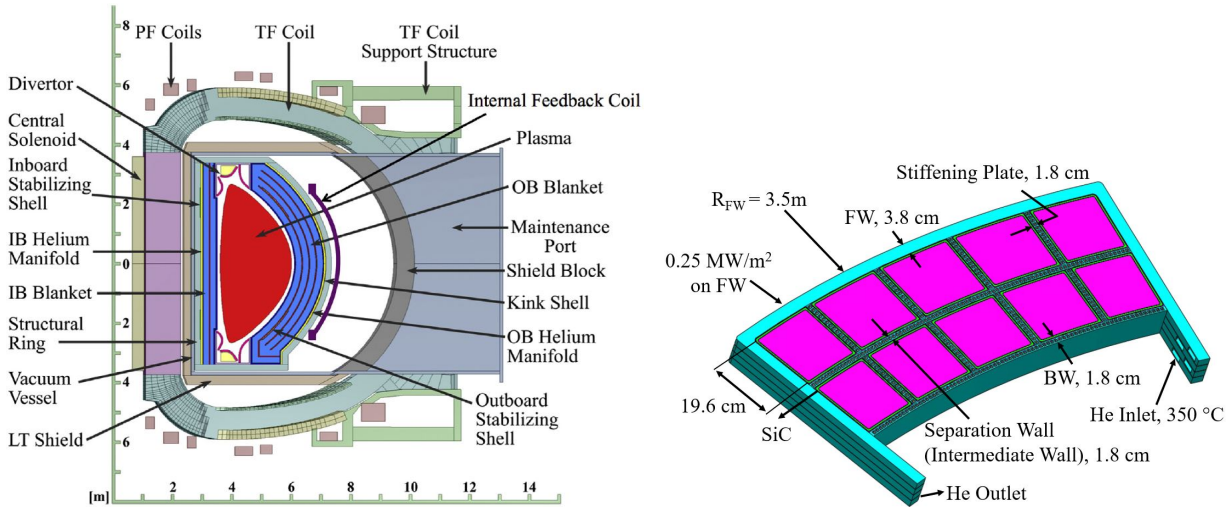

Figure 96: (a) Cross-sectional view of FNSF showing details of the FW/B system and how it fits inside the TF magnet system [69]. (b) FW/B structure showing significant dimensions and loading conditions

8.3 Heat Transfer and Temperature Distributions

8.3.1 Modeling

To determine the stress state and dimensional changes in this large section of the FW/B system, detailed temperature distributions throughout the structure are needed. To accomplish this task, the incident power and cooling mechanisms must be identified. The incident power resulting from fusion reactions within the plasma is two-fold: (1) a surface heat flux of 0.25 MW/m^2 as the combined heat load of photons and plasma ions on the FW; and (2) volumetric heat deposition due to the interaction between neutrons and various materials (both structures and coolant) within the FW/B system. The volumetric power deposited in the FW structure, SiC inserts and the LiPb breeder was determined through separate neutron transport calculations [77, 75].

Temperature distributions can be obtained in one of two possible ways. Detailed coupled heat transfer and fluid simulations can be used to calculate the energy exchange between the structure and the fluid (in this case, helium in the FW and LiPb in the breeder channels). A second approach is to rely on experimentally validated heat transfer correlations that give local heat transfer coefficients between the structure and the coolant, based only on bulk coolant properties. It is shown that using heat transfer correlations is sufficient for the required accuracy, if one accounts for differences between single-sided heating from the plasma and experimentally validated heat transfer coefficients, where the heat flux to tubes is usually applied from all sides [75]. Because of the enormous reduction in computational cost, we use common heat transfer correlations to determine temperature distributions everywhere in the FW/B structure, thus avoiding coupled Computational Fluid Dynamics (CFD) with heat transfer.

We model the heat transfer process in toroidal and poloidal channels with a convective heat flux boundary condition applied on the walls of these channels, starting with an initial guess for the average bulk temperature of helium between the inlet and outlet streams and the corresponding heat transfer coefficients. A Dittus-Boelter heat transfer correlation is used to obtain the heat transfer coefficients for both toroidal and poloidal helium cooling

channels, with an inlet velocity of 30 m/s for the toroidal channels and a total mass flow rate of 86 kg/s for poloidal channels in the 16 blanket sectors [75]. Since we are modeling one of these 16 sectors, the mass flow rate considered in poloidal channels for our study is 5.38 kg/s. In order to account for the heat transfer enhancements in toroidal channels due to internal fins, the toroidal heat transfer coefficient is increased by 50%. A MATLAB script is developed with 2-way communication with the finite element model to narrow down the initial guesses for average bulk temperatures in an iterative way. In this process, the temperature of the helium coolant at the toroidal channel inlet is assigned to be $350°C$ so as to avoid undesirable cooling of the structure below the DBTT for F82H [75]. The outlet temperatures of toroidal channels are calculated using an energy balance, considering all other applied heat sources. The computed outlet temperature is used to update the average bulk temperature and is used as the inlet temperature for poloidal channels. The same energy balance process is repeated to compute the outlet temperature of poloidal channels to update the average bulk temperature for these channels.

Liquid metal correlations are used to compute the heat transfer coefficient for LiPb in the breeder zone [75]. The calculated heat transfer coefficient is used as a layer conductance between the LiPb breeder and the SiC inserts in a thermal contact pair created between these two regions. Also, the LiPb breeder is treated as a working fluid carrying out heat from the system, moving with a velocity of 0.048 m/s (obtained from the inlet mass flow rate). The inlet temperature of LiPb in the first row of the breeder in our model is chosen to be 450°C, considering the 4 toroidal channels in our study as the very top layer in the IB blanket. Our current study is focused on the last 4 channels in IB blanket with the highest coolant temperature. Then average output temperature of the first row of breeder is used as the inlet temperature boundary condition for the second row. Temperature-dependent thermal properties (e.g. thermal conductivity, specific heat, and density) for F82H, Helium and LiPb are used in the FEM thermal model [3, 29, 75].

8.3.2 Temperature Distributions

Results of heat transfer simulations are shown in Figure 97. The maximum temperature in the breeder zone reaches to 460°C. The temperature of the F82H structure (Figure 97c) shows significant variation from a cool back end at 380°C to a maximum of 520°C on the first wall and 540°C on the first wall corners due to direct surface heating. These results reveal that heat transfer enhancement in FW channels should be adopted as part of the manufacturing process, as they are effective in providing enough cooling within the channels. Also, having LiPb as a moving working fluid is essential in keeping the temperature of the breeding zone (Figure 97a) at levels that are low enough not to result in excessive heating of the FW structure. The radial temperature distribution along the structure mid-plane is shown in Figure 98. It can be seen that FW temperature decreases from 520°C to 380°C inside He channels and gets to 454°C where it meets breeding zone and reduces again to 390°C and 385°C in intermediate and back wall He cooling channels. Figure 99 shows temperature distribution across SiC ceramic and its role in reducing heat flow from the breeding zone to He cooling channels in order to improve system effectiveness. Temperature distribution obtained on F82H structure (Figure 97c) is used in structural analysis to determine material properties as function of temperature in addition to using it for applied thermal loading.

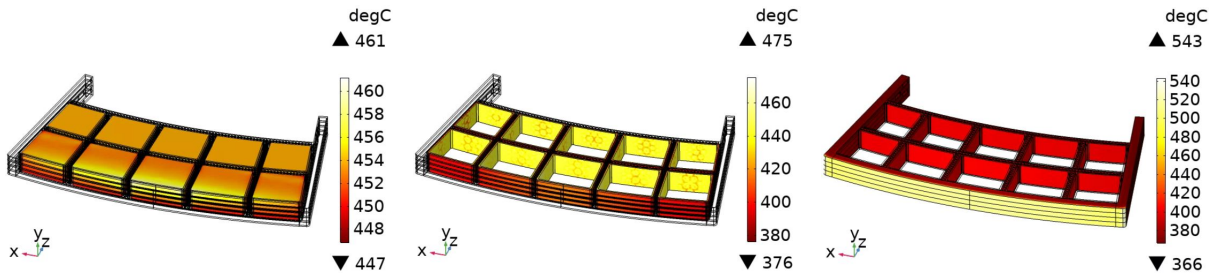

(a) (b) (c)

Figure 97: Temperature distribution of (a) LiPb breeding zone, (b) Sic ceramic and (c) FW/Blanket structure.

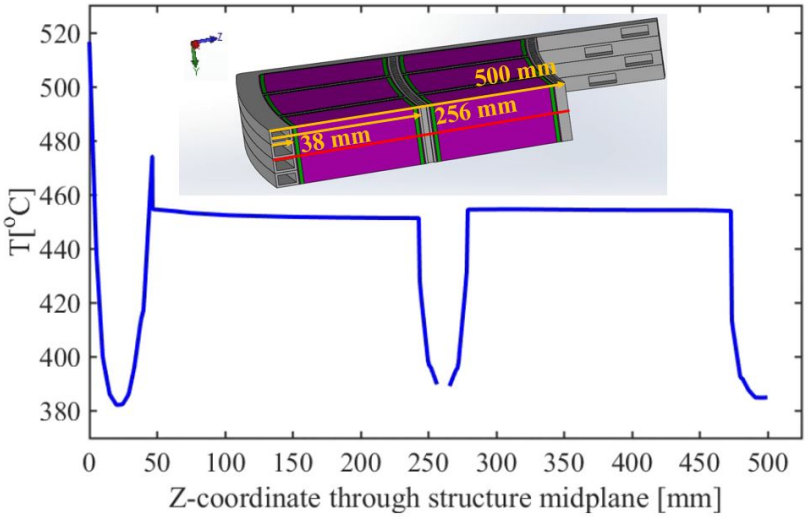

Figure 98: Temperature distribution along the radial direction (red line) shown in the structure's mid-plane, starting from the first wall and passing through He channels, stagnated LiPb, SiC ceramic FCI and the LiPb breeding zone.

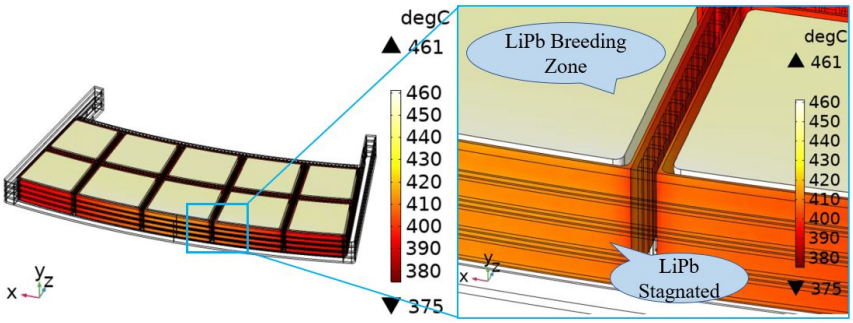

Figure 99: Temperature distribution across the SiC ceramic FCI, showing its effectiveness in reducing heat flow from the breeding zone to He cooling channels.

8.4 Solid Mechanics Modeling

8.4.1 Modeling Details & Boundary Conditions

Structural analysis is performed considering temperature and irradiation dependent material properties and the linear hardening plasticity model (Figure 27a) described in previous sections. We apply pressure loads, thermal loads due to the temperature distribution shown in Figure 97c, and include volumetric swelling effects shown in Figure 32. Pressure loading under normal operating condition is set to be 8 MPa in toroidal and poloidal cooling chan-

nels and 1.6 MPa in LiPb breeding zone. Symmetry boundary conditions are applied to the blanket allowing normal displacement on the top face considering free thermal expansion in the poloidal direction and no displacement in the normal direction to the bottom face to prevent free body motion. Also, roller conditions are applied at the end of the manifold, as shown in Figure 100a to prevent free body motion in the other two directions.

To examine the effects of radiation on the assembly/disassembly and maintenance of FW/B modules, we carry out structural analyses for two limiting cases. First, free side walls are considered, allowing free displacement normal to their plane due to thermal expansion and radiation induced swelling. This represent the case where IB blanket sectors are assembled in a way that allows enough room between them to accumulate any kind of deformations during service. Second, we consider the other limiting case of constrained side walls, where any displacement in the normal direction to the side walls plane is prevented. This case shows the extent of deformation mode change due to module constraints and the corresponding influence of the strain and stress distributions. Comparing the results obtained from these two case studies can help to identify a reasonable spacing between IB blanket sectors which will close up during heat up and swelling without building up huge stresses during service and will allow their easy replacement at the end of lifetime. This may have serious design implications on the tritium breeding ratio due to neutron streaming in between module gaps.

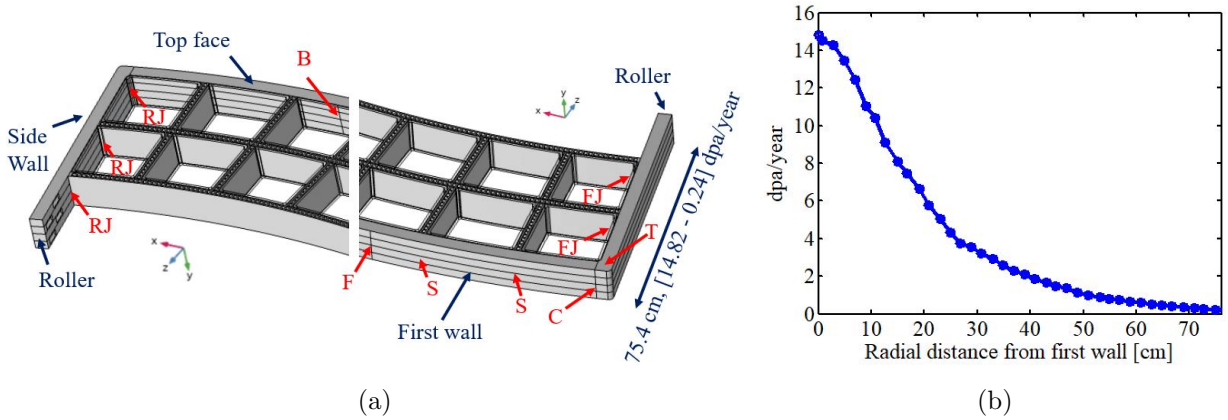

(a) (b)

Figure 100: (a) Cross-section of the inboard blanket CAD model. (b) Irradiation damage dose (dpa/year) along the radial distance from the FW [78].

Previous studies of radiation effects on FW/B structures were based on simple general limits of the magnitude of accumulated swelling strain at the FW of a few percent. In this study, we examine for the first time the influence of spatial gradients in radiation damage parameters (i.e. neutron dose and helium generation rate) on the deformation and stress evolution of the FW/B structure. To understand the complex ways by which deformation and stresses are distributed in spatially-varying radiation field, we will examine two cases. The first one is a reference case, where the radiation damage parameters at the FW/B are assumed to be the same regardless of spatial position. The second case is when radiation damage parameters are introduced in the structural model with their real space dependence. Irradiation damage dose (dpa/year) is maximum at the FW and decreases as the radial distance from the first wall increases as shown in Figure 100b. Space-dependent irradiation can affect the stress level and deformation mode and magnitude due to the gradual change in material properties and volumetric swelling from region to region. To enable consistent comparisons, we label seven distinct zones in the FW/B, as shown in Figure 100a and described in table 3.

Table 3: Distinct zones in the FW/B shown in Figure 100a

Region	Definition
F	Plasma-facing FW mid-plane
C	Plasma-facing FW corners
T	FW top and bottom corners
B	FW mid-plane facing LiPb breeder
S	Plasma-facing FW joints with radial stiffening ribs
FJ	Front joints between BW/IW and side walls
RJ	Rear joints between FW, BW & IW and side walls

8.4.2 Thermomechanical Stress and Deformation at BOL

Structural analysis at Beginning-Of-Life (BOL) does not include any irradiation effects, and is simply done by applying thermal and pressure loading onto the FW/B structure. We

performed BOL studies for the free and constrained side walls cases.

(i) Free side walls:

Allowing the side walls (Figure 100a) to freely expand under thermal and pressure loading introduces global mechanical displacements of the structure, as shown in Figure 101a. Note that the maximum displacement is ≈ 4 mm, and occurs at the FW corners (region C). Having free thermal expansion of the side walls reduces the stress level on structure, and results in negligible plastic strain of 0.004% at first wall region S and 0.02% at regions C, as shown in Figure 103a. The Von-Mises stress reaches its maximum of 397 MPa at the FW regions S and C (Figure 102a). Although the stress level and effective plastic strain in the overall structure is reasonable, the magnitude of free expansion and deformation of the side walls may not be allowable in IB assemblies considering the tight tolerances required for FW/B module assembly.

(ii) Constrained side walls:

When the side walls (Figure 100a) are constrained from displacement in the normal direction to allow precise alignment of FW/B modules during initial assembly, one would be concerned about the accommodation of both thermal and radiation-induced expansion of the large modules. This changes the displacement mode of the FW to be more like a bending type compared to the general volumetric expansion when the side walls are not-constrained. This can be seen by comparing Figure 101a to Figure 101b. Having this level of bending, requires detailed fracture analysis of the FW, IW and BW to prevent potential crack opening and propagation under large displacements. Another major concern is the mid-plane displacement of the FW (region F), which reaches a maximum of 18.4 mm at BOL. Such large displacement into the plasma scrape-off layer may be an important design concern that needs further analysis.

The Mises stress distribution shown in Figure 102b, indicates high stress concentrations in regions C, FJ, RJ, and T reaching to a maximum of 518 MPa. Such high stress levels result in significant plastic strain up to 3% in these regions (Figure 103b). This suggests that detailed cyclic plasticity analysis during startup/shutdown or pulsed operation on

these regions must be performed so as to estimate the accumulated plastic strain in strain-based life-time predictions. Also, it can be seen from Figure 102b that the stress at the middle of FW front face (region F) is lower than its back face (region B), even though the front face is at higher temperature. This is due to combination of bending and thermal stresses at first wall. Both faces of the FW experience compressive stresses due to constrained thermal expansion. However, the bending stress is tensile on the front face and compressive on the back face of the FW. This increases the magnitude of stress on the back face (region B) and lowers it on front face (region F). This trend is not observed in the free case (Figure 102a), where there is no bending effects. Constraining the side walls and introducing the bending-type stress state reduces the stress at the mid-plane of FW front face (region F) and increases the stress at the FW mid-plane back face (region B), as it can be seen by comparing 102b to 102a.

Comparing free and constrained side wall studies it can be seen that constraining side walls introduces large stress concentration at corners where FW, IW and BW join radial stiffening ribs and side walls specially at regions C, FJ and RJ. Design optimizations can be performed to prescribe certain displacement on side walls to allow enough bending deformation to balance the stress level from front to back face of FW. Even-though the stress state is mostly compressive on both faces of FW the build up residual stress at regions with high plasticity (regions C and FJ) will go under tensile stress during cool down and can cause crack initiation and propagation in these regions. It is noted that during the heat-up phase of operation, regions RJ will be under high tensile stresses, which can cause crack propagation and failure. On the other hand, regions C and FJ will be under high compressive stresses that can lead to large plastic strain and tensile residual stresses upon cool-down. These potential failure modes will be analyzed in a follow-up future publication.

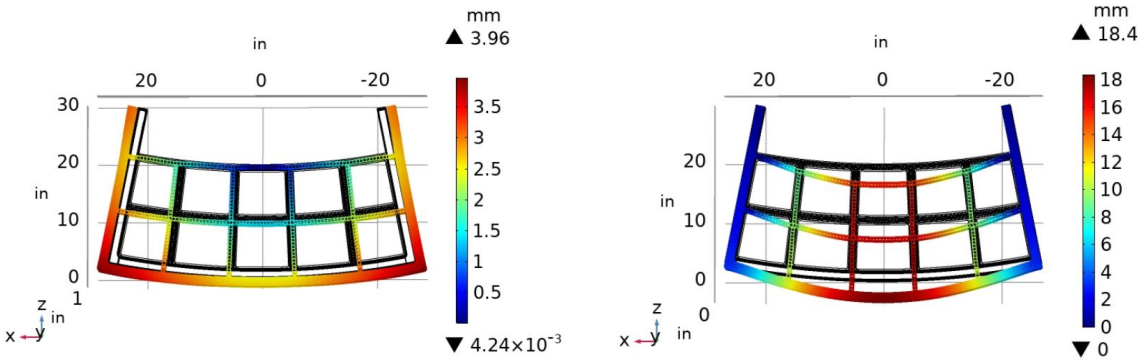

(a) (b)

Figure 101: Displacement results at BOL under (a) free side walls (scale factor 15) and (b) constrained side walls (scale factor 5).

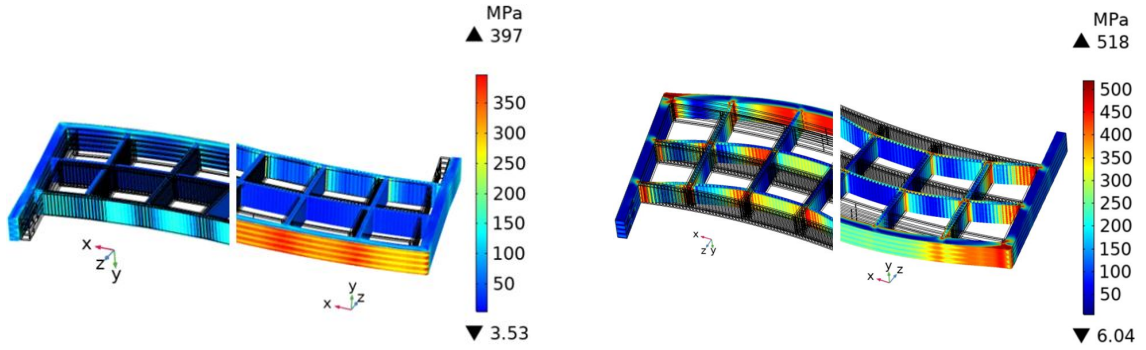

(a) (b)

Figure 102: Front and back view of stress distribution at BOL under (a) free side walls and (b) constrained side walls.

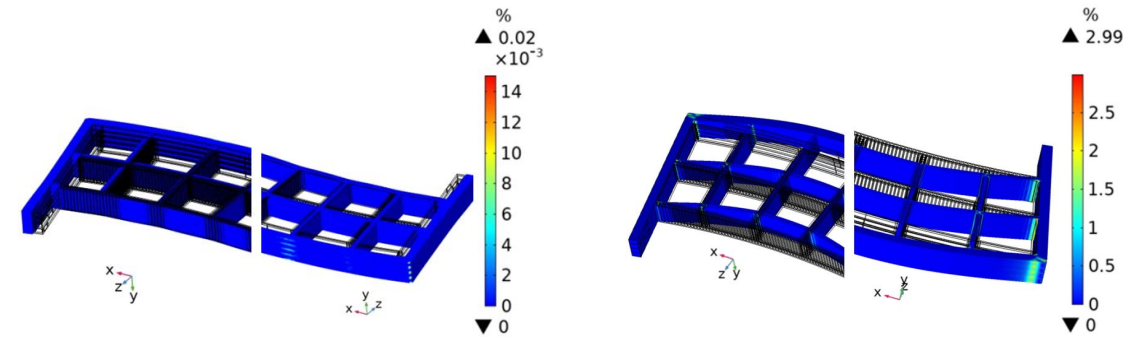

(a) (b)

Figure 103: Front and back view of effective plastic strain at BOL under (a) free side walls and (b) constrained side walls.

8.4.3 Reference Study of Uniform Irradiation Field

Let's first consider here a reference case, where the irradiation field is assumed to be the same as that experienced by the FW. Despite the conceptual nature of this reference case, understanding the dimensional stability and stress evolution under irradiation here will allow us to clearly determine the unique influence of spatial gradients in radiation damage parameters. The following results of computer simulations are given for a neutron displacement damage dose of 45 and 90 dpa, representing 3 and 6 years of continuous operation. The upper limit of 90 dpa is modest, since one of the goals of structural material development is to make it radiation-resistant up to $\approx$ 200 dpa. The influence of spatially-varying temperature on the yield strength, ultimate strength, tangent modulus and volumetric swelling is included. As can be seen in Figures 29a, 29b, 27b and 32 σ_y, σ_u, E_t and f_v are functions of temperature at any chosen dpa. The uniform irradiation simulations are performed on the two cases mentioned before to see the effects of boundary conditions and constraints.

(i) Free side walls (45 and 90 dpa):

In this study, the side walls are free to deform under irradiation-induced volumetric swelling and thermal expansion. As the neutron dose increases, the magnitude of volumetric swelling also increases causing continuing mechanical displacement and deformation of the entire FW/B structure. When we compare Figures 101a and 104, it can be seen that maximum displacement at the FW/B corners reaches $\approx$ 5 mm at 45 dpa and 9.5 mm at 90 dpa. Note that the maximum displacement at BOL was only 4 mm. Also, it can be seen that the global volumetric growth mode observed at BOL for free side walls did not change as a result of a uniform irradiation field.

There are some interesting aspects of radiation hardening and softening, which are functions of the structure temperature, when one considers the influence of prolonged neutron irradiation. Comparing Figure 102a to 105a, it can be seen that the maximum Mises stress in the FW decreases from 397 MPa at BOL to 323 MPa at 45 dpa due to softening caused by neutron irradiation at 500°C. This can be explained from Figure 29a, where σ_y at 45 dpa is smaller than σ_y at BOL (0 dpa) at temperatures above

392°C. The FW temperature is about 500°C, as shown in Figure 97c, suggesting σ_y of 400 MPa at BOL which reduces to 312 MPa at 45 dpa (Figure 29a). Having stresses above σ_y at 45 dpa shown in Figure 105a reflects the effect of the linear hardening plasticity model, shown in Figure 31b. FW softening at 45 dpa is also noticeable when we compare the effective plastic strain at BOL (Figure 103a) with that at 45 dpa (Figure 106a), showing a significant increase. This can be better understood by comparing the stress-strain curves at 500°C (FW temperature) in Figure 31b, showing 45 dpa curve below zero dpa at BOL.

Comparing the results of 90 and 45 dpa case studies, one can see that the effect of irradiation-induced swelling is to increase the stress and effective plastic strain, as shown in figures 105 and 106. We note here that because module expansion is not prevented, the accumulated plastic strain is low as a result of neutron irradiation. Also, it is important to notice that at 500°C and 90 dpa, F82H undergoes hardening (Figure 31b) causing the structure to show higher stresses at the FW, unlike at 45 dpa at 500°C which displayed a softening effect.

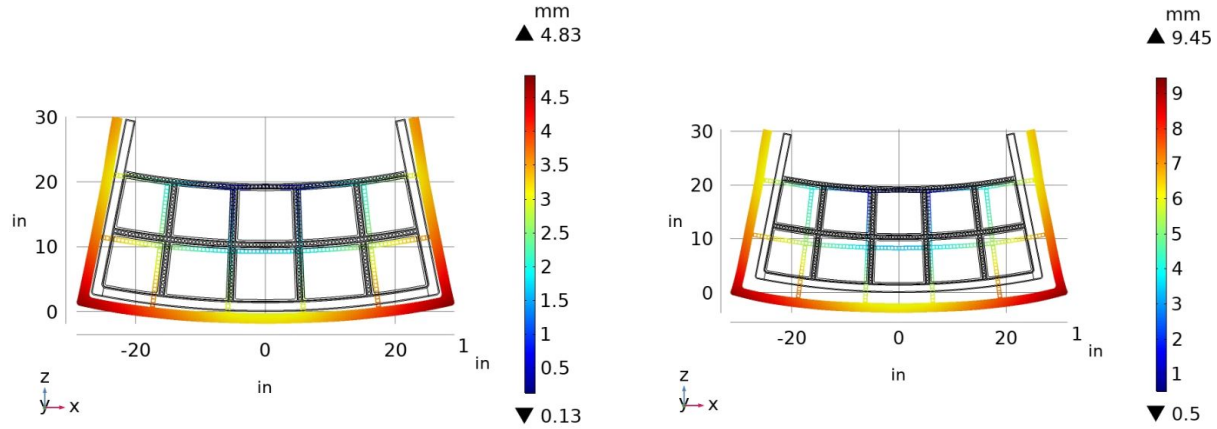

Figure 104: Displacement results (scale factor 15) for uniform irradiation and swelling of free side walls at (a) 45 and (b) 90 dpa.

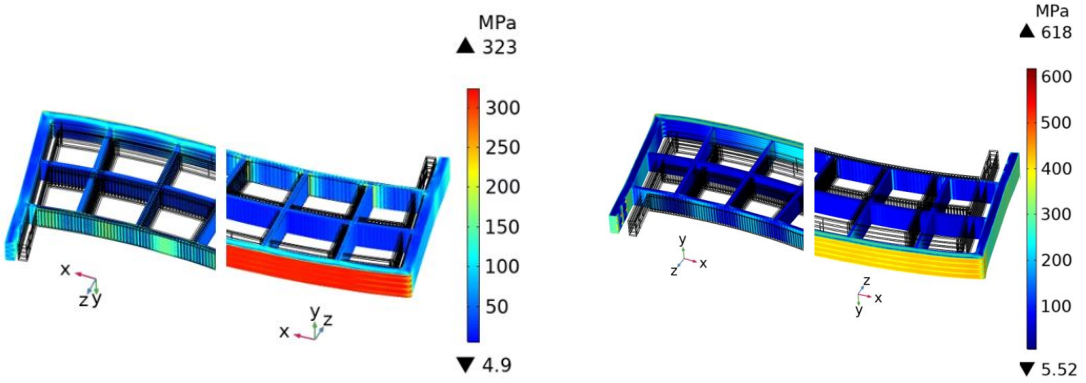

(a) (b)

Figure 105: Front and back view of the stress distribution for uniform irradiation and swelling of free side walls at (a) 45 and (b) 90 dpa.

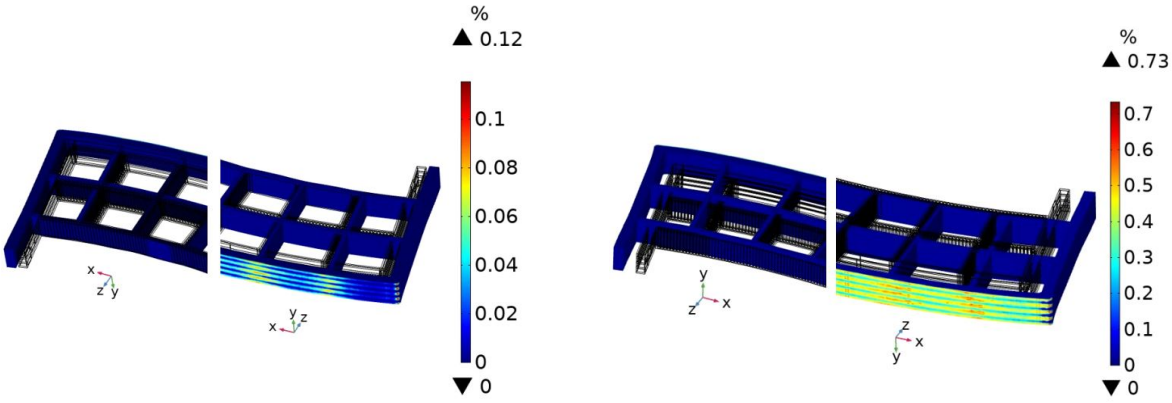

(a) (b)

Figure 106: Front and back view of the effective plastic strain for uniform irradiation and swelling of free side walls at (a) 45 and (b) 90 dpa.

(ii) Constrained side walls (45 and 90 dpa):

Similar to the BOL simulation results shown in section 8.4.2, constraining the side walls under uniform irradiation (45 and 90 dpa) increases the deformation, stress and effective plastic strain, in addition to altering the deformation mode to a bending-type. The center point of the FW structure facing the plasma side (region F) displaces by 46 mm into the plasma scrape-off region at 90 dpa, as can be seen in Figure 107b. Hardening and softening effects due to irradiation are observed in this case study as well. The top face of the FW corners are at 375 $^{\circ}C$ (Figure 97c) and σ_y at this temperature is about

460 MPa (Figure 29a). However, the stress in these regions shown in Figures 108a and 108b are much higher than σ_y. This level of stress is due to radiation hardening at 375 °C at both 45 and 90 dpa, as can be seen in Figures 31a and 29a. Irradiation-induced swelling together with irradiation hardening result in stresses up to 555 MPa and 680 MPa at 45 and 90 dpa, respectively, at top faces of the FW corners (region T), as shown in Figures 108a and 108b. We notice here in Figure 109b that the accumulated plastic strain is very large at the FW/B corner regions C and FJ, reaching over 7% at 90 dpa. These levels of plastic strain may not be tolerated by the limited ductility of the structure under irradiation, but this point needs further investigation of failure modes.

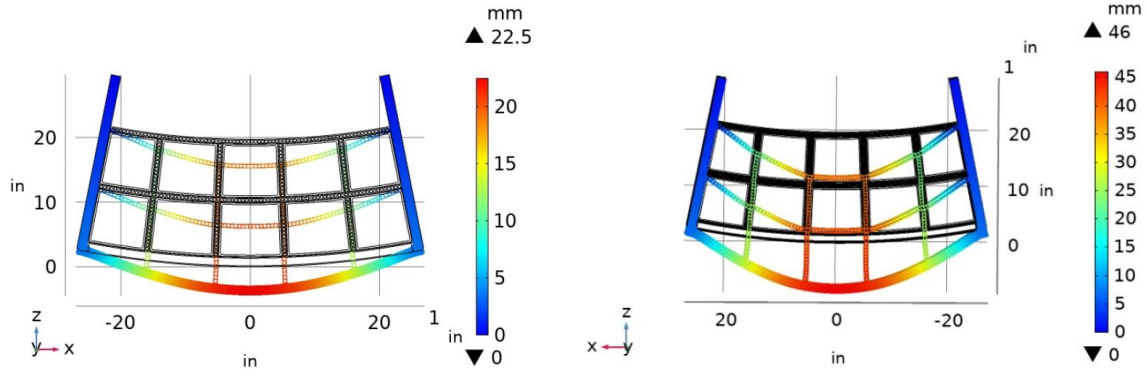

(a) (b)

Figure 107: Displacements (scale factor 5) for uniform irradiation and swelling of constrained side walls at (a) 45 and (b) 90 dpa.

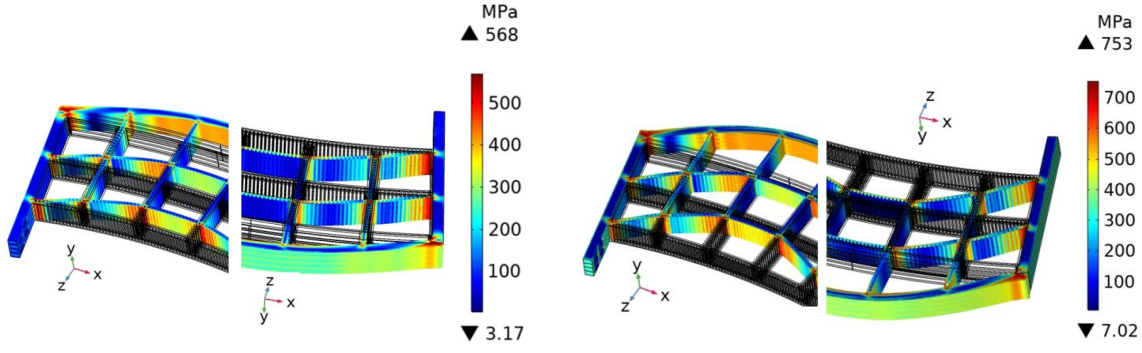

(a) (b)

Figure 108: Stress distributions for uniform irradiation and swelling of constrained side walls at (a) 45 and (b) 90 dpa.

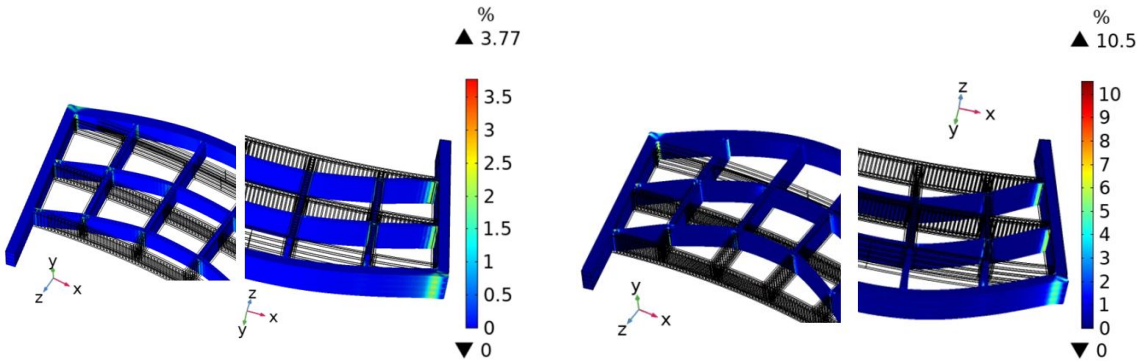

(a) (b)

Figure 109: Effective Plastic Strain distributions for uniform irradiation and swelling of constrained side walls at (a) 45 and (b) 90 dpa.

8.4.4 The influence of Spatial Gradients in the Irradiation Field

We proceed in this section to analyze the behavior of the FW/B structure under more realistic irradiation conditions, where the radiation field variables (dpa, helium generation rate) as well as temperature are all functions of the spatial location in the structure. Of concern is the steep gradients in the swelling and helium generation rates as a result of neutron interaction with the structure. The neutron displacement damage rate is at its maximum of 14.8 dpa/year at the FW, declining precipitously to only 0.24 dpa/year at the back end of the module (Figure 100b). We performed our structural analysis at 3 years (44.5 down to 0.7 dpa) and 6 years (88.9 down to 1.4 dpa).

(i) Free side walls (3 & 6 years of irradiation):

The influence of spatial gradients in irradiation-induced swelling and plasticity parameters on structural deformation is shown in Figure 110, which display a different type of displacement mode. It can be seen that the FW experiences larger expansion in the toroidal direction compared to the rest of the structure causing a "fanning mode" of deformation. This is to be contrasted with what we observed before in the reference uniform irradiation field case, where two other modes were observed: (1) uniform growth mode (unconstrained side walls); and (2) bending mode (constrained side walls). Com-

paring the results with those shown in Figure 104, it can be seen that changes in the displacement of the FW/B module from region C to the Roller at space-dependent 3 years irradiation (Figure 110a) is greater than the reference case under uniform irradiation (Figure 104a). This difference is even larger at 6 years (Figure 110b) as compared to the uniform 90 dpa case (Figure 104b). Having this type of displacement gradient in the structure increases the stress levels and effective plastic strain, as it can be seen by comparing Figures 105 and 111 for stress distributions, and Figures 106 and 112 for the effective plastic strain distributions.

The extent of the fanning mode deformation under 6 years of space-dependent irradiation reveals that the free side wall study at 6 years is similar to the constrained side wall studies where the back face of the FW (region B) shows higher stresses than the front face (region F) due to bending effects, as describe in section 8.4.2ii. This is shown in Figure 111b.

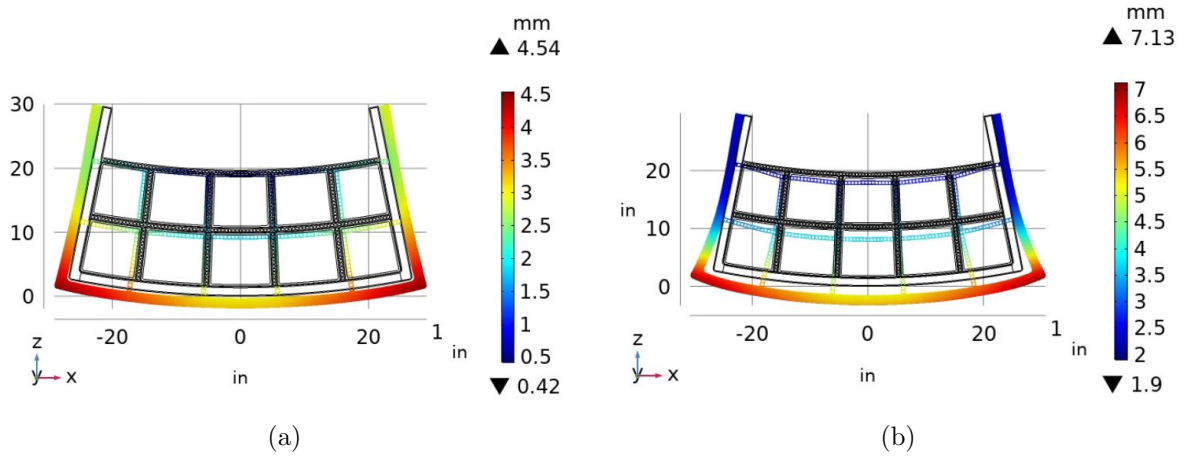

Figure 110: Displacement results (scale factor 15) for space-dependent irradiation and swelling of free side walls at (a) 3 years (44.5 down to 0.7 dpa) and (b) 6 years (88.9 down to 1.4 dpa).

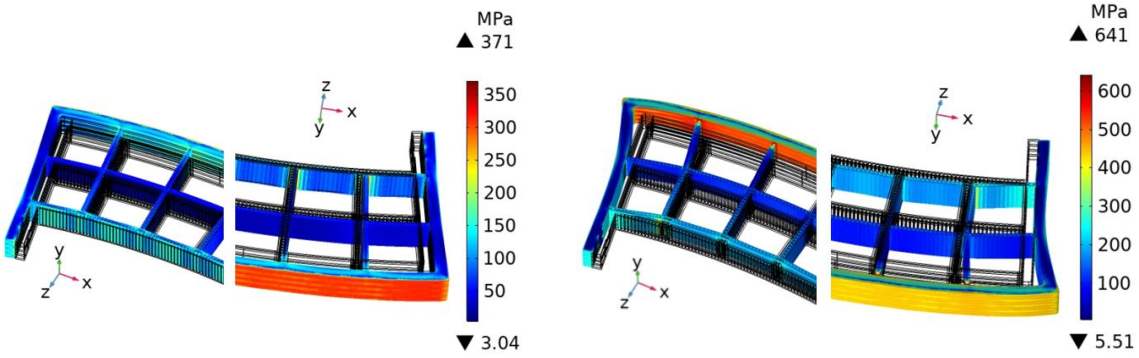

(a) (b)

Figure 111: Stress distributions for space-dependent irradiation and swelling of free side walls at (a) 3 years (44.5 down to 0.7 dpa) and (b) 6 years (88.9 down to 1.4 dpa).

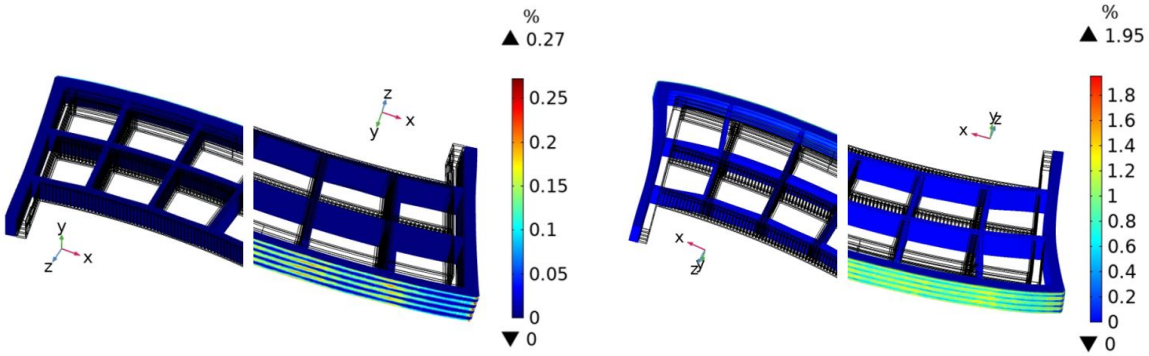

(a) (b)

Figure 112: Effective Plastic Strain results for space-dependent irradiation and swelling of free side walls at (a) 3 years (44.5 down to 0.7 dpa) and (b) 6 years (88.9 down to 1.4 dpa).

(ii) Constrained side walls (3 & 6 years of irradiation):

Similar to the previous constrained side wall case studies (sections 8.4.2ii and 8.4.3ii), we observe that constraining the side walls changes the deformation mode to a bending-type and increases the stress at the corners of FW, IW and BW (regions C, FJ and RJ). In addition, constraining the side walls increases the stress level at the back face of the FW (region B) making it even higher than the front face of FW (region F) due to the influence of bending stresses as described in section 8.4.2ii. Also, hardening and softening effects are observed in this study as discussed in previous sections. Constraining the side walls increases the FW mid-plane (region F) displacement from 3.1 mm to

21 mm for 3 years case study, and from 5.3 mm to 31 mm for 6 years case study, as can be seen by comparing Figures 110 and 113.

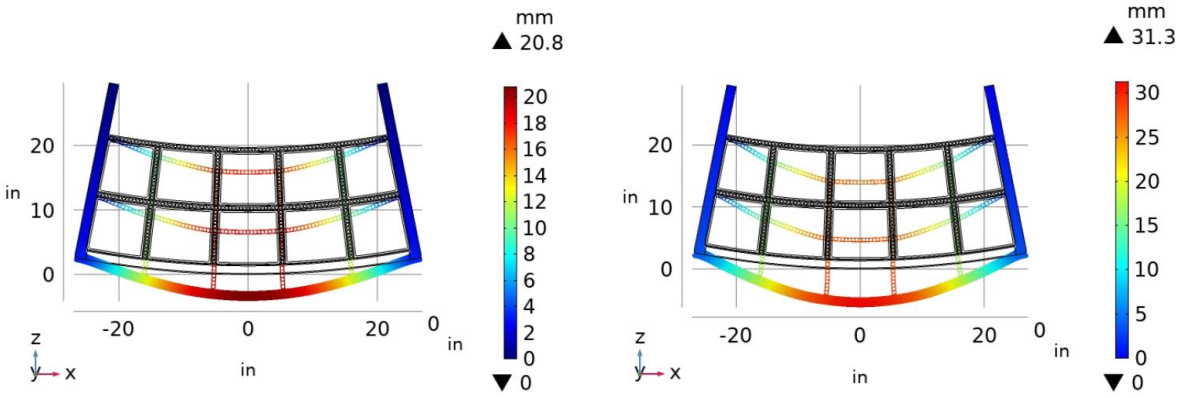

(a) (b)

Figure 113: Displacement results (scale factor 5) for space-dependent irradiation and swelling of constrained side walls at (a) 3 years (44.5 down to 0.7 dpa) and (b) 6 years (88.9 down to 1.4 dpa).

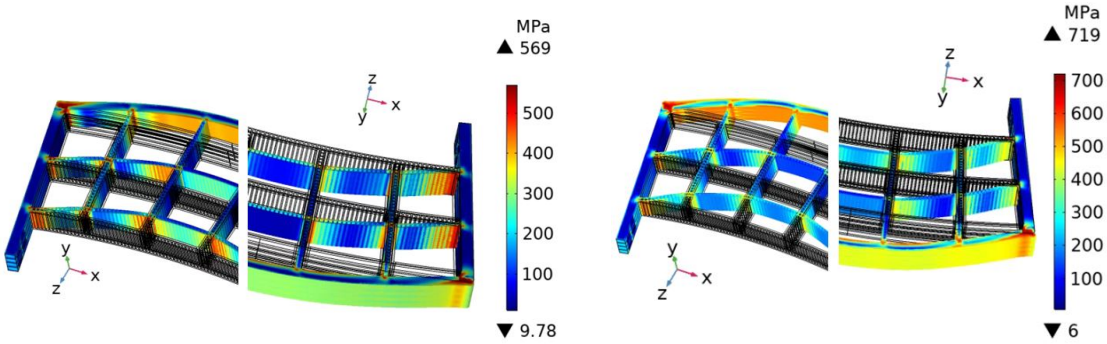

(a) (b)

Figure 114: Stress results for space-dependent irradiation and swelling of constrained side walls at (a) 3 years (44.5 down to 0.7 dpa) and (b) 6 years (88.9 down to 1.4 dpa).

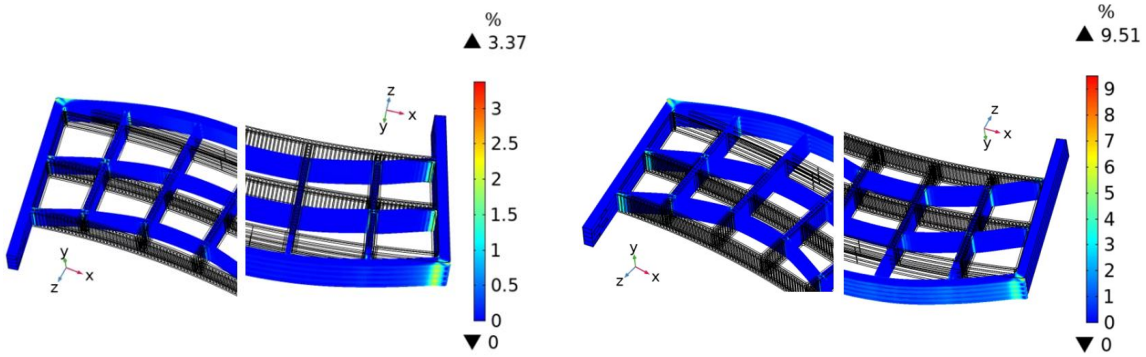

(a) (b)

Figure 115: Effective Plastic Strain results for space-dependent irradiation and swelling of constrained side walls at (a) 3 years (44.5 down to 0.7 dpa) and (b) 6 years (88.9 down to 1.4 dpa).

8.5 Summary & Conclusions

This study of the deformation and stress evolution of large-scale fusion energy structures is first-of-a-kind. Past efforts to model stress evolution and global deformations in FW/B structures were limited by two main impediments: (1) lack of computational methods that account for property changes as function of several radiation parameters simultaneously; and (2) the availability of a data-base upon which reasonable predictions can be made. We concentrated here on exploring the various ways by which the large FW/B structure can deform as it ages in a fusion reactor. We also explored the evolution of stresses and the accumulation of plastic strain as functions of neutron irradiation dose. Follow-up studies will consider failure modes driven by plastic strain accumulation and by the evolving stress field that can drive cracks through the FW/B structure. The following conclusions can be made:

1. The maximum stress at BOL for free side walls occurs at the FW regions S and C (Figure 102a). Constraining the side walls at BOL changes the stress state by reducing the stress magnitude at the mid-plane of the FW front face (region F) and increasing the stress at the mid-plane of FW back face (region B). Also, stress concentrations increase at the joints between the FW/IW/BW and radial stiffening ribs and side

walls (regions C, FJ and RJ) due to bending effects. The maximum plastic strain at BOL occurs for constrained side walls at regions C, FJ and RJ (Figure 103b), where there are maximum stress concentrations.

2. The reference case of uniform irradiation field for free side walls at 45 dpa shows softening of the FW front face especially at region S, reducing the stress and increasing the plastic strain level at this region as it can be seen by comparing Figure 102a with Figure 105a for stresses and Figure 103a with Figure 106a for plastic strain. However, at 90 dpa, the FW front face shows hardening that leads to higher stresses (Figure 105b) and higher plastic strain (Figure 106b) enhanced by irradiation-induced swelling. Similar to the BOL case, constraining the side walls changes the stress state and the maximum stress shifts to areas shown by regions B, C, FJ and RJ with the maximum plastic strain in regions C, FJ and RJ (Figure 109).

3. Gradients in the irradiation field variables (dpa and helium generation) introduces larger displacement difference between regions C and the reference roller (comparing Figure 104 with Figure 110), causing a fanning deformation mode. Extreme deformation is observed for free side walls at 6 years (Figure 110b), which increases the stress at the back face of the FW (Figure 111b). The stress and plastic strain in the FW/B structure all increase due to radiation gradient effects. Constraining the side walls increases the bending type deformation and displacements, with the maximum displacement at the mid-plane of FW (region F) reaching to 31 mm (Figure 113b). The maximum stress occurs in regions B, C, FJ and RJ (Figure 114) and the maximum plastic strain in regions C, FJ and RJ (Figure 115). Failure mode analysis should consider these regions separately.

4. If the side walls are constrained for reasons of closing neutron streaming gaps compressive regions show extreme plastic strain accumulation (regions C and FJ). The build-up of residual stresses can cause crack propagation upon cool-down and during cyclic reactor operations. Regions B, F, S, C and FJ all experience compressive stresses during heat-up, which may not be a concern in terms of crack opening. However, the regions

that undergo compressive plastic deformation (regions C and FJ) can see severe tensile residual stresses upon cool-down, followed by crack propagation and failure. On the other hand, region RJ is under extreme tensile stress during operation (heat-up) and can show failure during reactor operation time, if cracks propagate due to low fracture toughness. This region requires sophisticated fracture mechanics analysis ensuring adequate safety margins.

5. Some potential failure concerns can be alleviated by design optimization. This may include controlling the cooling patterns of the structure to maintain a high yield strength in desired areas (region C) so as to prevent extreme plastic strain accumulation and to allow reduction in the yield strength in other areas that are under extreme tensile stresses (region RJ) so as to lower the stress magnitude and to introduce reasonable plastic deformation preventing sever cracking.

6. Constraining the side walls (8.4.2ii, 8.4.3ii, and 8.4.4ii) brings noticeable stress concentrations to the joints between the FW/IW/BW and the radial stiffening ribs and also with the side walls, specially in regions RJ, C and FJ. This issue can be addressed by increasing the fillet radius in these regions to reduce the stress concentration. A limitation may be the increased amount of structure that can impact the tritium breeding ratio.

7. Comparing the constrained and free cases, one can come up with a prescribed spacing between the IB blanket sectors that would close up during heat up and would allow enough displacement to balance the stress distribution on modules reducing stress concentrations and plastic strain in the structure, and at the same time would make it easier to replace the module at the end of lifetime.

8. Three distinct dimensional stability modes have been revealed in the current study. These are: “self-similar growth mode” for unconstrained modules; (2) “bending mode” for constrained modules; and (3) “fanning mode” associated with radiation damage gradients.

9. The maximum structural displacements and their locations are summarized in Table 4.

Table 4: Maximum structural displacements (mm)

BOL	45 dpa	90 dpa	Region
Free Side Walls-Uniform			
4	4.8	9.5	C
Constrained Side Walls-Uniform			
18.4	22.5	46	F
Free Side Walls-Gradient			
4	4.5	7.1	C

CHAPTER 9

Effects of Thermal Creep on Stress Evolution and Deformation in Fusion Structures

Large fusion energy structures (FW/B) were studied in great detail in Chapter 8 providing the effects of thermal and radiation fields on stress evolution and deformation under two different constraints (boundary conditions). In the first case, (*Free side walls* - section 8.4), the FW/B side walls were allowed to expand freely under thermal and pressure loading. In the second case (*Constrained side walls* - section 8.4), the side walls were constrained from displacement in the normal direction assuming that the modules had no gap during assembly. Structural analyses were performed considering these two boundary conditions for the **BOL** (section 8.4.2), **Uniform Irradiation Field** case (section 8.4.3), and for the **Spatially-varying Irradiation Field** case (section 8.4.4).

The primary goal of the research reported in this chapter is to determine the influence of thermal creep on stress evolution and deformation of the FW/B structure as it is irradiated during service. The study is focused on the case of *free side wall* boundary conditions, assuming that the design of a tokamak-type fusion reactor will include gaps in between modules during assembly to allow free expansion normal to the FW/B side walls. Here we utilized the setup for the **Spatially-varying Irradiation Field** case (described in section 8.4.4). The irradiation field variables (dpa, helium generation rate) are all functions of the special location in the FW/B structure. A linear hardening plasticity model of irradiated materials and inelastic volumetric swelling deformation are considered in the study, as described in detail in Chapter 8. Also, similar to Chapter 8, all material properties used in the FE simulations here are functions of irradiation and temperature. Keeping the same thermal and pressure loading on the FW/B, we will study thermal creep effects on this structure, and

will compare the stress and deformation state with previous results presented in Chapter 8, which did not include the effects of creep.

In order to study the creep effect, Norton creep law (equation 52) with temperature dependent parameters A and n is applied in FE simulations as follows;

$$\varepsilon^{\circ} = A\sigma^{n} \tag{52}$$

where, ε° is the strain rate in 1/s and A and n are temperature dependent parameters for Eurofer steel obtained from [79] as tabulated in Table 5. It is important to notice that all the material properties used for FW/B in Chapter 8 are from F82H steel. Since F82H creep data was not available in temperature range required for our study, we used Eurofer steel creep properties from Tavassoli report [79] in this chapter (F82H and Eurofer are both low-activation steels suggested for fusion applications and they are very similar to each other). In table 5 the temperature dependent parameters start from 450 °C assuming the creep is negligible below this temperature for this type of steel. According to FW/B temperature distribution (Figures 97c and 98) obtained from our heat transfer analysis in section 8.3, only *first wall* (Figure 100a) and its helium cooling channels are above 450 °C (Figure 122a) and will go under creep deformation. Creep is negligible on the rest of FW/B.

Table 5: Norton creep law parameters[79].

Temperature (°C)	A (1/s)	n
450	2.32×10^{-66}	22.72
500	3.82×10^{-60}	21.19
550	1.27×10^{-49}	17.77
600	6.92×10^{-29}	9.51
650	1.73×10^{-21}	6.75

Strain rate as function of stress is plotted at different temperatures using Norton creep law (equation 52) and tabulated parameters in table 5 for Eurofer steel as shown in Figure 116.

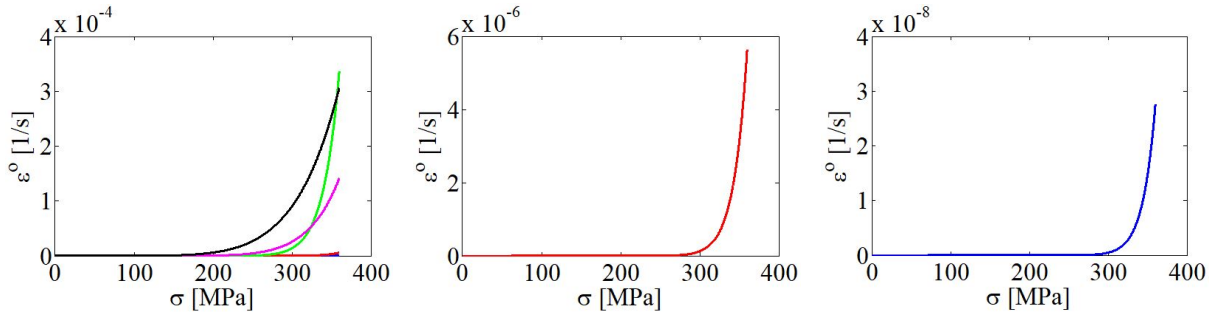

Figure 116: Strain rate plotted as function of stress for Eurofer steel using Norton creep law at different temperatures. (a) Strain rate at 650 °C plotted in black, 600 °C in magenta, 550 °C in green, 500 ° C in red and 450 °C in blue. For better visualization strain rate at 500 °C is separately plotted in (b) and strain rate at 450 °C is plotted in (c).

The creep FE time-dependent simulation is performed for 3-years including special and time dependent irradiation effects. The irradiation damage dose per year is shown in Figure 100b along the radial distance from the FW. The FE results from BOL *free side walls* are used as initial condition for this creep study. The displacement, Von Mises stress and effective creep strain are shown in Figures 117a, 117b and 118b respectively. Comparing displacement results presented in Figure 117a with no creep case shown in Figure 110a it can be seen that creep doesn't make significant changes in the deformation mode of the FW/B. However, the Von Mises stress at regions F, S and C of FW/B (the different regions on FW/B are shown in Figure 100a) studied here (Figure 117b) are much smaller than the ones presented for no creep case (Figure 111a). This is due to creep relaxation. Effective creep strain is highest at the corners of FW/B (region C) reaching to 0.5 %. This is due to structure's higher temperature (540 °C) at these corners.

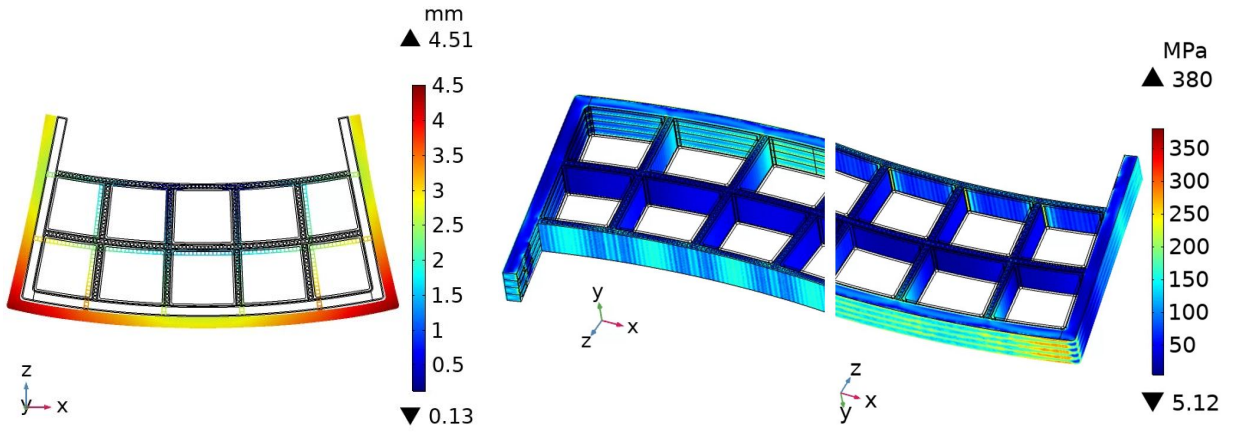

(a) (b)

Figure 117: (a) Displacement (scale factor 15) and (b) Von Misses stress after 3 years creep including special and time dependent irradiation effects for *free side walls* boundary condition.

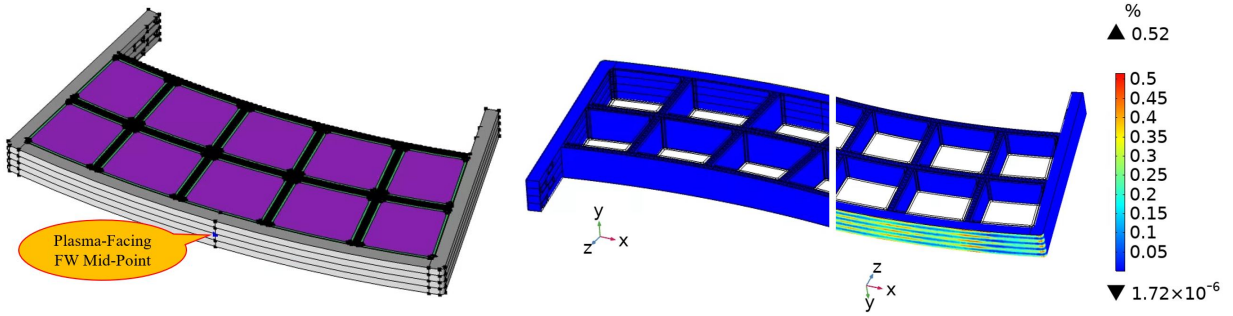

(a) (b)

Figure 118: (a) Mid-point at plasma facing FW. (b) Effective creep strain after 3 years creep including special and time dependent irradiation effects for *free side walls* boundary condition.

The Von Mises stress at plasma-facing FW mid-point (Figure 118a) is plotted for 3 years in Figure 119. It can be seen that stress initially reduced from 360 MPa at BOL to 145 MPa in 2500 hours and then accumulated swelling raised the stress level to 170 MPa at the end of 3 years. Reduction of the stress on FW is due to both radiation softening and creep relaxation effects. The radiation softening can be explained by Figure 28a where at 500 °C (the entire FW is at 500-540 °C as shown in Figure 97c) F82H undergoes irradiation softening (reducing yield strength) for 0-64 dpa range. In 3-years study performed here the irradiation dose on FW starts from zero at BOL and increases to 44.5 dpa at the end of 3 years (14.8 dpa/year as shown in Figure 100b). Therefore, FW experiences radiation

softening the entire 3-years which reduces the yield strength of F82H lowering the stress level and increasing the plasticity on the structure. Also, increasing creep deformation (strain) reduces the elastic strain (Figure 120) which lowers the stress on the structure (Figure 119) in expense of creep deformation.

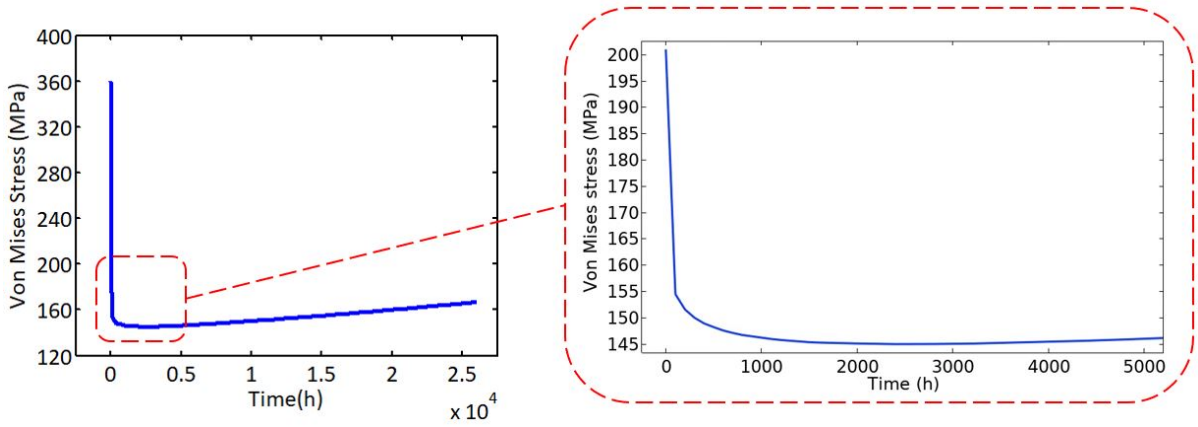

Figure 119: Von Mises stress from FE simulation of 3 years creep including special and time dependent irradiation effects for *free side walls* boundary condition plotted at Plasma-facing FW mid-point (Figure 118a).

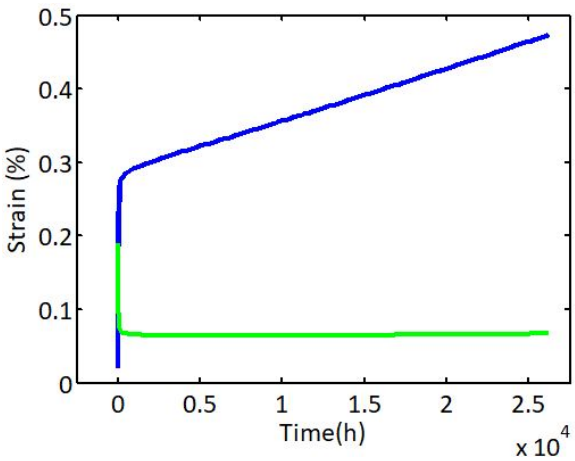

Figure 120: Effective creep strain plotted in blue and effective elastic strain plotted in green from FE simulation of 3-years creep including special and time dependent irradiation effects for *free side walls* boundary condition plotted at Plasma-facing FW mid-point (Figure 118a).

It is important to notice that creep rate is higher at the first 2500 hours (sharp increase in effective creep strain observed in Figure 120 and sharp stress decline observed in Figure 119) because the stress on FW is higher at the beginning of life ($\approx$ 360 MPa reported for BOL, Figure 102a). The creep rate reduces in time due to reduction in stress magnitude

from creep relaxation and irradiation softening. This can be described by Figure 116 where at a given temperature creep rate (ε^o) is lower at lower stress levels.

To compare the effects of radiation softening and creep relaxation on the stress state, the Von Misses stress at regions F and C is tabulated in Table 6 for studies performed at **BOL** (Figure 102a), **Spatially-varying Irradiation Field** at the end of 3-years (Figure 111a) and **Creep and Spatially-varying Irradiation Field** at the end of 3-years (Figure 117b).

Table 6: Von Mises stress at regions F and C on FW/B (these regions are shown in Figure 100a) obtained from different studies showing the effects of irradiation and creep.

Study	Von Mises [MPa] at F	Von Mises [MPa] at C
BOL	360	360
Spatially-varying Irradiation Field, 3-years	310	310
Creep & Spatially-varying Irradiation Field, 3-years	170	275

Also, effects of spatially-varying irradiation field and creep are shown at FW/B mid-plane cross-section (Figure 121) in Figure 122. Comparing results at BOL (Figure 122b) with the ones obtained using special-varying irradiation field (Figure 122c) it can be seen that the outer-wall stress reduced from 360 MPa to 310 MPa and the inner-wall stress increased from 150 MPa to 325 MPa after 3 years irradiation. This is due to combined effect of irradiation softening and swelling where the outer-wall which is at higher temperature developed more softening compare to the inner-wall. Also, comparing the special-varying irradiation case (Figure 122c) with the creep (including special-varying irradiation field) case shown in Figure 122d it can be seen that the stress at outer-wall reduced form 310 MPa to 170 MPa and at the inner-wall reduces from 325 MPa to 275 MPa due to creep relaxation. The creep relaxation is higher at the outer wall because it is at higher temperature compare to the inner wall (outer-wall is at 515 °C and the inner-wall is at 450 °C as shown in Figure

122a) which leads to a higher creep rate. Creep rate is almost 100 times higher at 500 °C compare to 450 °C as shown in Figure 116.

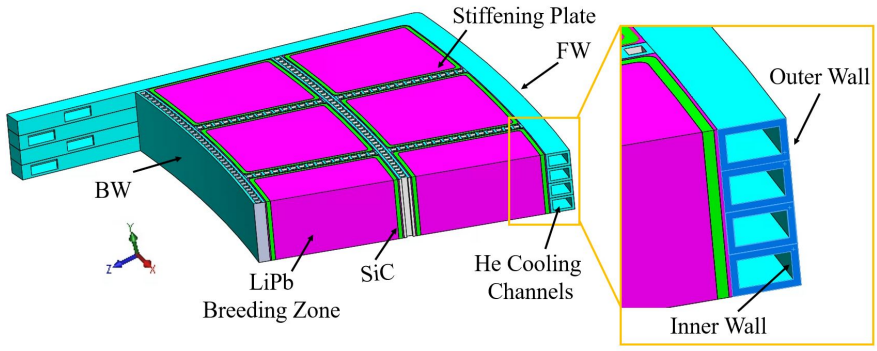

Figure 121: Cross-section of fist wall at its mid-plane showing outer and inner walls of He cooling channels.

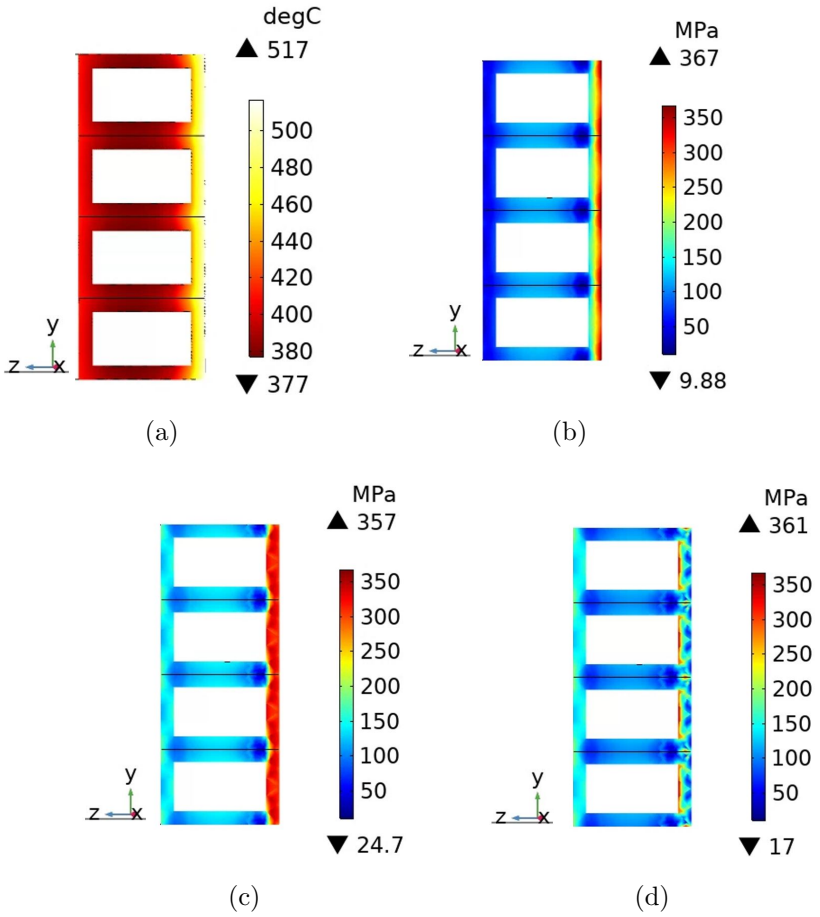

Figure 122: (a) Temperature distribution on FW/B mid-plane cross-section. Von Misses stress for *free side wall* boundary condition at (b) BOL, (c) end of 3-years of spatially-varying irradiation and (d) end of 3-years creep including spatially-varying irradiation at the He cooling channels in FW/B mid-plane.

In summary, creep can cause stress relaxation reducing the stress level in the structure. However, this would be in expense of creep strain and plastic deformation. Having high plastic deformation in the structure leads to brittle crack opening and crack propagation upon cool-down due to residual stresses. Also, plastic deformation can increase the chance of fatigue failure in cyclic loading. Lastly, if the creep deformation and plasticity accumulates cycle to cycle in pressurized cooling channels under thermal cyclic loading, the material will get to ratcheting regimes leading to rupture and catastrophic failures. Therefore, it is important to perform a detailed cyclic loading analysis and determine a design temperature for the structure to keep the creep rate low enough preventing these failures.

CHAPTER 10

Thesis Summary and Conclusions

Increasing interest in efficient power conversion systems, such as fusion reactors, has promoted considerable research on high-temperature materials and their thermomechanical behavior at elevated temperatures. Meanwhile, high-temperature materials are finding many applications, such as in the leading edge of hypersonic vehicles, compact heat exchangers, etc.. Tungsten is one of the main candidates for these applications due to its high melting point (3422 °C) and good mechanical properties at high-temperatures. However, its applications are limited to its brittle behavior below its DBTT (≈ 200-400 °C) and after its recrystallization (≈ 1300 °C). Rapid temperature transients and thermal stresses develop *through-thickness* cracks in tungsten which can cause component failure. Although such cracks are often described as *thermal shock* cracks, the exact origin of this type if failure is not always clear. The research presented in this thesis is focused on characterization of high-temperature plasticity and behavior of structural materials such as tungsten via a combination of theoretical, computational, and experimental methods. The main objective is to design experiments to investigate different failure modes in high-temperature material mainly tungsten. This is achieved by designing and fabricating a variety of sample fixtures to impose desired loading and boundary condition on samples in high-temperature tests performed in HEFTY. Also, in order to define the thermal loading conditions, a heat flux sensor was designed and used to measure the heat flux in HEFTY. The heat flux profile for the HEFTY plasma arc-jet was thus developed, which can be used in FE simulations describing these tests.

Experiments where one can control the constraints and boundary conditions in addition to mechanical and thermal loading conditions were designed to better represent material

behavior while in service. High-temperature plasticity under cyclic loading gets even more complicated as material properties change under the influence of high temperature. Microstructural changes, such as re-crystallisation can change material properties, namely the yield strength and fracture toughness, due to changes in grain size and impurity migration to grain boundaries. Experimental work presented in this thesis included detailed pre- and post- material characterization, such as SEM, FIB imaging, and EDS, to study the effects of high temperature loading on material microstructure. This helps to better understand and explain the reasoning behind materials behavior and cracking under different constraints and loading conditions.

Since there are some challenges in designing HHFFCs from tungsten due to its brittle fracture below the DBTT and above the recrystallization temperature, W foam is proposed as a sacrificial non-structural armor so as to protect cooled components from thermal shock and residual stress induced failure. This was demonstrated by a series of experiments performed on W foam fabricated by Ultramet Inc. First, variety of W foam samples were tested using designed sample fixtures under high heat flux loading to investigate the best combination of volume fraction and PPI that provide enough porosity to withstand extreme thermal transients. After defining the best volume fraction and PPI for W foam in high heat flux applications, foam samples were tested under higher heat flux conditions and were compared directly to solid tungsten disks under the same conditions. The damage in tested W foams and disks were compared and presented quantitatively in terms of the COD distribution, crack length, recrystallization and grain growth. This study showed that W foams are more resilient to damage due to high heat flux and thermal transients. The type of thermal damage is manifest as a network of micro-cracks with smaller COD compared to solid W disks, where cracks developed with larger COD and through-thickness penetration. This is due to the porosity content of W foam, where ligaments can freely expand at high temperature and are flexible enough to bend or rotate at their triple junctions accommodating thermal strains. In contrast, stresses induced by thermal strains develops plasticity in W disks during sample heat-up, which raises tensile residual stresses upon cool-down causing brittle cracks and fracture. This is more pronounced at local high heat flux loading on W disks,

where the surrounding material at lower temperature constrains the central loaded zone developing more plasticity during heat-up. In order to demonstrate this idea of material self-constraint under rapid local loading, several testes were performed using specially designed sample fixtures, where spring loaded clamps allowed W disks to freely expand. It was shown that W disks under high-heat flux rapid local loading develop large through-thickness cracks, even if they are free to expand, supporting the notion of material self-constraint. Also, this is well demonstrated by comparing the tests performed on the 2.5 cm and 5.1 cm diameter W disks, where the latter developed much larger cracks due to having more material at lower temperature surrounding the central hot zone. In addition, observing many intergranular cracks in SEM images suggested that grain boundary weakening after recrystallization took place at high temperature. This can be due to migration of impurities to grain boundaries. Another advantages of W foam is that it has less impurity content compared to solid tungsten due to its manufacturing process (CVD). SEM images showed less cracking on grain boundaries of recrystallized W foam compare to solid tungsten. Detailed FE simulations were performed on both W foams and W disks to describe experimental results. Temperature dependent effective properties were used in W foam simulations to represent thermal and mechanical behavior of the foam without a need to perform simulations on actual foam geometry.

The second goal of the research presented in this thesis was to develop a framework to model and demonstrate material degradation effects under high temperature and irradiation on HHFFCs, such as the FW/B structures in fusion energy devices. This is performed by modeling linear hardening plasticity of irradiated materials and inelastic deformation by swelling and creep in FE simulations. Temperature-dependent irradiation effects, such as swelling and irradiation hardening/softening, are used as functions of geometry and time over the service life of the FW/B structure. The deformation and stress evolution are studied in FE simulations for two different configurations namely *free side walls* and *constrained side walls* to emphasis the effect of constraints and boundary condition in stress state of the structure. It is shown that constraining the side walls increases the bending type deformation and stresses. Several suggestions are provided on FW/B design to reduce the stress and

deformation level including a gap between FW/B sectors (there are 16 sectors in doughnut-shape tokamak as shown Figure 95) to accommodate thermal strain reducing the stress level on structure. Also, the influence of irradiation field's spatial gradients on the stress state and deformation mode of FW/B is studied by comparing the FE simulation results from a uniform irradiation field case study with the one obtained from a study using spatially-varying irradiation field. It is shown that the spatially-varying irradiation field can increase the stress state in FW/B and introduce fanning mode deformation in which the FW deforms more than the rest of the structure due to higher irradiation dose and swelling effects on it.

Later, lifetime of fusion energy structure (FW/B) is studied considering thermal and radiation fields effects. This is done by performing creep analysis on FW/B using Norton creep law in FE simulations. In order to include the effect of temperature in creep rate, temperature dependent parameters are used for Norton creep law. This study is performed using *free side walls* boundary condition assuming the tokamak-type fusion reactor will include gaps between modules during assembly to satisfy free expansion normal to the FW/B side walls. The FW/B is studied for 3-years creep including spatially-varying irradiation field. The irradiation dose (in units of dpa) is also function of time in this study. It is shown that the reduction in stress on FW over 3 years is due to both radiation softening and creep, leading to higher plasticity. Creep relaxation is due to increase in creep strain and plastic deformation which can lead to failures at cool-down due to residual stresses induced by large plasticity. Also, creep strain and plasticity can increase the chance of fatigue failure in cyclic loading. Since the He cooling channels are pressurized and go under thermal cyclic loading, material can go to ratcheting regimes and rupture if the plastic strain accumulates cycle to cycle.

It is observed that creep rate on FW is high at the begging of life when the stress is high on the structure and reduces as stress reduces due to creep relaxation and irradiation softening. Stress state is presented on cross-section of FW at its mid-plane for **BOL**, **Spatially-varying Irradiation Field** case, and **Creep Including Spatially-varying Irradiation Field** case to show the effect of irradiation and creep on the He cooling channels. It is shown that creep rate is higher at the outer-wall of FW He channels compare to the

inner-wall causing higher stress relaxation and more plastic deformation (creep strain). This is due to higher temperature on the outer-wall compare to the inner-wall. Also, Swelling induced strain increase the stress state of FW/B as the structure ages.

REFERENCES

[1] A Herrmann, I Zammuto, M Balden, H Greuner, N Jaksic, A Kallenbach, M Li, R Neu, V Rohde, and ASDEX Upgrade Team. Experiences with a solid tungsten divertor in ASDEX upgrade. *Nuclear Materials and Energy*, 12:205–209, 2017.

[2] Carl E Pigeon, Nathan G Orr, Benoit P Larouche, Vincent Tarantini, Grant Bonin, and Robert E Zee. A low power cylindrical hall thruster for next generation microsatellites. 2015.

[3] A-AF Tavassoli, J-W Rensman, M Schirra, and K Shiba. Materials design data for reduced activation martensitic steel type f82h. *Fusion engineering and design*, 61:617–628, 2002.

[4] Tungsten Mechanical Properties. www.plansee.com/en/materials/tungsten, 2019.

[5] Panagiotis Tolias, EUROfusion MST1 Team, et al. Analytical expressions for thermophysical properties of solid and liquid tungsten relevant for fusion applications. *Nuclear materials and energy*, 13:42–57, 2017.

[6] Chai Ren, Z.Zak Fang, Mark Koopman, Brady Butler, James Paramore, and Scott Middlemas. Methods for improving ductility of tungsten - a review. *International Journal of Refractory Metals and Hard Materials*, 75:170 – 183, 2018.

[7] Jens Reiser, Jan Hoffmann, Ute Jäntsch, Michael Klimenkov, Simon Bonk, Carsten Bonnekoh, Michael Rieth, Andreas Hoffmann, and Tobias Mrotzek. Ductilisation of tungsten (w): On the shift of the brittle-to-ductile transition (BDT) to lower temperatures through cold rolling. *International Journal of Refractory Metals and Hard Materials*, 54:351 – 369, 2016.

[8] Xiaoxin Zhang, Qingzhi Yan, Shaoting Lang, Min Xia, and Changchun Ge. Texture evolution and basic thermal–mechanical properties of pure tungsten under various rolling reductions. *Journal of Nuclear Materials*, 468:339 – 347, 2016.

[9] T. Hao, Z.Q. Fan, T. Zhang, G.N. Luo, X.P. Wang, C.S. Liu, and Q.F. Fang. Strength and ductility improvement of ultrafine-grained tungsten produced by equal-channel angular pressing. *Journal of Nuclear Materials*, 455(1):595 – 599, 2014. Proceedings of the 16th International Conference on Fusion Reactor Materials (ICFRM-16).

[10] Q Wei and LJ Kecskes. Effect of low-temperature rolling on the tensile behavior of commercially pure tungsten. *Materials Science and Engineering: A*, 491(1-2):62–69, 2008.

[11] RI Jaffee and CT Sims. The effect of rhenium on the fabricability and ductility of molybdenum and tungsten. Technical report, BATTELLE MEMORIAL INST COLUMBUS OH, 1958.

[12] H Bolt, V Barabash, W Krauss, J Linke, R Neu, S Suzuki, N Yoshida, and ASDEX Upgrade Team. Materials for the plasma-facing components of fusion reactors. *Journal of nuclear materials*, 329:66–73, 2004.

[13] Armando Giannattasio and Steve G Roberts. Strain-rate dependence of the brittle-to-ductile transition temperature in tungsten. *Philosophical Magazine*, 87(17):2589–2598, 2007.

[14] Peter Gumbsch. Brittle fracture and the brittle-to-ductile transition of tungsten. *Journal of Nuclear Materials*, 323(2-3):304–312, 2003.

[15] Peter Bernhard Hirsch, SG Roberts, and J Samuels. The brittle-ductile transition in silicon. ii. interpretation. *Proceedings of the Royal Society of London. A. Mathematical and Physical Sciences*, 421(1860):25–53, 1989.

[16] A Hartmaier and P Gumbsch. On the activation energy for the brittle/ductile transition. *Physica Status Solidi B Basic Research*, 202:R1–R2, 1997.

[17] James R Rice and Robb Thomson. Ductile versus brittle behaviour of crystals. *The Philosophical Magazine: A Journal of Theoretical Experimental and Applied Physics*, 29(1):73–97, 1974.

[18] Mahadevan Khantha, David P Pope, and Vaclav Vitek. Dislocation screening and the brittle-to-ductile transition: a kosterlitz-thouless type instability. *Physical review letters*, 73(5):684, 1994.

[19] HW Schadler. Mobility of edge dislocations on {110} planes in tungsten single crystals. *Acta metallurgica*, 12(8):861–870, 1964.

[20] G Federici, A Zhitlukhin, N Arkhipov, R Giniyatulin, N Klimov, I Landman, V Podkovyrov, V Safronov, A Loarte, and M Merola. Effects of ELMs and disruptions on ITER divertor armour materials. *Journal of nuclear materials*, (337-339):684–690, 2005.

[21] J Bree. Elastic-plastic behaviour of thin tubes subjected to internal pressure and intermittent high-heat fluxes with application to fast-nuclear-reactor fuel elements. *Journal of strain analysis*, 2(3):226–238, 1967.

[22] JoDean Morrow. Cyclic plastic strain energy and fatigue of metals. In *Internal friction, damping, and cyclic plasticity*. ASTM International, 1965.

[23] Jochen Linke. High heat flux performance of plasma facing materials and components under service conditions in future fusion reactors. *Fusion science and technology*, 49(2T):455–464, 2006.

[24] Muyuan Li and Jeong-Ha You. Cracking behavior of tungsten armor under ELM-like thermal shockloads II: A revised prediction for crack appearance map. *Nuclear Materials and Energy*, 9:598–603, 2016.

[25] G Pintsuk, I Bobin-Vastra, S Constans, P Gavila, M Rödig, and B Riccardi. Qualification and post-mortem characterization of tungsten mock-ups exposed to cyclic high heat flux loading. *Fusion Engineering and Design*, 88(9-10):1858–1861, 2013.

[26] Ermile Gaganidze, Daniel Rupp, and Jarir Aktaa. Fracture behaviour of polycrystalline tungsten. *Journal of Nuclear Materials*, 446(1-3):240–245, 2014.

[27] J Linke, Th Loewenhoff, Vincent Massaut, G Pintsuk, G Ritz, M Rödig, A Schmidt, C Thomser, Inge Uytdenhouwen, V Vasechko, et al. Performance of different tungsten grades under transient thermal loads. *Nuclear Fusion*, 51(7):073017, 2011.

[28] S Jitsukawa, M Tamura, B Van der Schaaf, RL Klueh, A Alamo, C Petersen, M Schirra, P Spaetig, GR Odette, AA Tavassoli, et al. Development of an extensive database of mechanical and physical properties for reduced-activation martensitic steel f82h. *Journal of Nuclear Materials*, 307:179–186, 2002.

[29] A-AF Tavassoli. Present limits and improvements of structural materials for fusion reactors–a review. *Journal of Nuclear Materials*, 302(2-3):73–88, 2002.

[30] Z Tong and Y Dai. Tensile properties of the ferritic martensitic steel f82h after irradiation in a spallation target. *Journal of nuclear materials*, 385(2):258–261, 2009.

[31] Nasr M Ghoniem, Giacomo Po, and Shahram Sharafat. Deformation mechanisms in ferritic/martensitic steels and the impact on mechanical design. *Journal of nuclear materials*, 441(1-3):704–712, 2013.

[32] Takuya Nagasaka, Hideo Sakasegawa, Hiroyasu Tanigawa, Masami Ando, Teruya Tanaka, Takeo Muroga, and Akio Sagara. Tensile properties of f82h steel after aging at 400–650 c for 100,000 h. *Fusion Engineering and Design*, 98:2046–2049, 2015.

[33] Takuya Yamamoto and G. Robert Odette. Fusion relevant engineering void swelling model for 9cr tempered martensitic steels. Technical Report DOE/ER-0313/67 – Volume 67, Fusion Reactor Materials Semiannual Report, Oak Ridge, TN, December 2019.

[34] Yamamoto Takuya Alam, E. and G. Robert Odette. Primary creep models for 9crw tempered martensitic steels: effects on the high-temperature dimensional stability of fusion structures. Technical Report DOE/ER-0313/68 – Volume 68, Fusion Reactor Materials Semiannual Report, Oak Ridge, TN, June 2020.

[35] Takuya Yamamoto and G. Robert Odette. Constitutive models for hardening of tempered martensitic steels at 300 to 500° up to high dpa and helium. Technical Report DOE/ER-0313/68 – Volume 68, Fusion Reactor Materials Semiannual Report, Oak Ridge, TN, June 2020.

[36] Warren Nadvornick, Arian Ghazari, Dylan Dickstein, Sohun Patel, Brian Williams, Don Hughes, and Nasr Ghoniem. Design, fabrication, and testing of a water-cooled high-heat flux plasma-facing module. *Journal of Nuclear Materials*, page In Preparation, 2022.

[37] Kuo Zhang, Ermile Gaganidze, and Michael Gorley. Development of the material property handbook and database of cucrzr. *Fusion Engineering and Design*, 144:148–153, 2019.

[38] Ali Gülhan. Heat flux measurements in high enthalpy flows. Technical report, GERMAN AEROSPACE CENTER (DLR) COLOGNE (GERMANY) INST OF FLUID MECHANICS, 2000.

[39] Jochen Max Linke, Takeshi Hirai, Manfred Rödig, and Lorenz Anton Singheiser. Performance of plasma-facing materials under intense thermal loads in tokamaks and stellarators. *Fusion science and technology*, 46(1):142–151, 2004.

[40] Yue Huang, Warren Nadvornick, Arian Ghazari, and Nasr M Ghoniem. Multiphysics-multiscale modeling of plasma-facing structures in extreme heat and radiation environments. *International Journal for Multiscale Computational Engineering*, 18(2), 2020.

[41] David Rivera, Richard E Wirz, and Nasr M Ghoniem. Experimental measurements of surface damage and residual stresses in micro-engineered plasma facing materials. *Journal of Nuclear Materials*, 486:111–121, 2017.

[42] Edward Gao, Warren Nadvornick, Russ Doerner, and Nasr M Ghoniem. The influence of low-energy helium plasma on bubble formation in micro-engineered tungsten. *Journal of Nuclear Materials*, 501:319–328, 2018.

[43] Muyuan Li and Jeong-Ha You. Interpretation of the deep cracking phenomenon of tungsten monoblock targets observed in high-heat-flux fatigue tests at 20 mw/m2. *Fusion Engineering and Design*, 101:1–8, 2015.

[44] M Wirtz, G Cempura, J Linke, G Pintsuk, and Inge Uytdenhouwen. Thermal shock response of deformed and recrystallised tungsten. *Fusion Engineering and Design*, 88(9-10):1768–1772, 2013.

[45] Inge Uytdenhouwen, Marc Decréton, Takeshi Hirai, Jochen Linke, Gerald Pintsuk, and Guido Van Oost. Influence of recrystallization on thermal shock resistance of various tungsten grades. *Journal of nuclear materials*, 363:1099–1103, 2007.

[46] M Wirtz, J Linke, G Pintsuk, L Singheiser, and Inge Uytdenhouwen. Comparison of the thermal shock performance of different tungsten grades and the influence of microstructure on the damage behaviour. *Physica scripta*, 2011(T145):014058, 2011.

[47] Shahram Sharafat, Akira Kobayashi, and Nasr M Ghoniem. Application of high-power plasma gun for thermal cycle testing of refractory foams. *Vacuum*, 73(3-4):475–480, 2004.

[48] S Sharafat, N Ghoniem, B Williams, and J Babcock. Cellular foams: a potential innovative solid breeder material for fusion applications. *Fusion science and technology*, 47(4):886–890, 2005.

[49] M Andersen, S Sharafat, and N Ghoniem. Thermo-mechanical analysis of a micro-engineered tungsten-foam armored inertial fusion energy first wall. *Fusion engineering and design*, 81(8-14):1639–1645, 2006.

[50] S Sharafat, A Mills, D Youchison, R Nygren, B Williams, and N Ghoniem. Ultra low pressure-drop helium-cooled porous-tungsten pfc. *Fusion Science and Technology*, 52(3):559–565, 2007.

[51] Michael F Ashby and Lorna J Gibson. Cellular solids: structure and properties. *Press Syndicate of the University of Cambridge, Cambridge, UK*, pages 175–231, 1997.

[52] VS Deshpande and NA Fleck. High strain rate compressive behaviour of aluminium alloy foams. *International Journal of Impact Engineering*, 24(3):277–298, 2000.

[53] Vikram S Deshpande and Norman A Fleck. Isotropic constitutive models for metallic foams. *Journal of the Mechanics and Physics of Solids*, 48(6-7):1253–1283, 2000.

[54] Vikram S Deshpande, Norman A Fleck, and Michael F Ashby. Effective properties of the octet-truss lattice material. *Journal of the Mechanics and Physics of Solids*, 49(8):1747–1769, 2001.

[55] Norman A Fleck, Vikram S Deshpande, and Michael F Ashby. Micro-architectured materials: past, present and future. *Proceedings of the Royal Society A: Mathematical, Physical and Engineering Sciences*, 466(2121):2495–2516, 2010.

[56] Rani Harb, Ertugrul Taciroglu, and Nasr Ghoniem. Partitioning of elastic energy in open-cell foams under finite deformations. *Acta materialia*, 61(5):1454–1468, 2013.

[57] Ming Yang Ma and Hong Ye. An image analysis method to obtain the effective thermal conductivity of metallic foams via a redefined concept of shape factor. *Applied thermal engineering*, 73(1):1279–1284, 2014.

[58] Gottfried Laschet, Jörg Sauerhering, Oliver Reutter, Thomas Fend, and Josef Scheele. Effective permeability and thermal conductivity of open-cell metallic foams via homogenization on a microstructure model. *Computational Materials Science*, 45(3):597–603, 2009.

[59] OE Petel, S Ouellet, AJ Higgins, and DL Frost. The elastic–plastic behaviour of foam under shock loading. *Shock Waves*, 23(1):55–67, 2013.

[60] Arian Ghazari, Cameron McElfresh, Dylan Dickstein, Jaime Marian, and Nasr Ghoniem. Effects of cyclic plasma heating on surface damage of micro-porous tungsten. *Physica Scripta*, 2021.

[61] Arian Ghazari, Dylan Dickstein, Warren Nadvornick, and Nasr Ghoniem. Heat flux measurements in the plasma arc-jet hefty facility. *Journal of Thermophysics and Heat Transfer*, page In Preparation, 2022.

[62] Dmitry Terentyev, Xiazi Xiao, A Dubinko, A Bakaeva, and Huiling Duan. Dislocation-mediated strain hardening in tungsten: Thermo-mechanical plasticity theory and experimental validation. *Journal of the Mechanics and Physics of Solids*, 85:1–15, 2015.

[63] Warren Isamu Nadvornick. *Erosion and Thermomechanical Behavior of Metallic Foams in Plasma Environments*. University of California, Los Angeles, 2021.

[64] T Sadowski and P Golewski. Multidisciplinary analysis of the operational temperature increase of turbine blades in combustion engines by application of the ceramic thermal barrier coatings (tbc). *Computational Materials Science*, 50(4):1326–1335, 2011.

[65] K Farrell, AC Schaffhauser, and JO Stiegler. Recrystallization, grain growth and the ductile-brittle transition in tungsten sheet. *Journal of the Less Common Metals*, 13(2):141–155, 1967.

[66] VP Budaev, Yu V Martynenko, AV Karpov, NE Belova, AM Zhitlukhin, NS Klimov, VL Podkovyrov, VA Barsuk, AB Putrik, AD Yaroshevskaya, et al. Tungsten recrystallization and cracking under iter-relevant heat loads. *Journal of Nuclear Materials*, 463:237–240, 2015.

[67] Marius Wirtz, J Linke, Th Loewenhoff, G Pintsuk, and Inge Uytdenhouwen. Thermal shock tests to qualify different tungsten grades as plasma facing material. *Physica scripta*, 2016(T167):014015, 2016.

[68] RL Barto and LJ Ebert. Deformation stress state effects on the recrystallization kinetics of molybdenum. *Metallurgical Transactions*, 2(6):1643–1649, 1971.

[69] CE Kessel, JP Blanchard, A Davis, L El-Guebaly, LM Garrison, NM Ghoniem, PW Humrickhouse, Y Huang, Y Katoh, A Khodak, et al. Overview of the fusion nuclear science facility, a credible break-in step on the path to fusion energy. *Fusion Engineering and Design*, 135:236–270, 2018.

[70] Adrian Cho. Scientists rally around plan for fusion power plant. *Science Magazine*, 370, Issue 6522:1258, 2020.

[71] David S Gelles, Nasr M Ghoniem, and Roger W Powell. Low activation ferritic alloys, November 11 1986. US Patent 4,622,067.

[72] Steven J Zinkle and Nasr M Ghoniem. Prospects for accelerated development of high performance structural materials. *Journal of Nuclear Materials*, 417(1-3):2–8, 2011.

[73] N.M. Ghoniem and R. Conn. Assessment of ferritic steels for steady-state fusion reactors. *International Atomic Energy Agency, Vienna (Austria); Panel proceedings series*, IAEA-TC–392/62:486–492, 1983.

[74] Yuhu Zhai, Peter Titus, Charles Kessel, and Laila El-Guebaly. Conceptual magnet design study for fusion nuclear science facility. *Fusion Engineering and Design*, 135:324–336, 2018.

[75] Yue Huang, MS Tillack, NM Ghoniem, JP Blanchard, LA El-Guebaly, and CE Kessel. Multiphysics modeling of the fw/blanket of the us fusion nuclear science facility (fnsf). *Fusion Engineering and Design*, 135:279–289, 2018-a.

[76] Yue Huang, Fabio Cismondi, Eberhard Diegele, Giafranco Federici, Alessandro Del Nevo, Fabio Moro, and Nasr Ghoniem. Thermo-structural design of the european demo water-cooled blanket with a multiscale-multiphysics framework. *Fusion Engineering and Design*, 135:31–41, 2018-b.

[77] Tim D Bohm, Andrew Davis, Moataz S Harb, Edward P Marriott, and Paul PH Wilson. Initial neutronics investigation of a liquid-metal plasma-facing fusion nuclear science facility. *Fusion Science and Technology*, 75(6):429–437, 2019.

[78] A Davis, M Harb, L El-Guebaly, P Wilson, E Marriott, et al. Neutronics aspects of the fess-fnsf. *Fusion Engineering and Design*, 135:271–278, 2018.

[79] F Tavassoli. APPENDIX A MATERIAL DESIGN LIMIT DATA A3.S18E EUROFER STEEL. Technical Report CEA/DEN/SAC/DMN, 7 2002.